



This deliverable has not yet been externally reviewed and approved by the European Commission.

Project no.:	101095738		
Project full title:	6G Short range extreme communication IN Entities		
Project Acronym:	6G-SHINE		
Project start date:	01/03/2023	Duration	30 months

D2.3 – RADIO PROPAGATION CHARACTERISTICS FOR IN-X SUBNETWORKS

Due date	30/11/2024	Delivery date	30/11/2024
Work package	WP2		
Responsible Author(s)	Enrico M. Vitucci (CNIT)		
Contributor(s)	Enrico M. Vitucci (CNIT), Usman Virk (Keysight), Fengchun Zhang (AAU), Ivan Bonev (AAU), Elena Bernardi (CNIT), Juha-Matti Runtti (Keysight), Vittorio Degli Esposti (CNIT), Pekka Kyösti (Keysight).		
Version	V1.0		
Reviewer(s)	Basuki Priyanto (Sony), Filipe Conceicao (IDE)		
Dissemination level	Public		

VERSION AND AMENDMENT HISTORY

Version	Date (MM/DD/YYYY)	Created/Amended by	Changes
V0.1	05/07/2024	Enrico M. Vitucci	Initial draft/ Table of Content
V0.2	04/11/2024	Enrico M. Vitucci	Draft for internal review
V0.3	06/11/2024	Berit H. Christensen	Updated list of figures, list of tables and cross-references.
V0.4	11/11/2024	Enrico M. Vitucci	Internal review No. 1
V0.5	20/11/2024	Enrico M. Vitucci	Internal review No. 2
V0.6	23/11/2024	Enrico M. Vitucci	Updates based on reviewers' comments
V0.7	28/11/2024	Enrico M. Vitucci	Last refinement
V0.8	29/11/2024	Berit H. Christensen	Update reference numbers
V0.9	30/11/2024	Berit H. Christensen	Proofreading and layout check
V1.0	30/11/2024	Enrico M. Vitucci	Final version (Submitted in the portal/SYGMA)

TABLE OF CONTENTS

- LIST OF FIGURES 6
- LIST OF TABLES 9
- ABBREVIATIONS 10
- EXECUTIVE SUMMARY 12
- 1. INTRODUCTION 13
- 2. RELEVANT PROPAGATION SCENARIOS FOR THE PROJECT 15
 - 2.1 FREQUENCY BANDS AND PROPAGATION PARAMETERS OF INTEREST..... 15
 - 2.2 SELECTED MEASUREMENT SCENARIOS AND MAPPING TO THE USE CASES 15
 - 2.3 LAISON WITH OTHER EU SNS JU PROJECTS 16
 - 2.4 DATA AVAILABILITY AND ITS ALIGNMENT WITH THE DATA MANAGEMENT PLAN 17
- 3. PROPAGATION MEASUREMENTS AND MODELLING IN INDUSTRIAL SCENARIOS..... 18
 - 3.1 MEASUREMENTS SETUP 18
 - 3.2 MEASUREMENTS IN INDUSTRIAL SCENARIOS 18
 - 3.2.1 Spatial map measurements20
 - 3.2.2 Short range measurements24
 - 3.2.3 Virtual antenna array (VAA) for a few spatial locations27
 - 3.2.4 Large-scale VAA29
 - 3.2.5 Summary.....31
 - 3.3 CHANNEL MODELING FOR SHORT-RANGE INDOOR FACTORY SCENARIOS ... 32
 - 3.3.1 Analysed measurement campaigns.....32
 - 3.3.2 Data-Postprocessing and Large-Scale Parameters (LSPS) Extraction 33
 - 3.3.3 Results: Aalborg University Industrial Production Lab.....34
 - 3.3.3.1 Delay spread analysis.....35
 - 3.3.3.2 K-Factor analysis 37
 - 3.3.3.3 Pathloss analysis 39
 - 3.3.4 GSCM model parametrization and spatially consistent example channel model from WP5 POC.....44
 - 3.3.5 Summary.....46
- 4 PROPAGATION MEASUREMENTS AND MODELLING FOR IN-VEHICLE AND OUTDOOR2VEHICLE SCENARIOS.....47
 - 4.1 IN-VEHICLE MEASUREMENTS AT AAU47
 - 4.1.1 Analysis of in-cabin LOS measurements in the car.....55

- 4.1.2 Summary.....56
- 4.2 IN-VEHICLE MEASUREMENTS AND OUTDOOR2VEHICLE MEASUREMENTS AT CNIT 57
 - 4.2.1 Measurement setup.....57
 - 4.2.2 In-vehicle scenarios.....59
 - 4.2.3 Outdoor2vehicle scenarios61
 - 4.2.4 Measurement post-processing and relevant propagation parameters.....62
 - 4.2.4.1 Power Delay Profile and Associated Propagation Parameters.....62
 - 4.2.4.2 Penetration Loss Analysis63
- 4.3 MODELING OF PROPAGATION IN IN-VEHICLE AND OUTDOOR2VEHICLE SCENARIOS AT FR3 AND D-BAND FREQUENCIES 64
 - 4.3.1 In-vehicle Results64
 - 4.3.1.1 Path loss and RMS delay spread results for in-vehicle scenario, at FR3 and sub-THz frequencies.....64
 - 4.3.1.2 Penetration loss results in-vehicle OLOS SCENARIO.....65
 - 4.3.1.3 Power angle delay profile in in-vehicle scenario66
 - 4.3.2.1 Transmission loss results in O2V scenario67
 - 4.3.2.2 Transmission loss results in o2v scenario at FR3 frequencies69
 - 4.3.2.3 Signal Spillover Effect through Window Transmission at FR3 frequencies69
 - 4.3.2.4 Transmission loss results in O2V scenario at D-band frequencies70
 - 4.3.2.5 Power angle delay profile in O2V scenario71
- 5 PROPAGATION MODELLING IN SHORT-RANGE OUTDOOR CAMPUS SCENARIOS..... 74
 - 5.1 MULTI-BAND MEASUREMENTS IN A CAMPUS SCENARIO 74
 - 5.2 DELAY SPREAD ANALYSIS.....76
 - 5.3 K-FACTOR ANALYSIS.....78
 - 5.4 PATHLOSS ANALYSIS80
 - 5.5 COMPARISON OF LSPs WITH 3GPP 5G INF CHANNEL MODELS AND DISCUSSION 83
 - 5.6 LARGE-SCALE PARAMETERS COMPARISON BETWEEN MEASUREMENTS AND RAY-TRACING87
 - 5.7 SUMMARY.....88
- 6 CHARACTERIZING HUMAN BODY SHADOWING AT D-BAND SUB-THZ FREQUENCIES..... 90
 - 6.1 MEASUREMENT SETUP90
 - 6.2 RESULTS AND DISCUSSION92

- 6.3 MULTIPATH CHANNEL MODEL INTEGRATING HUMAN BLOCKAGE EFFECT MEASUREMENT SETUP 94
- 6.4 SUMMARY..... 95
- 7 PROPAGATION MODELLING AND MEASUREMENTS FOR RIS-AIDED WIRELESS COMMUNICATIONS 97
 - 7.1 DEVELOPMENT OF MACROSCOPIC RIS CHANNEL MODELS 97
 - 7.1.1 Reflective and Transmissive RISs 97
 - 7.1.2 Power Balance on a RIS 98
 - 7.1.3 Antenna-Array-Like vs ray-based modelling approach..... 100
 - 7.1.3.1 AAL approach..... 100
 - 7.1.3.2 Fully ray-based approach..... 103
 - 7.1.4 Parametrization of RIS models 107
 - 7.1.5 Integration of RIS model into deterministic or geometrical-stochastic planning tools..... 107
 - 7.2 MEASUREMENTS WITH RIS 107
 - 7.2.1 3D reradiation characterization of RIS 108
 - 7.2.2 RIS Diagnosis..... 113
 - 7.2.3 Summary..... 115
- 8 CONCLUSIONS AND RECOMMENDATIONS 116
- REFERENCES..... 118

LIST OF FIGURES

Figure 1. Anritsu’s distributed VNA channel sounder	19
Figure 2. Biconical antenna: (a) photo and (b) gain of the antenna	19
Figure 3. (a) The smart production lab, (b) the Tx and (c) the Rx of the channel sounder	21
Figure 4. Measurement map for (a) Rx_0, (b) Rx_1 and (c) Rx_2, where the Rx and the Tx are denoted by BS and UE, respectively. Note that Rx locations are noted by blue stars and those of Tx by yellow triangulars.	22
Figure 5. CIRs of data BS_1-UE (01, 20) (as illustrated by green arrow in Figure 4 (b)) for three frequency bands	23
Figure 6. CIR profiles between the Rx1 and the Tx at 19 locations as highlighted with red dashed line in Figure 4 (b)	24
Figure 7. Scenario 1: 6-arm system, (a) photo and (b) distribution map of the Tx and the Rx.....	25
Figure 8. Scenario 2: production line system, (a) photo and (b) distribution map of the Tx and the Rx. 26	
Figure 9. CIRs of Tx 0 - Rx 1 with the Tx and Rx with the same height.....	26
Figure 10. CIRs of Tx 1 - Rx 1 with the Tx and Rx with different heights.....	27
Figure 11. CIRs of Tx 1 - Rx 1 with the Tx and Rx with the same height.....	27
Figure 12. VAA measurement: (a) photos and (b) distribution map of the Tx and the Rx.....	28
Figure 13. Measured CIRs (left) and PADPs by using classical beamforming (right) in three frequency bands for Tx 1: (a) 2.5-4.5 GHz, (b) 10-12 GHz and (c) 28-30 GHz	29
Figure 14. Large-scale VAA: (a) photos and (b) locations of the Tx and the Rx	30
Figure 15. Measured CIRs (left) and PADP by using classical beamforming (right) in three frequency bands: (a) 2.5-4.5 GHz, (b) 12-14 GHz and (c) 28-30 GHz	31
Figure 16. Data preparation flowchart.....	34
Figure 17. FR1 channel delay spreads in each Rx location (triangle). The three figures from left to right denote the three Tx locations (blue pentagram) in the measurement.	35
Figure 18. FR3 channel delay spreads	36
Figure 19. FR2 channel delay spreads	36
Figure 20. Delay spread CDF FR1 (left), FR3 (middle) and FR2 (right).....	37
Figure 21. Measured FR1 channel K-factors.....	38
Figure 22. Measured FR3 channel K-factors.....	38
Figure 23. Measured FR2 channel K-factors	39
Figure 24. Channel K-factor CDF extracted from FR1 (left), FR3 (middle) and FR2 (right) measurements and comparison with 3GPP	39
Figure 25. Measured FR1 channel pathloss	40
Figure 26. Measured FR3 channel Pathloss	40
Figure 27. Measured FR2 channel Pathloss	41
Figure 28. Pathloss CDF extracted from FR1 (left), FR3 (middle) and FR2 (right) from measurements and comparison with 3GPP	41
Figure 29. Pathloss floating intercept fit of FR1 channel and comparison with 3GPP InF-DL (left) and InF-SL (right) pathloss models	41
Figure 30. Pathloss floating intercept fit of FR3 channel and comparison with 3GPP InF-DL (left) and InF-SL (right) pathloss models	42
Figure 31. Pathloss floating intercept fit of FR2 channel and comparison with 3GPP InF-DL (left) and InF-SL (right) pathloss models	42
Figure 32. Shadow fading LOS (left) and NLOS (right) for FR1	42

Figure 33. Shadow fading LOS (left) and NLOS (right) for FR343

Figure 34. Shadow fading LOS (left) and NLOS (right) for FR2 43

Figure 35. Channel model implementation in F9860000A Keysight Channel Studio GCM.....44

Figure 36. Emulating generated channel model with Keysight low-latency F8820B PROPSIM channel emulator and validating model characteristics with Keysight N5247B PNA and N5247B UXA.44

Figure 37. PDP validation for RX position no. 6 (from Figure 80) of the derived channel model.45

Figure 38. Model and measured Temporal Autocorrelation Function (TCF) for the derived channel model over the UE route.45

Figure 39. Measured Doppler spectrum for the derived channel model over the UE route..... 45

Figure 40. Photos of the antenna used in the measurement campaigns48

Figure 41. Measurement locations in the engine bay of the (a) van and (b) the car..... 49

Figure 42. Diagram of the measurement system for measurements in the passenger cabin 49

Figure 43. Photos of the channel spatial measurements in (a) Scenario 1 and (b) Scenario 2..... 50

Figure 44. Measured CIRs for (a) Tx1-R1 in the van, (b) Tx1-Rx3 in the van, (c) Tx1-Rx5 in the van, (d) Tx1-Rx1 in the car, (e) Tx1-Rx3 in the car and (f) Tx1-Rx4 in the car..... 51

Figure 45. RMS delay spread results for measurements (a) in the van and (b) car, where the mean values are denoted by dashed lines.52

Figure 46. Measured PADPs in Scenario 1 at (a) low frequency band and (b) mmWave band 53

Figure 47. Trajectory of the main MPCs in relation to geometry of Scenario 1..... 53

Figure 48. Measured PADPs in Scenario 2 at (a) low frequency band and (b) mmWave band..... 54

Figure 49. Images depicting various in-vehicle Line-of-Sight scenarios, with the following link distances: Scenario A – 0.91 m, Scenario B – 1.62 m, and Scenario C – 0.88 m 55

Figure 50. Pictures of the measurements campaign at sub-THz (D-Band). 58

Figure 51. Pictures of the measurements campaign at FR3 (X-Band).....58

Figure 52: Seating position scenarios..... 59

Figure 53. Floor position scenarios. 60

Figure 54. Combined floor and seat scenarios. 60

Figure 55. Measurement setup to analyse power angle delay profile..... 60

Figure 56. Different measurements setups outdoor2vehicle (O2V)..... 61

Figure 57. Different configurations for setup 1 and setup 3, where the receiver height varies..... 61

Figure 58. Different setups O2V with Rx mounted on a mechanical rotator.....62

Figure 59. Pictures of the various OLoS scenarios: Scenario 1, Scenario 2, and Scenario 3. 64

Figure 60. Penetration loss values at D-Band frequencies for obstructing obstacles, including the seat backrest of the Tesla Model Y, the seat backrest of the Seat Leon, and the area beneath the seats of the Tesla Model Y. 65

Figure 61. In-vehicle scenario evaluated for PADP result. 67

Figure 62. PADP result for in-vehicle scenario. 67

Figure 63. Penetration loss values for O2V scenario at FR3 frequencies.....68

Figure 64. Penetration loss values for O2V scenario at D-Band frequencies..... 68

Figure 65. Geometry of the O2V scenario for evaluating penetration loss caused by the vehicle door. 70

Figure 66. PADP for the O2V scenario with the Tx positioned externally in front of the trunk..... 71

Figure 67. PADP for the O2V scenario with the Tx positioned externally in front of the hood..... 72

Figure 68. Main power paths detected in the PADP for the specific O2V scenario..... 73

Figure 69. PADP for the O2V scenario with the Tx positioned externally on the rear side of the vehicle. 73

Figure 70. Picture of the Rx Tx locations and the courtyard site in Aalborg University..... 75

Figure 71. Figurative picture of the measurement site with calculated Rx (green pentagram) and Tx (blue square) LOS distances.....	75
Figure 72. FR1 channel delay spread.....	76
Figure 73. FR3 channel delay spread.....	77
Figure 74. FR2 channel delay spreads	77
Figure 75. Delay spread CDF FR1 (left), FR3 (middle) and FR2 (right).....	78
Figure 76. FR1 channel K-factors.....	79
Figure 77. FR3 channel K-factors.....	79
Figure 78. FR2 channel K-factors.....	80
Figure 79. K-factor CDF FR1 (left), FR3 (middle) and FR2 (right).....	80
Figure 80. FR1 channel pathloss.....	81
Figure 81. FR3 channel Pathloss.....	82
Figure 82. FR2 channel Pathloss.....	82
Figure 83. Pathloss CDF FR1 (left), FR3 (middle) and FR2 (right)	83
Figure 84. Floating intercept fit of measured FR1(left), FR3 (middle) and FR2 (right) and 3GPP UMi model pathloss	83
Figure 85. 3D-model of measurement site with simulated ray paths generated for the CNIT raytracing simulation.....	87
Figure 86. Measured and CNIT simulated PDPs with delay spreads and K-factors calculated (positions 20, 45, 46 and 65) FR3.....	88
Figure 87. D-band human blockage measurement system.....	91
Figure 88. D-band human blockage layout and human trajectories.....	91
Figure 89. LOS PDP of the link without blockage	92
Figure 90. The reference fading pattern of the cylinder	93
Figure 91. Comparison of D-band human blockage attenuation between measurement and theoretical models for lateral human crossing.....	94
Figure 92. Comparison of D-band human blockage attenuation between measurement and theoretical models for frontal human crossing	94
Figure 93. The blockers movement along with the trace of the individual paths	95
Figure 94. Channel gains over time of the individual path	95
Figure 95. Bilateral power balance at a generic surface element.....	98
Figure 96. Generic antenna element, its cardioid-shaped radiation pattern and the Tx/Rx geometry.102	
Figure 97. Reradiated field [V/m] in the xz plane for a horizontal xy 7x7 m LIS centred in the origin: f = 3 GHz, normal incidence, phase gradient set for TE-polarization.....	103
Figure 98. Incident and reradiated rays on a point of a periodic RIS, with representation of the total surface phase gradient.	105
Figure 99. Incident and (anomalously) diffracted ray on a RIS edge	106
Figure 100. Comparison of the ray model with the PO model in terms of field strength along the dashed	106
Figure 101. The fundamental geometrical parameters of a RIS aided wireless communication system, where the assumption is that the Rx is positioned in the far-field of the RIS, and the Tx is situated in the near-field of the RIS.....	108
Figure 102. Photo (a) and diagram (b) of the proposed OTA testing system	109
Figure 103. Measured RIS reradiation in the beamforming direction (30°, 0°): (a) 3D pattern and (b) 2D cut pattern with azimuth angle of 0°	110

Figure 104. Measured RIS reradiation in the beamforming direction (45°, 225°): (a) 3D pattern and (b) 2D cut pattern with azimuth angle of 225° 111

Figure 105. Measured RIS reradiation pattern in two cuts with azimuth angle of: (a) 0° and (b) 45°. The directions of multiple intended beamforming in each cut are as they are shown in the legend 112

Figure 106. RIS diagnosis measurement setup: (a) photo and (b) diagram 113

Figure 107. The proposed RIS diagnosis method applied to five scenarios 114

LIST OF TABLES

Table 1: Measurement scenarios and relation with use cases 15

Table 2: Antennas specifications 20

Table 3: VNA setting 20

Table 4: Antennas specifications 24

Table 5: Tx and Rx set-up 24

Table 6: VNA setting 25

Table 7: Antennas specifications 28

Table 8: VNA setting 28

Table 9: Antennas specifications 30

Table 10 VNA setting 30

Table 11: Summary of measurement campaigns for the indoor factory scenario 32

Table 12: Specification of the engine bay measurements 47

Table 13: Specification of the channel spatial measurements 50

Table 14: Overview of RMS Delay Spread, Path Loss, and IF SPL Values for Various In-Vehicle LoS Scenarios (illustrated in Fig. 49) Across Different Frequency Ranges. 56

Table 15: Parameters and characteristics of the measurement setup at sub-THz (D-Band) 58

Table 16: Parameters and characteristics of the measurement setup at FR3 (X-Band). 59

Table 17: Link distances different scenarios and frequencies. 60

Table 18: RMS Delay Spread, Path loss and Isotropic Free-Space Path Loss for the In-vehicle OLoS scenarios shown in Fig. 59 64

Table 19: Mean penetration Loss and standard deviation values in in-vehicle scenario at sub-THz. 66

Table 20: Mean penetration Loss and standard deviation values in O2V scenario at FR3 frequencies. . 69

Table 21: Mean penetration Loss and standard deviation values in O2V scenario at D-Band frequencies. 71

Table 22: Summary of measurement campaigns for the outdoor campus scenarios 74

Table 23: Statistics of estimated FR1 (2.5-4.5 GHz) large-scale parameters and comparison to corresponding 3GPP model parameters. 84

Table 24: Statistics of estimated FR3 (10-12 GHz) large-scale parameters and comparison to corresponding 3GPP model parameters. 85

Table 25: Statistics of estimated FR2 (28-30 GHz) large-scale parameters and comparison to corresponding 3GPP model parameters. 86

Table 26: Selected parameters for CNIT raytracing simulation 87

Table 27: Measurement setup parameters 91

Table 28. Human measurement subjects' physical dimensions and total number of measurement sweeps 91

ABBREVIATIONS

Acronym	Description
AAL	Antenna- Array-Like
AAL Approach	Antenna- Array-Like Approach
AOA	Angle of arrival
AP	Access point
BS	Base station
C-band	Conventional Band
CDF	Cumulative distribution functions
CENTRIC	Towards an AI-Native User-Centric Air Interface for 6G Networks
CIR	Channel impulse responses
CW	Continuous wave
CFR	Channel frequency response
dB	Decibel
dBi	Decibel isotropic
D-band	D-frequency band (110-170 GHz)
ELAA	Extra-large antenna array
EM	Electromagnetic
ETSI	European Telecommunications Standards Institute
IEEE	Institute of Electrical and Electronics Engineers
ISG	Industry specification group
InF-DL	Indoor Factory with Dense clutter and Low base station height
InF-SL	Indoor Factory with Sparse clutter and Low base station height
FR1 – FR2 – FR3	Frequency band 1, 2 and 3
GO	Geometrical Optics
GHz	Gigahertz
GSCM	Geometry-Based Stochastic Channel Model
IFSPL	Isotropic free space path loss
InF	Indoor Factory
KED	Knife-edge diffraction
IOT	Internet-of-things
K-factor	Rician factor
LSP	large-scale channel parameter
LOS	Line-of-sight
L	Penetration loss
MEMS	Micro-electromechanical systems
METIS	Mobile Enablers for Twenty-Twenty Information Society
MSE	Mean square error
MHz	Megahertz
MPCs	Multipath components
NLoS	No line-of-sight
OloS	Obstructed line-of-sight
O2V	Outdoor-to-vehicle

OTA	Over-the-air
PADP	Power-angle-delay profile
PL	Path loss
PGM	Phase Gradient Metasurface
PO	Physical Optics
PoC	Proof of Concept
PDP	Power-delay profile
RIS	Reconfigurable Intelligent Surfaces
RMSE	Root Mean Square Error
RMS	Root mean square
RoF	Radio over Fiber
Rx	Receiver
SMD	Spatial Modulation Dyadic
SW	Software
sub-THz	Sub-terahertz
TERRAMETA	TER ahertz Reconfigurable META surfaces for ultra-high-rate wireless communications
TIMES	THz industrial mesh networks in smart sensing & propagation environments
Tx	Transmitter
UC1	Use case 1
UTD	Uniform geometrical theory of diffraction
UCA	Uniform circular array
VNA	Vector network analyser
VAA	Virtual antenna array
X-band	Frequency range between 8.0 GHz and 12.0 GHz.
3GPP	The 3rd Generation Partnership Project

EXECUTIVE SUMMARY

This report is the third deliverable of the 6G-SHINE Work Package 2 (WP2) and it consolidates the knowledge of radio propagation through measurement campaigns and the derivation of channel models in the identified scenarios, for all the frequency bands of interest. Wireless propagation in confined and cluttered environments such as industrial and in-vehicle scenarios, that are of great interest for the design of future subnetworks, was not completely explored, and there are only few studies in the literature covering multiple frequency bands including sub-6GHz, mm-wave and sub-THz. Therefore, the present document contributes at reducing this knowledge gap, by analysing the results of multiple measurement campaigns and providing indications on how to improve existing channel models, or how to parametrize them. Finally, a macroscopic modelling approach is proposed to efficiently compute the reradiated field by reconfigurable intelligent surfaces and to evaluate the performance of RIS-aided wireless networks.

The deliverable is organized as follows: Section I provides an introduction, while Section II recaps the relevant propagation scenarios for the project, and in particular the relationship between the project use cases and the selected measurement scenarios. Sections from III to VI describe the measurement campaigns for the different scenarios and presents some preliminary results: in particular, measurement results are analysed in detail for some of the presented scenarios by extracting some reference channel parameters from the measurements, which are then compared with reference channel models such as 3GPP models, and deterministic ray tracing simulation. In the analysis, particular attention is given to the new frequency bands for 6G, such as sub-THz and the mid-band frequency range (7-24 GHz, also known as FR3). Section VII provides the macroscopic models for RIS, and an automated measurement system is introduced to evaluate the performance of a RIS under realistic conditions. Finally, conclusions are drawn in Section VIII.

1. INTRODUCTION

In recent years, the demand for reliable and high-speed wireless communication has surged, driven by the proliferation of connected devices and the advent of the Internet of Things (IoT) [19]. This has necessitated advancements in radio channel measurements and modelling, particularly for short-range communication within In-X subnetworks. These subnetworks, which involve industrial environments, indoor consumer scenarios, in-vehicle and outdoor-to-vehicle scenarios, present unique challenges and opportunities for wireless communication technologies [20][21] [22].

This deliverable document aims to present the unique contributions and advancements made by our project within the current landscape of channel measurements and modelling research for short-range communication. It encompasses detailed measurements and modelling efforts across various relevant propagation scenarios, offering insights into the propagation characteristics and channel models that are critical for the design and optimization of short-range communication systems.

The primary objectives of this document are to:

1. Analyse relevant propagation scenarios for short-range communication within In-X subnetworks
2. Review the state of the art in radio channel measurements and modelling, highlighting key advancements and their implications.
3. Conduct detailed measurement campaigns in selected scenarios, including measurements in industrial environments, short measurements in different types of environments, representative of the consumer scenarios, and measurements to assess the feasibility of in-vehicle subnetworks and outdoor-to-vehicle communication.
4. Develop and validate channel models based on the measurement data, providing a foundation for future research and development.
5. Characterize the impact of human body shadowing at D-band sub-THz frequencies, which is crucial for the deployment of high-frequency communication systems.
6. Explore the potential of Reconfigurable Intelligent Surfaces (RIS) in enhancing communication performance through innovative measurement and modelling techniques.

The document is structured as follows:

- Chapter 2: Relevant Propagation Scenarios for the Project - This chapter outlines the key propagation scenarios, reviews the state of the art, and discusses the frequency bands and propagation parameters of interest.
- Chapter 3: Propagation measurements and modelling in industrial scenarios - This chapter presents multi-band measurement campaigns conducted in various in-factories scenarios. Measurements are analysed in detail to derive channel parameters such as path-loss, delay spread, fading statistics (Rician K-factor) and compared with reference 3GPP models.
- Chapter 4: Propagation measurements and modelling for in-vehicle and outdoor-to-vehicle scenarios: this section provides an extensive analysis of radio propagation inside vehicles, considering several types of cars, several tx/rx and antenna configurations including outdoor2indoor cases, and multiband measurement campaigns. Results include path loss, delay spread analysis, penetration losses through car bodies and internal furniture, and angular characteristics of the radio channel. These results can be used to derive simplified formulas or to derive guidelines for the deployment of communication and sensor nodes in vehicular subnetworks.
- Chapter 5: Propagation modelling in short-range outdoor scenarios: this section provides the analysis of a short- range multi-band measurement campaign in a Campus scenario. The results are compared with 3GPP models and preliminary comparisons with a state-of-the-art 3D ray tracing tool are shown. Particular attention is given to the parametrization of the ray tracing model for the mid-

band frequencies (FR3). The obtained results and the adopted methodology are also applicable to subnetworks where the propagation environments have similar characteristics to the considered short-range scenario, such as the “consumer” use category described in D2.1 and D2.2.

- Chapter 6: Characterizing human body shadowing at D-band sub-THz frequencies: this chapter provides a modelling approach for the problem of human body shadowing, which is of great importance in indoor consumer scenarios, where the use of sub-THz frequencies is foreseen for future short-range broadband communication systems.
- Chapter 7: Propagation modelling and measurements for RIS-aided wireless communications: this chapter presents a macroscopic modelling approach for RIS. Novel Huygens-based and fully-ray based models that allow to compute the field reradiated by a RIS in a realistic and physically sound way are described: such models can be suitably integrated into ray-tracing models and used for the deployment of radio links in presence of RISs. This methodology can be applied for the design of subnetworks in all the scenarios analysed in previous chapters, and in particular in consumer and industrial environments. Finally, the chapter presents an automated 3D measurement system for the performance evaluation of real RIS prototypes and a method to study the degradation of RIS performance in the presence of malfunctions of some of its elements.
- Chapter 8: Conclusions - The final section summarizes the key findings and discusses the implications for future research and development.

By systematically addressing these objectives and providing a detailed analysis of the measurement and modelling efforts, this document aims to contribute to the advancement of short-range communication technologies within In-X subnetworks. The insights gained from this research will be instrumental in the design and optimization of next-generation wireless communication systems, ensuring their reliability and performance in diverse and challenging environments.

2. RELEVANT PROPAGATION SCENARIOS FOR THE PROJECT

In the following, the main scenarios of interest for the 6G-SHINE project that have been analysed during the activities carried out in WP2-Task2.2 (“Measurement and modelling of propagation in the scenarios of interest”) are briefly reviewed. The considered frequency bands, the relation with use cases and other EU SNS JU projects are also summarized, as well as the main outcomes of WP2-Task2.2 in terms of data that will be used by WP3-WP4-WP5 and will be made publicly available as open data.

2.1 FREQUENCY BANDS AND PROPAGATION PARAMETERS OF INTEREST

Each new generation of mobile communications addresses new spectrum bands. In 5G, the centimetre wave band (i.e., FR1, ranging from 410 MHz to 7.125 GHz) was complemented with the millimetre wave band (24.250-70 GHz, FR2) to significantly increase throughput and reduce latency. For 6G, in addition to FR1 and FR2 two different blocks of spectrum are currently being investigated: the mid-bands (7-24 GHz, also known as FR3, despite at the moment there is no official source for this) and the sub-THz bands (100-350 GHz), which are currently undergoing pre-standardization activities (one of them is described in the “ETSI ISG THz Activity Report 2023” [57]), with several envisioned applications, such as in-vehicle entertainment, remote surgery, backhaul, etc. All the above-mentioned frequency bands are expected to be part of the next generation wireless systems and are good candidates for different types of subnetworks, fully falling within the scope of the 6G-SHINE project which aims to realize a broad network of subnetworks.

In particular, the present document aims at filling some of the gaps in knowledge of radio channel characteristics in short-range, cluttered and confined environments (e.g. in-vehicle and industrial scenarios), especially for the new frequency bands (mid-band-FR3 and sub-THz). Among the analysed propagation parameters there are path-loss, delay spread, penetration loss through objects/materials, power-angle profiles, fading statistics (e.g. Rician K-factor).

2.2 SELECTED MEASUREMENT SCENARIOS AND MAPPING TO THE USE CASES

The measurement scenarios considered in this document for the aim of channel characterization and modelling are consistent with the use-cases and use-categories presented in D2.1 and D2.2 [58], [59]. A mapping between the measurement campaigns performed and the corresponding use cases is reported in the following *Table 1*.

Table 1: Measurement scenarios and relation with use cases

Measurement Scenario	Operating Frequencies	Analysed propagation parameters	Related Uses Case Categories
Spatial map measurements in production lab	2.5-4.5 GHz, 10-12 GHz, 28-30 GHz	Path Loss, Power-Delay Profiles, Delay Spread, K-factor	Industrial UC4 (subnetworks swarms)
Short-range industrial measurements - 6-arms operation platform and industrial assembly line platform	2.5-4.5 GHz, 10-12 GHz, 28-30 GHz	Path Loss, Power-Delay Profiles, Delay Spread	Industrial UC1 (robot control), UC2 (unit test cell), UC3 (Visual inspection cell)

Virtual array measurements in industrial environment	2-30 GHz	Power-Angle-Delay Profiles	Industrial UC4 (subnetworks swarms)
In-vehicle	1-8 GHz, mm-wave (28 GHz) subTHz (100 GHz, D-band), FR3 (8-15 GHz)	Attenuation, PdP/Delay Spread, Spatial measurements (fading characteristics)	Vehicular UC1 (Wireless Zone ECU) , UC2 (Collaborative Wireless Zone ECUs), UC3 (intra-subnetwork communication)
Outdoor2indoor with vehicle	subTHz (D-band), FR3 (8-15 GHz), mm-wave (26-38 GHz)	Attenuation, PdP/Delay Spread, PaP/Angle Spread (FR3 and mm-wave only), Fading statistics (FR3 and mm-wave only)	Vehicular UC3 (inter-subnetwork communication)
Human Body shadowing	D-band	Path loss, Power-Angle Profiles	Consumer (all)
Short-range measurements in a Campus scenario	FR1, FR2, FR3	Path loss, Power-Delay Profiles, K-factor Delay Spread	Consumer (all)
RIS angular characterization, RIS diagnosis	3.5 GHz	Path Loss, Power Angle Profiles	Consumer (all UCs), Vehicular UC2

2.3 LAISON WITH OTHER EU SNS JU PROJECTS

The 6G-SHINE project collaborates actively with several key SNS projects, including TIMES [60], TERRAMETA [61], and CENTRIC [62], to foster a more unified approach to advancing 6G technologies.

- TIMES has been funded under the SNS Work Programme Phase 1 Stream B, which focuses on novel technologies for commercial networks in a mid and/or long-term time period. From the channel modelling perspective, 6G-SHINE and TIMES work together on developing channel models for sub-THz frequencies in industrial and confined/cluttered propagation environments. Channel models and planning criteria for RIS-aided communications are also of common interest for the two projects.
- TERRAMETA project aims to investigate revolutionary technologies for 6G and demonstrate the feasibility of Terahertz (THz) Reconfigurable Intelligent Surface (RIS) assisted ultra-high data rate wireless communications networks. 6G-SHINE collaborates with TERRAMETA to study the performance of RIS and metasurfaces in realistic situations, including non-idealities of the RIS caused by imperfect design, and the effects of the surrounding propagation environment.
- CENTRIC proposes leveraging AI techniques through a top-down, modular approach to wireless connectivity that puts the users' communication needs and environmental constraints at the centre of the network stack design. Through collaboration with CENTRIC, 6G-SHINE aligns its

research with the practical implementation of deterministic ray-based channel models (ray launching and ray-tracing), and the integration of RIS macroscopic models into them.

These ongoing collaborations strengthen the 6G-SHINE project's outcomes by integrating insights across various specialized areas, ensuring that 6G infrastructure will be robust, responsive, and ready for future societal needs.

2.4 DATA AVAILABILITY AND ITS ALIGNMENT WITH THE DATA MANAGEMENT PLAN

In accordance with the Data Management Plan of the 6G-SHINE project, the following data derived from the present deliverable document will be made available open access in the official Zenodo repository of the project (<https://zenodo.org/communities/6g-shine/>):

- Post-processed data, in the form of tables and figures, summarizing the main propagation parameters at different frequency bands in the scenarios of interest (e.g. path-loss, delay spread, K-factor, penetration losses, etc.)
- Synthetic propagation parameters derived from ray tracing simulation, where the ray tracing tool has been properly parametrized according to the outcome of the measurement campaigns
- Basic implementation (e.g. Matlab code) for the developed macroscopic models for RIS, presented in Section 4.4 of this document.

3. PROPAGATION MEASUREMENTS AND MODELLING IN INDUSTRIAL SCENARIOS

All the measurement campaigns described in the document share a common architecture, where data have been acquired through a wideband channel-sounding system, based on Vector Network Analyzer (VNA).

In this chapter, we start with the description of the measurement campaigns in industrial environment and their outcomes in terms of insights into the characteristics of radio channels, in order to provide indications for radio channel modelling in the use-cases of interest for the project (see Table 1, Entries 1-3). The presented measurement campaigns cover multiple frequency bands and provide channel data in industrial environment either on a large scale employing omnidirectional antennas (“spatial map measurements”), or in a smaller scale and in a few selected locations (short-range measurements), also providing angular channel characteristics (power-angle-delay profiles) using directional antenna and with the aid of the Virtual Antenna Array measurement technique.

3.1 MEASUREMENTS SETUP

A channel sounding system is typically comprised of the following components:

- A transmitter (Tx) antenna, used to transmit radio signals.
- A receiver (Rx) antenna, used to receive radio signals.
- A vector network analyser (VNA), used to measure the channel frequency response (CFR) between the Tx and Rx antenna ports. The VNA is configured with operating frequency band, frequency points, a transmitted power level, and an intermediate frequency (IF) bandwidth.
- A laptop connected to the VNA, employed to control the operation of the VNA and store the measurement data.

The multipath components (MPCs) in delay and spatial domains for different frequency bands have been identified via a sounding system using a VNA coupled to a Virtual Antenna Array (VAA) and to a rotational directional antenna in [56]. More specifically in the latter, a uniform circular array (UCA) with a particular radius r and number of elements P is used. Furthermore, an explanation that the distance between two consecutive elements in the UCA should not be larger than $\lambda/2$ is given. It is worth noting that the reader can refer to equation (1) – (6) in [56]. More details about the radius and number of elements of the UCA for the VAA and large-scale VAA measurements can be found in Table 7 and Table 9.

3.2 MEASUREMENTS IN INDUSTRIAL SCENARIOS

The measurements in this sub-chapter were carried out in the “The Smart Production Laboratory” located at the Department of Mechanical and Manufacturing Engineering at Aalborg University. The laboratory size is (41 x 14 x 6) m. It is a typical industrial environment filled with various machines, assembly lines, movable robots, and robotic arm platforms, as illustrated in *Figure 3a* and defined as InF-DL in [25]. The Anritsu’s distributed modular two-port VNA (model ShockLine TM ME7868A series shown in *Figure 1*) was used to measure the CFR between the Tx and Rx antenna ports [23].

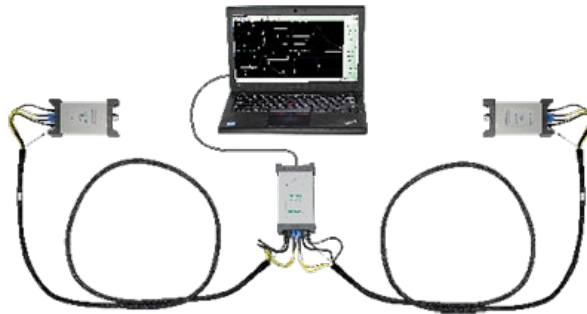


Figure 1. Anritsu's distributed VNA channel sounder

This VNA supports measurements in a frequency range of up to 43 GHz and at measurement distance of up to 100 m. Furthermore, it offers coherent phase measurements through the integrated phase-compensated Radio over Fiber (RoF) solution. In all measurements presented in this sub-chapter, two vertically polarized omnidirectional biconical antennas (shown in Figure 2), covering the frequency range of 2 to 30 GHz, were used.

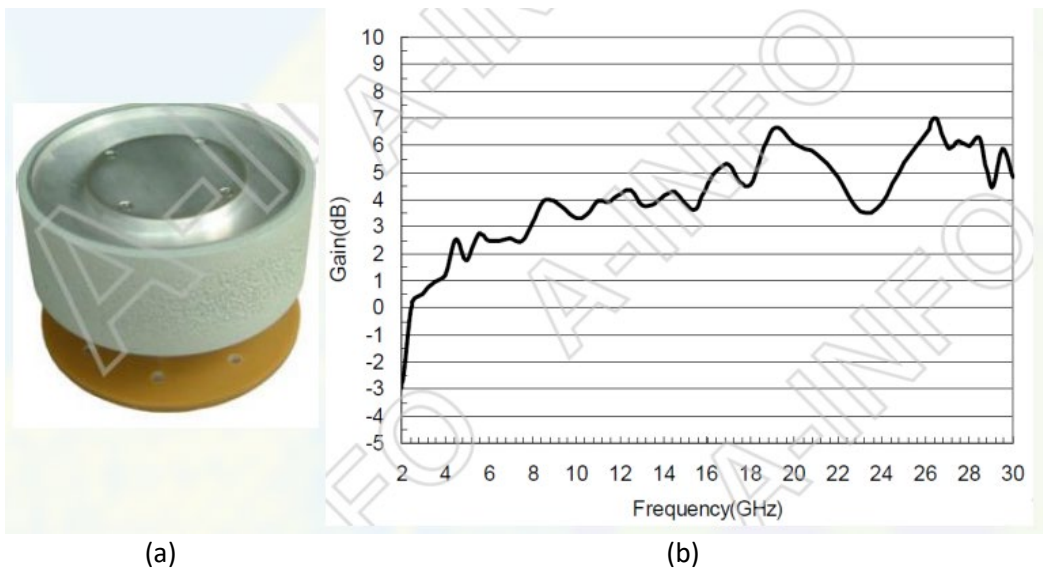


Figure 2. Biconical antenna: (a) photo and (b) gain of the antenna

The collection of extensive spatial radio map data at both macro and micro levels across diverse real-world deployment scenarios is crucial for training and testing the accuracy, complexity, and efficiency of machine learning-based radio map prediction methods. These radio maps also serve as a valuable resource for validating deterministic ray-tracing simulation models, which depend heavily on a detailed geometric and electromagnetic characterization of the propagation environment to ensure their accuracy.

Four different groups of measurement were conducted:

- Spatial map measurements
- Short-range measurements
- VAA

- Large scale VAA

Where the first group measurement belongs to macro-level spatial radio map measurement while the remaining groups are within the scope of micro-level spatial radio map measurements.

3.2.1 Spatial map measurements

Antennas and VNA setting's specifications are summarized in Table 1 and Table 2. Note that an antenna with a fixed position is used on both Tx and Rx sides.

Table 2: Antennas specifications

	Antenna	Height [m]	Number of Tx and Rx locations
UE(Tx)	P bi-conical antenna / INFO SZ-2003000. Polarization: vertical. Gain:	1.15	BS_0: 115 points BS_1: 89 points BS_2: 50 points
BS(Rx)	<ul style="list-style-type: none"> • 3.5 GHz: 1 dB • 11.0 GHz: 3.2 dB • 29.0 GHz: 4.5 dB 	1.15	3

It is noted that the Tx locations are labelled as BS while the Rx locations are labelled as UE in the maps in Fig. 4. The BS (Rx) were positioned in 3 locations as indicated by the blue stars. For each BS (Rx) location, the UE (Tx) were moved to many locations. For each pair of the BS and UE location, the channel frequency responses over the three bands were measured. As indicated in the maps in Fig. 4, for BS_0, we have 115 UE locations, for BS_1, we have 89 UE locations, and for BS_2, we have 50 UE locations.

Table 3: VNA setting

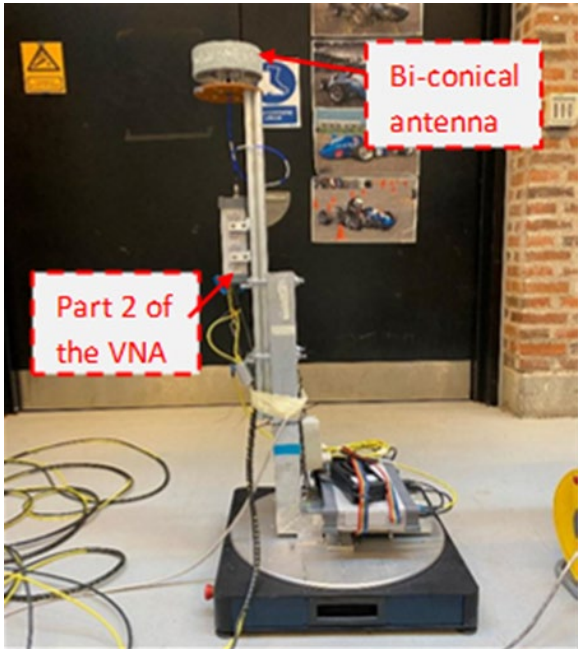
VNA setting	Power [dBm]	Frequency [GHz]	Number of frequency points
0		Band 1: 2.5 - 4.5 Band 2: 10 – 12 Band 3: 28 - 30	2001 for each band

Three frequency bands are measured, each of which is 2 GHz. The number of frequency points is chosen such that an adequate resolution in the frequency domain is obtained. Therefore, 2001 points gives an appropriate resolution of 1 MHz.

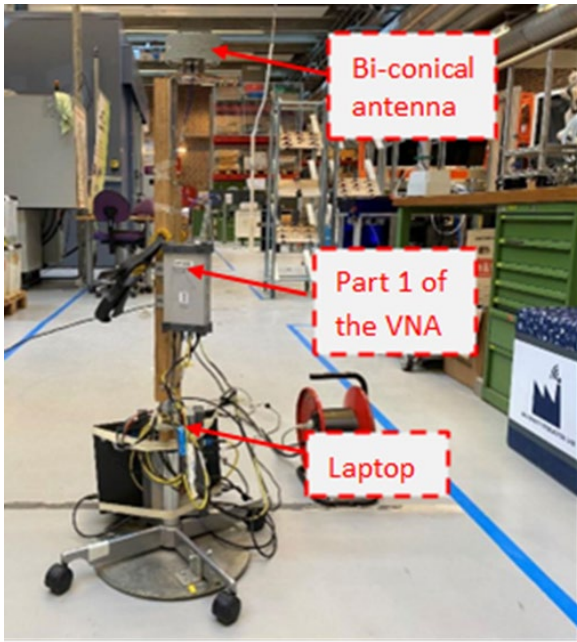
Photos of the laboratory environment and the measurement setup are shown in *Figure 3* and *Figure 4*, respectively.



(a)



(b)



(c)

Figure 3. (a) The smart production lab, (b) the Tx and (c) the Rx of the channel sounder



Figure 4. Measurement map for (a) Rx_0, (b) Rx_1 and (c) Rx_2, where the Rx and the Tx are denoted by BS and UE, respectively. Note that Rx locations are noted by blue stars and those of Tx by yellow triangulars.

The defined coordinate system is shown in Figure 4 (a). We can differentiate three scenarios:

- In scenario 1, BS_0 denotes the position of the Rx and it has coordinates (-0.52m, 17.07m).
- In scenario 2, BS_1 denotes the position of the Rx and it has coordinates (0.0m, 0.0m).
- In scenario 3, BS_2 denotes the position of the Rx and it has coordinates (2m, 36.75m).

The intervals between the adjacent Tx positions are 1 m, except 4 cases for scenario 1, where 3 possible Tx positions are skipped (those are shown with grey markers) and one Tx position does not fit to the initially predefined grid of 1 m.

Preliminary results of the channel impulse responses (CIR) for one specific location of the Tx for three frequency bands are shown in Figure 5.

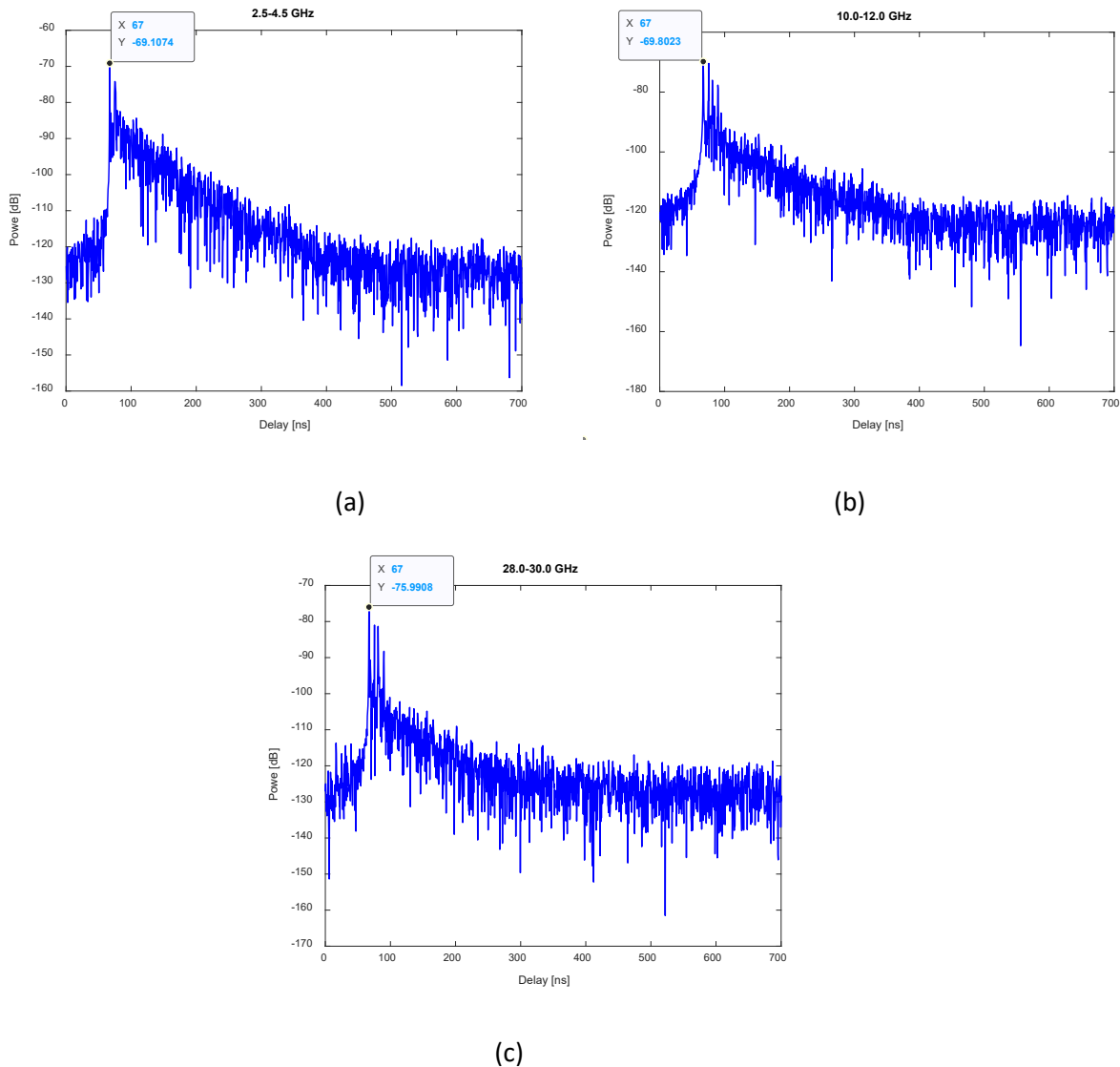


Figure 5. CIRs of data BS_1-UE (01, 20) (as illustrated by green arrow in Figure 4 (b)) for three frequency bands

CIRs results for that position of the Tx are presented, because both LOS and NLOS paths are available. The LOS path has a delay of 67 ns, which corresponds to distance of 20.1 m agreeing good enough with the measured distance of 20.02 m between the Tx and Rx. Some of the initial results have been processed further, presented and discussed in [1]. *Figure 4* from [1] is represented here as *Figure 6*.

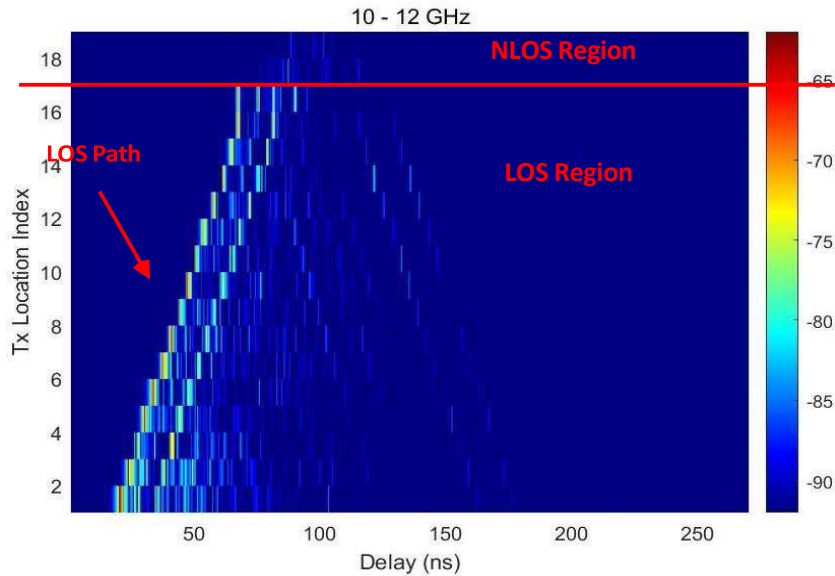


Figure 6. CIR profiles between the Rx1 and the Tx at 19 locations as highlighted with red dashed line in Figure 4 (b)

Figure 6 presents the measured CIRs between Rx1 and Tx located at 19 positions (highlighted in Figure 4 (b)) at 10 - 12 GHz, cover both the LOS and non-LOS regions. The CIR shows that the time for the LOS path between the Rx1 and Tx1 is 20 ns, which corresponds to distance of 6 m, in agreement with the measured distance of 6 m when planning the measurements. From the CIRs, the received power of the LOS path from the Tx1 to the Rx1 is -62 dB and is in good agreement with the theoretically evaluated free-space path loss of 68.8 dB, considering that the antenna gain of both the Tx and Rx antennas is 3.2 dB at 11 GHz. As the Tx is positioned further away from the Rx, the delay increases, and the power of the path decreases for the first arrival path. LOS scenarios are (Tx1 - Tx16) and non-LOS scenarios are the rest - (Tx17 - Tx19). The latter can be observed from the significant decrease in the peak power in scenarios (Tx17 - Tx19), compared to those obtained for the Tx positioned at the previous sixteen positions.

3.2.2 Short range measurements

Antennas, measurement set-up and VNA setting specifications are presented in Table 4, Table 5 and Table 6 respectively. In this set of measurements, the antennas are kept at fixed position.

Table 4: Antennas specifications

	Antenna
Tx	P bi-conical antenna / INFO SZ-2003000. Polarization: vertical.
Rx	Gain: <ul style="list-style-type: none"> • 3.5 GHz: 1 dB • 11.0 GHz: 3.2 dB • 29.0 GHz: 4.5 dB

Table 5: Tx and Rx set-up

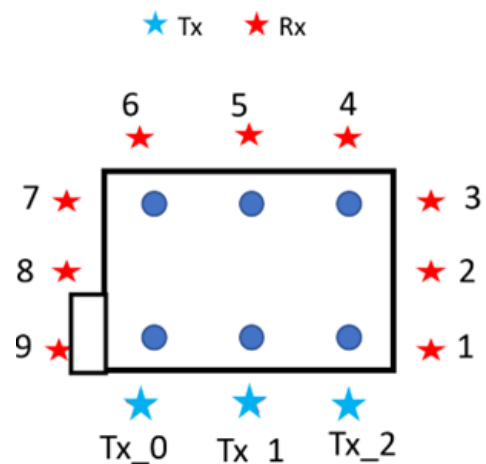
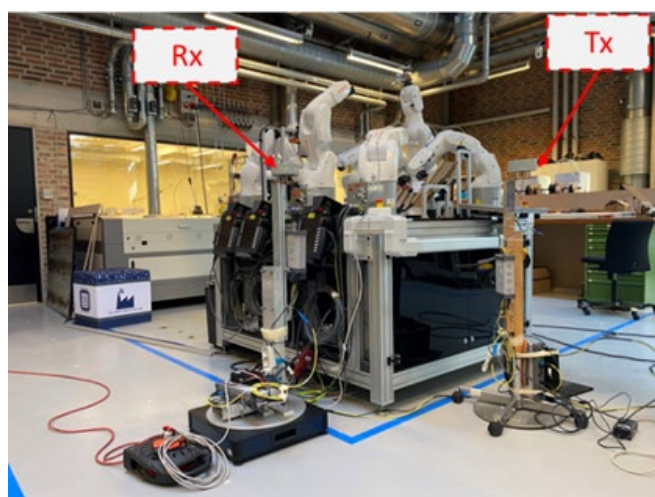
Scenario	Rx height [m]	Tx height [m]	Number of Rx locations	Number of Tx locations
1: 6-arm system	1.15	1.15	3	For Tx_0, Rx is located 1-8; For Tx_1, Rx is located 1-9; For Tx_2, Rx is located 2-9
	1.15	2.00	3	For all Tx locations (Tx_0, Tx_1 and Tx_2), Rx is located 1-9
2: production line system	1.15	1.15	For all Rx locations (Rx_0, Rx_1 and Rx_2), Tx is located 1 - 7	3

Table 6: VNA setting

VNA setting	Power [dBm]	Frequency [GHz]	Number of frequency points
0		Band 1: 2.5 - 4.5 Band 2: 10 – 12 Band 3: 28 - 30	2001 for each band

The VNA setting is the same as in the previous measurements. The photo and map of the measurement in 6-arm system scenario are shown in Figure 7 (a) and (b). For the Tx height set to 1.15 m case: the Tx was located at Tx_0 while the Rx was moved from location 1 to 8; the Tx was located at Tx_1 while the Rx was moved from location 1 to 9; the Tx was located at Tx_2 while the Rx was moved from location 2 to 9.

For the Tx height set to 2 m case: the Tx was located at Tx_0, Tx_1 and Tx_2 respectively; for each Tx location, the Rx was moved from location 1 to 9.



(a)

(b)

Figure 7. Scenario 1: 6-arm system, (a) photo and (b) distribution map of the Tx and the Rx

The photo and the map of the measurement in production line system scenario are shown in Figure 8 (a) and (b). The Rx was in 3 locations in blue colour; for each Rx location, the Tx was moved from location 1 to 7 locations indicated by the red stars.

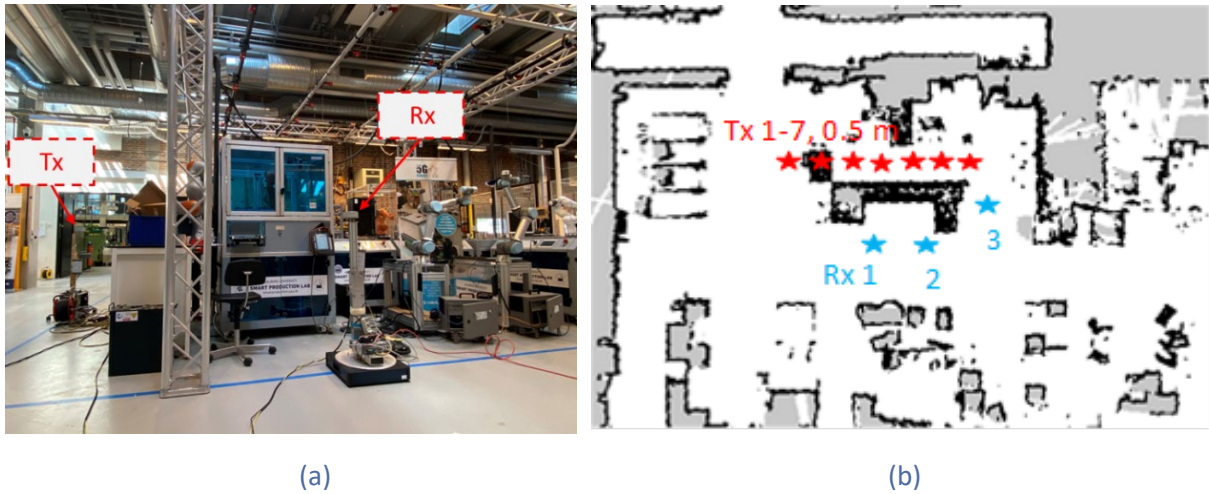


Figure 8. Scenario 2: production line system, (a) photo and (b) distribution map of the Tx and the Rx

Preliminary results of the CIRs between the Tx at location Tx_0 and the Rx at location 1 for Scenario 1 (6-arm system scenario) are shown in Figure 9 for the Tx height of 1.15 m and Figure 10 for the Tx height of 2 m respectively. Both CIR examples in Figure 9 and Figure 10 were recorded in LOS scenarios and a dominant direct path can be observed in each sub-figure. Obviously, the height of Tx has a negligible effect on measured power levels of the received signal for the three frequency bands, because the CIRs from Figure 9 are similar to those of Figure 10 for the respective frequency bands. As one could expect, the received power for the LOS path at lower frequency (-50 dB at 3.5 GHz) is higher than those at higher frequency (-65 dB at 30 GHz). The latter can be theoretically explained by the Friis law (please refer to [55]) and the fact the received power is inverse proportional to the frequency of the transmitted signal.

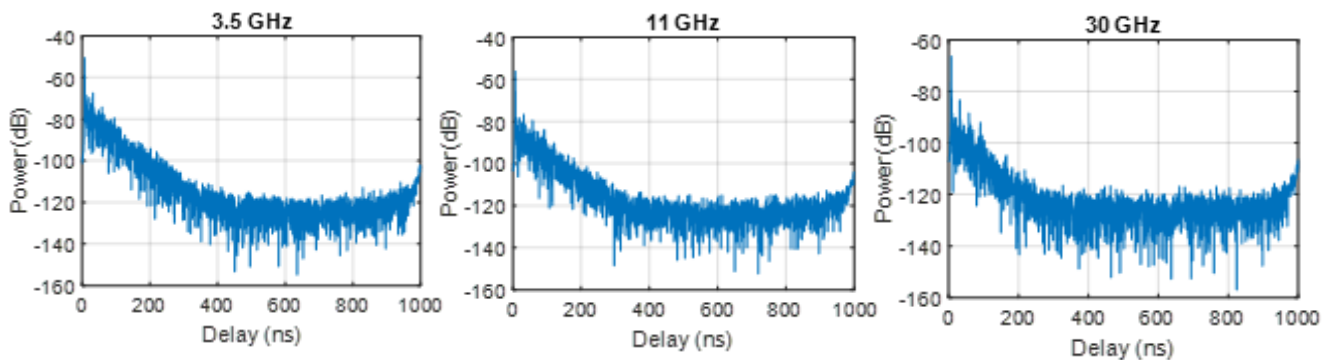


Figure 9. CIRs of Tx 0 - Rx 1 with the Tx and Rx with the same height

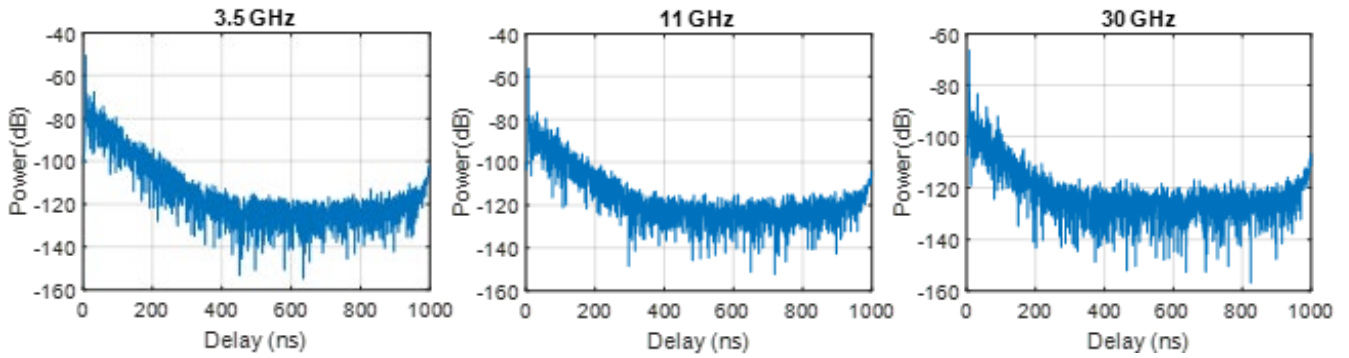


Figure 10. CIRs of Tx 1 - Rx 1 with the Tx and Rx with different heights

Preliminary results of the CIRs between the Tx 1 and the Rx 1 for Scenario 2 (production line system scenario) are shown in Figure 11. The CIR examples in Figure 11 were measured in a NLOS scenario, where the direct propagation path was blocked by the obstacles in the environment as illustrated by Figure 8.

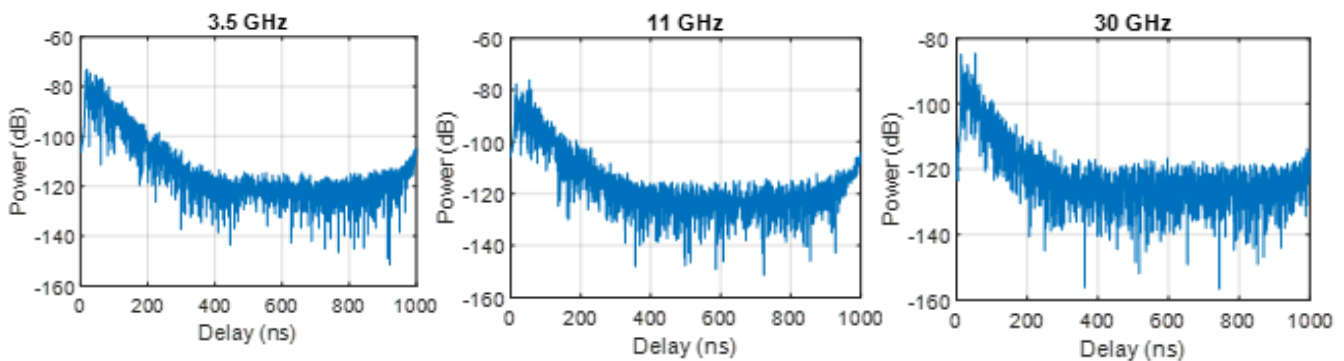


Figure 11. CIRs of Tx 1 - Rx 1 with the Tx and Rx with the same height

3.2.3 Virtual antenna array (VAA) for a few spatial locations

Antennas and VNA setting specifications are presented in *Table 7* and *Table 8* respectively. Note that number of the UCA elements 1 means that the antenna is at fixed position during the measurement. Radius of 20 cm and 180 elements of the UCA means that the Rx will move along a circle with radius 20 cm with a rotation step of 2°. For each position of the Rx, a measurement of the CFR between the Tx and the Rx is conducted. Therefore, information about the power levels and delays of the different propagation components of the transmitted signal between the Tx and Rx can be obtained based on an appropriate array processing (beamforming) algorithm. The obtained metric is called power angular delay profile (PADP) (please refer to *Figure 13* and *Figure 15*). The entire bandwidth from 2 to 30 GHz is measured at once. The reason for this is the need to obtain results for the entire bandwidth rather than for narrow band as in the previous two cases. Therefore, 15001 frequency points are chosen, which results in frequency resolution of 1.866 MHz.

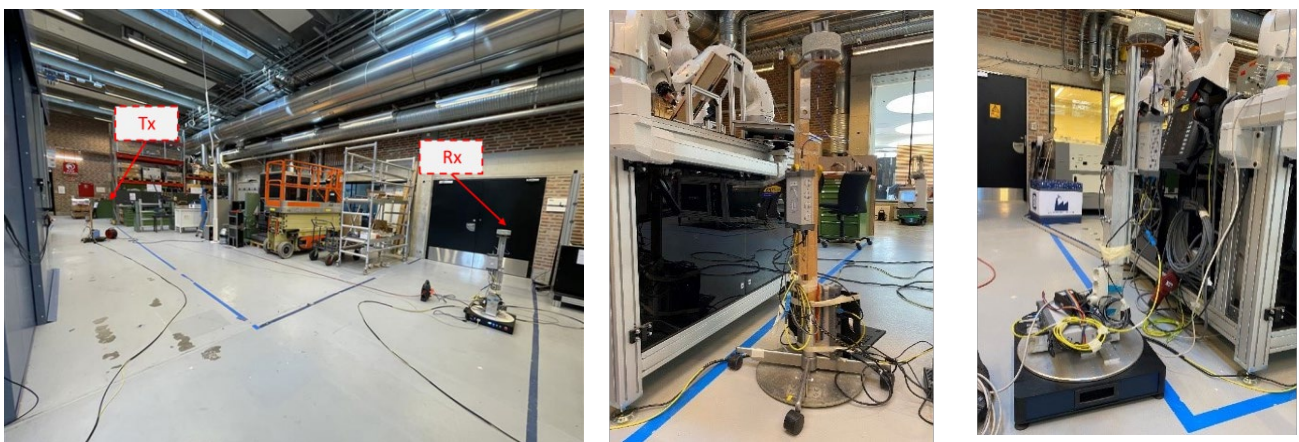
Table 7: Antennas specifications

	Antenna	Radius of UCA [cm]	Number of UCA elements	Height [m]	Number of Tx and Rx locations
Tx	P bi-conical antenna / INFO SZ-2003000.	0	1	1.15	2
Rx	Polarization: vertical. Gain: <ul style="list-style-type: none"> • 3.5 GHz: 1 dB • 11.0 GHz: 3.2 dB • 29.0 GHz: 4.5 dB 	20	180	1.15	1

Table 8: VNA setting

VNA setting	Power [dBm]	Frequency [GHz]	Number of frequency points
	0	2 – 30	15001 for each band

The VAA measurements set-up is presented in Figure 12. The positions of Tx and Rx were selected such that the LOS path is available for all three scenarios.



(a)



(b)

Figure 12. VAA measurement: (a) photos and (b) distribution map of the Tx and the Rx

A classical beamforming algorithm generates array beams in various directions by applying phased array steering factors, which are determined by the configuration of the phased arrays [55]. The measured CIRs and PADPs using classical beamforming are shown for three frequency band in *Figure 13*.

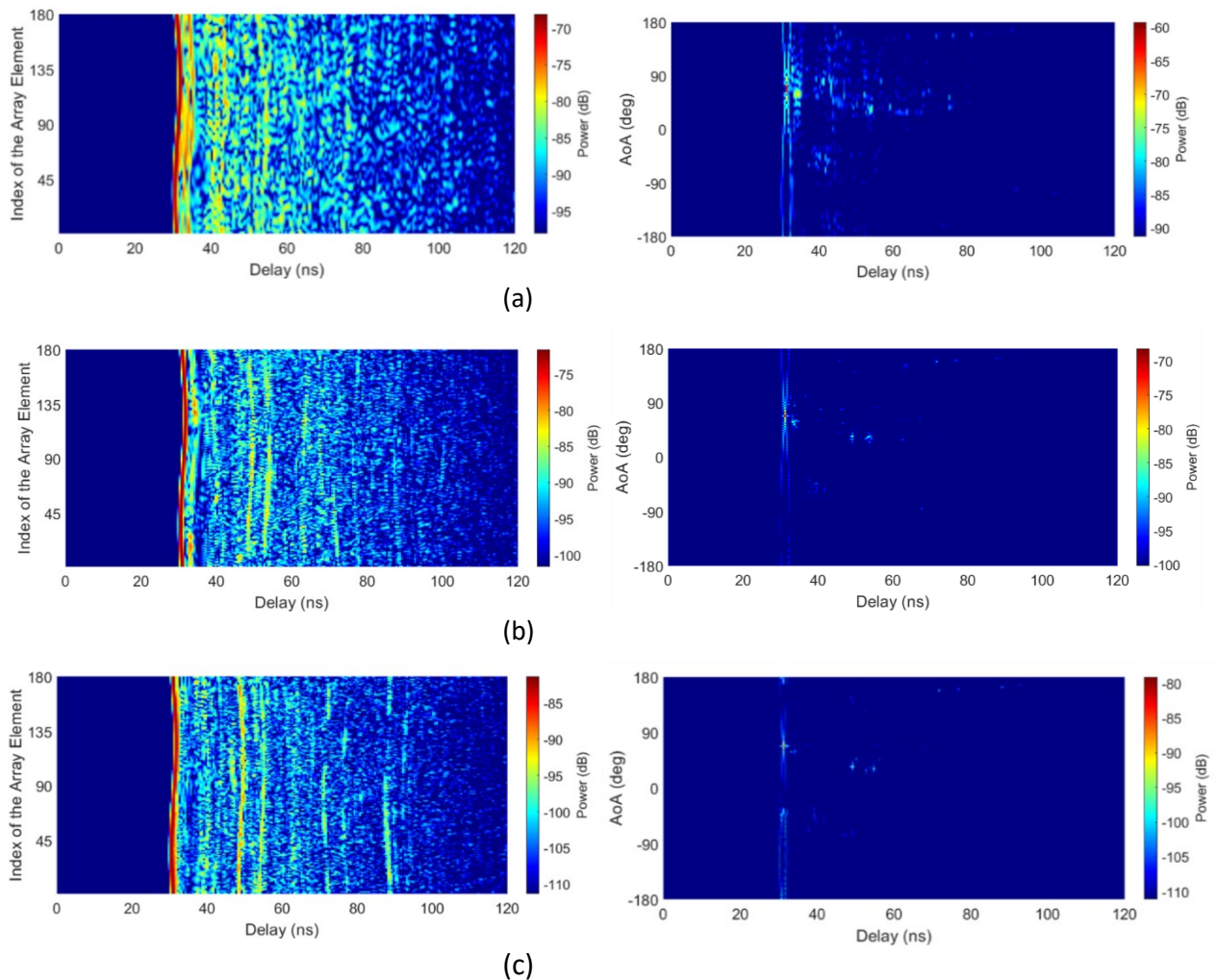


Figure 13. Measured CIRs (left) and PADPs by using classical beamforming (right) in three frequency bands for Tx 1: (a) 2.5-4.5 GHz, (b) 10-12 GHz and (c) 28-30 GHz

The evaluated PADPs identifies a LOS path and few NLOS paths, showing a sparse channel. The flight time of the LOS path between the Tx and the Rx is approximately 30 ns, which results in a distance of 9 m; this agrees well with the measured distance between the Tx and Rx when planning the measurement campaign.

3.2.4 Large-scale VAA

Antennas and VNA setting specifications are presented in Table 9 and Table 10 respectively. Note that number of the UCA elements 1 means that the antenna is at fixed position during the measurement. In this case, the VAA measurement can be classified as a large-scale based on the large radius and number of elements of UCA – 41.5 cm and 360 elements respectively, i.e., the angular interval of the adjacent UCA elements is 1 degree.

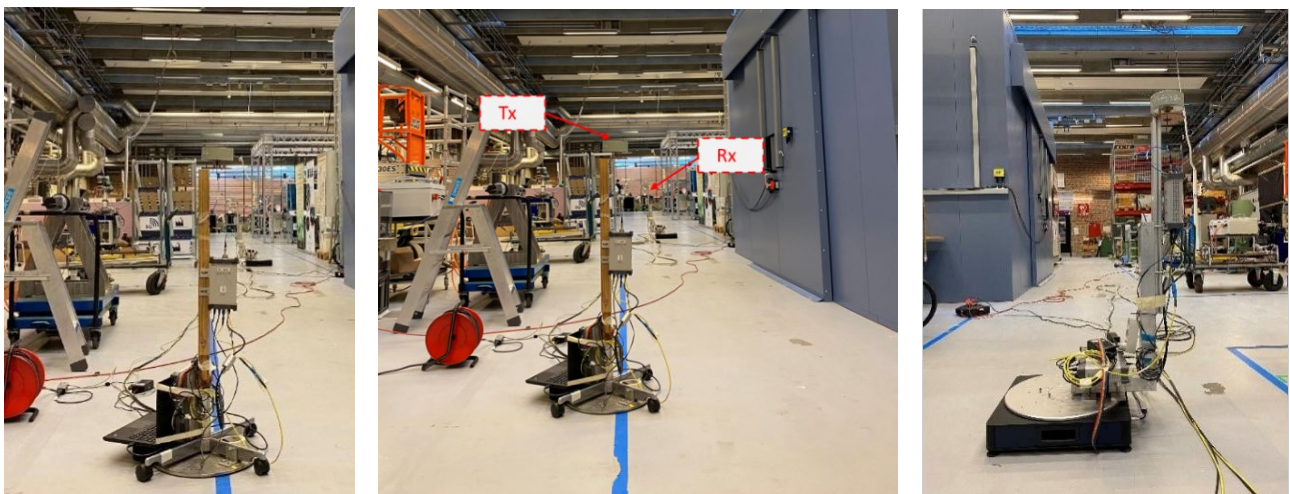
Table 9: Antennas specifications

	Antenna	Radius of UCA [cm]	Number of UCA elements	Height [m]	Number of Tx and Rx locations
Tx	P bi-conical antenna / INFO SZ-2003000. Polarization: vertical. Gain: <ul style="list-style-type: none"> • 3.5 GHz: 1 dB • 11.0 GHz: 3.2 dB • 29.0 GHz: 4.5 dB 	0	1	1.15	1
Rx		41.5	360	1.15	1

Table 10 VNA setting

VNA setting	Power [dBm]	Frequency [GHz]	Number of frequency points
0		Band 1: 2.5 - 4.5 Band 2: 10 – 12 Band 3: 28 - 30	2001 for each band

The large-scale VAA measurements set-up is presented in Figure 14. Due to the long measurement time, only one scenario is investigated, and it involves a LOS path.



(a)



(b)

Figure 14. Large-scale VAA: (a) photos and (b) locations of the Tx and the Rx

The measured CIRs and PADPs using classical beamforming algorithm are shown for three frequency band in Figure 15.

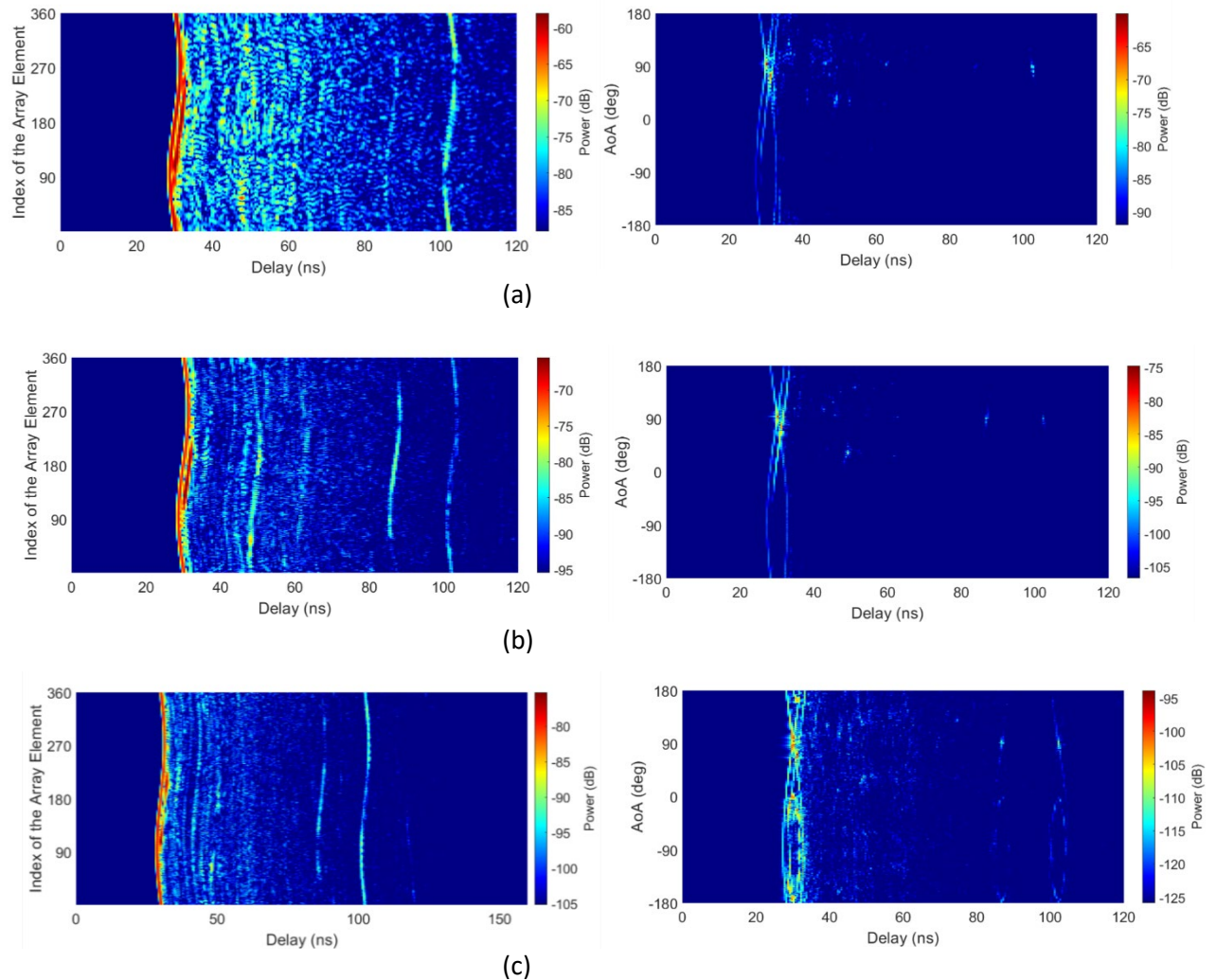


Figure 15. Measured CIRs (left) and PADP by using classical beamforming (right) in three frequency bands: (a) 2.5-4.5 GHz, (b) 12-14 GHz and (c) 28-30 GHz

Initially, the Rx is around 90 degrees to the direction of the Tx. The PADP shows several MPC. However, their power level is over 25 dB lower than the power level of the LOS path. The channel can be considered as sparse as it was in the example in the previous sub-chapter.

3.2.5 Summary

More detailed processing analysis will be presented in the next Section 3.2. The most important points of this sub-chapter can be summarized as follows:

- Preliminary results from wideband measurements in four different scenarios within an industrial environment have been presented. The measured bandwidth is 2 GHz for the spatial map, short-range and large-scale VAA scenarios, while for the VAA scenario the entire frequency band from 2.5 GHz to 30 GHz is measured at once.
- For the spatial map and short-range measurements, the position of both Tx and Rx were fixed during the measurement, allowing only the delay information of MPCs, i.e., PDP, to be resolved.

However, in the other two scenarios – VAA and large-scale VAA, the Rx was rotated in the horizontal plane according to a predefined angle step, enabling both the delay and direction information of MPCs, i.e., PADP, to be resolved.

- For all LOS cases, both the free space path loss and the distance between the Tx and the Rx could be derived from the measured CIRs. The free space path loss derived from the measured CIRs agreed well with the theoretical calculations. The distance between the Tx and the Rx obtained from the measured CIRs accurately matched the actual distance.
- A classical beamforming algorithm was applied to the measured data in the VAA and large-scale VAA scenarios. For both scenarios, a few significant MPC were distinguished in addition to the LOS path, indicating sparse measured channels.

3.3 CHANNEL MODELING FOR SHORT-RANGE INDOOR FACTORY SCENARIOS

The industry is increasingly interested in developing ultra-fast, low-latency networks for industrial environments to support short-range communication networks, such as In-X subnetworks as described in the introduction. In addition to the existing FR1 and FR2 frequency spectrums, there is active research into new spectrums, particularly the mid-band FR3 frequency range from 7 GHz to 24 GHz. The lower end of this spectrum, in particular, has garnered significant attention from the industry. The primary objective of this work is to gain an understanding of the channel through empirical methods for various wireless propagation scenarios, such as indoor industrial scenarios and outdoor urban microcellular scenarios with short communication links. Additionally, we aim to compare the channel statistics for these scenarios with the 3GPP standard channel models [25] [26]. Finally, we present an example channel model following the geometry-based stochastic channel modelling (3GPP) approach and parametrized using the channel parameters extracted from the channel measurements.

3.3.1 Analysed measurement campaigns

The measurement campaigns that are used in this analysis have been described in detail in the preceding Section 3.2.1. However, for readers' convenience, these are briefly summarized in *Table 11*.

Table 11: Summary of measurement campaigns for the indoor factory scenario

Measurement information and parameters	Indoor Factory
Measurement location	Aalborg University (AAU) production lab
Radio frequency [GHz]	2.5 - 4 .5 (FR1)
	10 - 12 (FR3)
	28 - 30 (FR2)
Number of freq. points	2001
Tx & Rx antenna	Bi-conical (omni)
Number of links	254
Dimensions [m]	41 × 17 × 4 (l × w × h)
Link distances [m]	1.3 m – 23.5 m

3.3.2 Data-Postprocessing and Large-Scale Parameters (LSPS) Extraction

Channel frequency responses captured by the network analyser were first modulated with Hanning window to reduce the effects of spectral leakage and discontinuities in the discrete frequency domain measurements. Frequency domain measurements were then transformed into time domain channel impulse responses (CIR) via Fast Fourier Transform (FFT). The overall procedure is sketched in Figure .

In order to capture only meaningful delay-tap information, the noise removal procedure had to be applied to CIRs. Typically noise cut is performed by finding the peak power of a CIR, selecting a certain amount dynamic range down from the peak, e.g., 30 dB, and setting the noise cut power threshold there. For these measurements we noticed that the power variance in the noise range samples was varying between measured positions. For receivers very close to the transmitter, the power variance in the noise range samples was considerably higher than in the Rx – Tx positions with higher distance between them. This may be due to the power scaling in the measurement equipment (VNA). There was also a challenge in separating line-of-sight LOS positions from NLOS positions, which was done by visual observation based on the building layout and transceiver locations. Using a fixed noise threshold across all positions would most likely cause unwanted noise taps to be included into further processing in the case of NLOS Rx – Tx positions.

Therefore, we opted for an alternative way of selecting the noise threshold that is less affected by the noise power variation. We first identify the noise range from delay bins of CIRs where no significant multipath but only noise is expected. Then, we fitted a normal distribution to the real and imaginary components of the noise range samples and calculated a threshold of four standard deviations higher from the mean values of these components. Then, by calculating again the power from the thresholds of the real and imaginary components, the actual noise-cut threshold for the CIRs was determined. Moreover, the samples appearing in longer propagation delays than the higher limit of the noise range were also omitted because no significant multipath were expected to occur on such long propagation delays. This would also eliminate the rising tail -effect resulting from the nature of the Fourier Transform. There is also noise present in the early delay taps of the CIR which is related to the delay and frequency resolution of the measurement equipment. To more accurately capture the earliest multipath, we accepted the first taps according to the following procedure: First the delay tap with the maximum power was identified. Then we searched all the taps within 10 dB power range from the maximum power tap. From this range of taps, the earliest was selected and additional 5 ns was added to accept even earlier taps if their power was above the determined noise cut threshold. By visual inspection, we estimate that the earliest tap was clearly separable from the noise with this procedure.

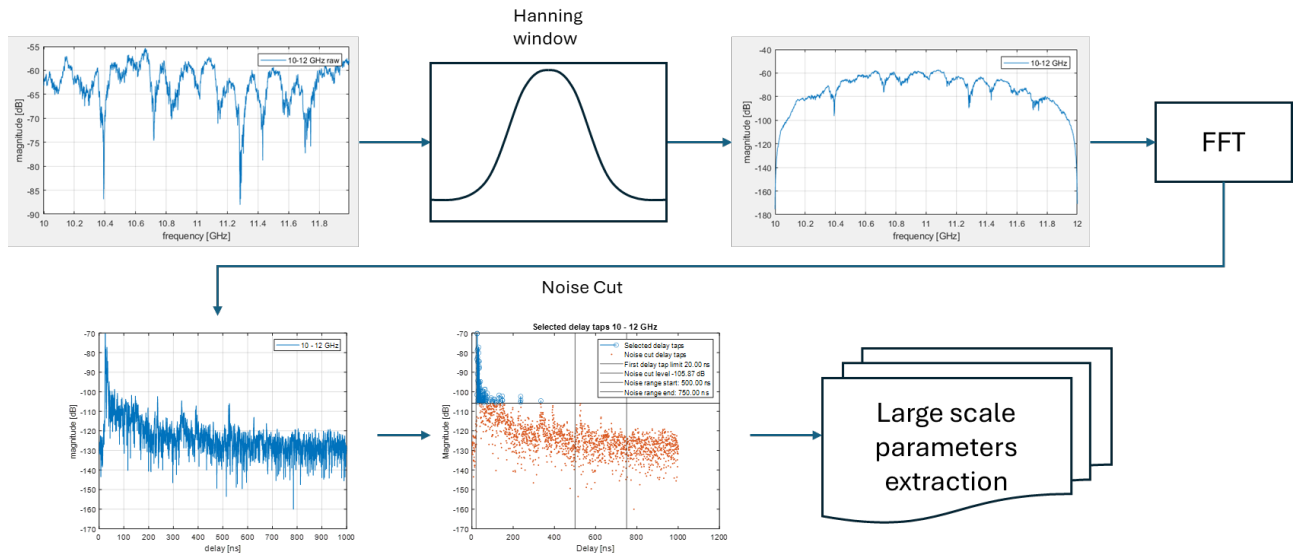


Figure 16. Data preparation flowchart

We calculated large scale parameters: power delay profile (PDP), rms delay spread, Rician K-factor, pathloss and excess pathloss from measurement data.

Power delay profile is defined by taking the selected noise cut delay taps and calculating their power.

RMS delay spread is calculated according to following formulas. RMS delay spread is calculated as:

$$\sigma_{\tau_{RMS}} = \sqrt{\frac{\int_0^{\infty} (\tau - \mu_{T_m})^2 A_c(\tau) d\tau}{\int_0^{\infty} A_c(\tau) d\tau}} \quad (3.1)$$

By first calculating the mean delay as:

$$\mu_{T_m} = \frac{\int_0^{\infty} \tau A_c(\tau) d\tau}{\int_0^{\infty} A_c(\tau) d\tau} \quad (3.2)$$

where $\mu_{T_m}(\tau)$ and $A_c(\tau)$ are the mean delay and channel autocorrelation function (power-delay profile).

For Rician K-factor estimation we used the method of moments introduced by Greenstein [24] by comparing the first and second moments of the average gain of raw non-windowed frequency responses accordingly. In other words, the estimation was performed for each link over the 2001 measured frequency samples.

The overall pathloss was calculated by taking the average gain of raw non-windowed frequency responses of each Rx – Tx pair and removing the effect of added antenna gain in both Tx and Rx side. We also calculated the excess pathloss by subtracting the measured pathloss from the theoretical free space pathloss (FSPL).

3.3.3 Results: Aalborg University Industrial Production Lab

In this section, we present the large-scale channel parameter (LSP) analysis including delay spread, K-factor, and path loss for the Aalborg University Industrial Production Lab scenario. The extracted LSPs

are illustrated through scatter plots (Figure 17-Figure 27) overlaid on the floor plan of the measurement site. A blue pentagram marks the transmitter (TX) location, while coloured triangles represent the receiver locations. The colour intensity of the Rx triangles corresponds to the magnitude of the LSPs according to the respective scales.

3.3.3.1 Delay spread analysis

Measured and estimated rms delay spreads are illustrated for the three measured frequency ranges FR1, FR3, and FR2 in layout plots Figure 17-Figure 19, respectively. Layout of the measurement site is the bottom layer. There are separate sub-figures for each of the three Tx locations. The Tx location is denoted by a blue pentagram and Rx locations with coloured triangles. The colour indicates the rms delay spread in nanoseconds. As expected, we can observe that the delay spread increases with increasing link distance and apparently correlates with the LOS/NLOS condition, at least on the lower frequencies.

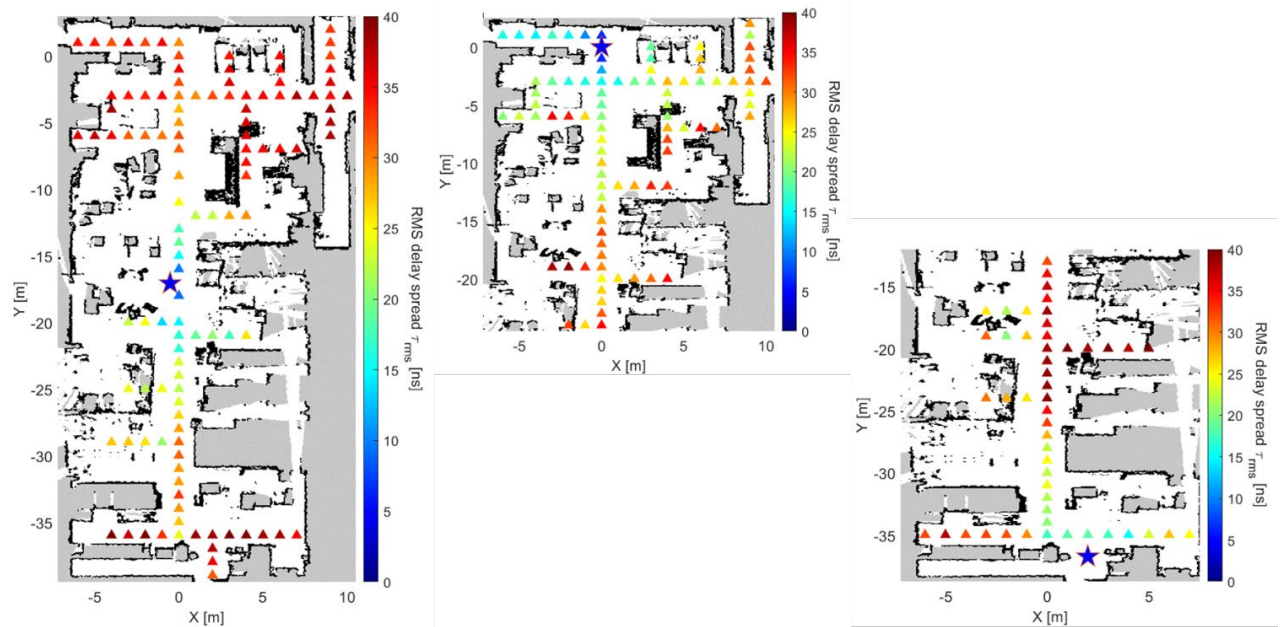


Figure 17. FR1 channel delay spreads in each Rx location (triangle). The three figures from left to right denote the three Tx locations (blue pentagram) in the measurement.

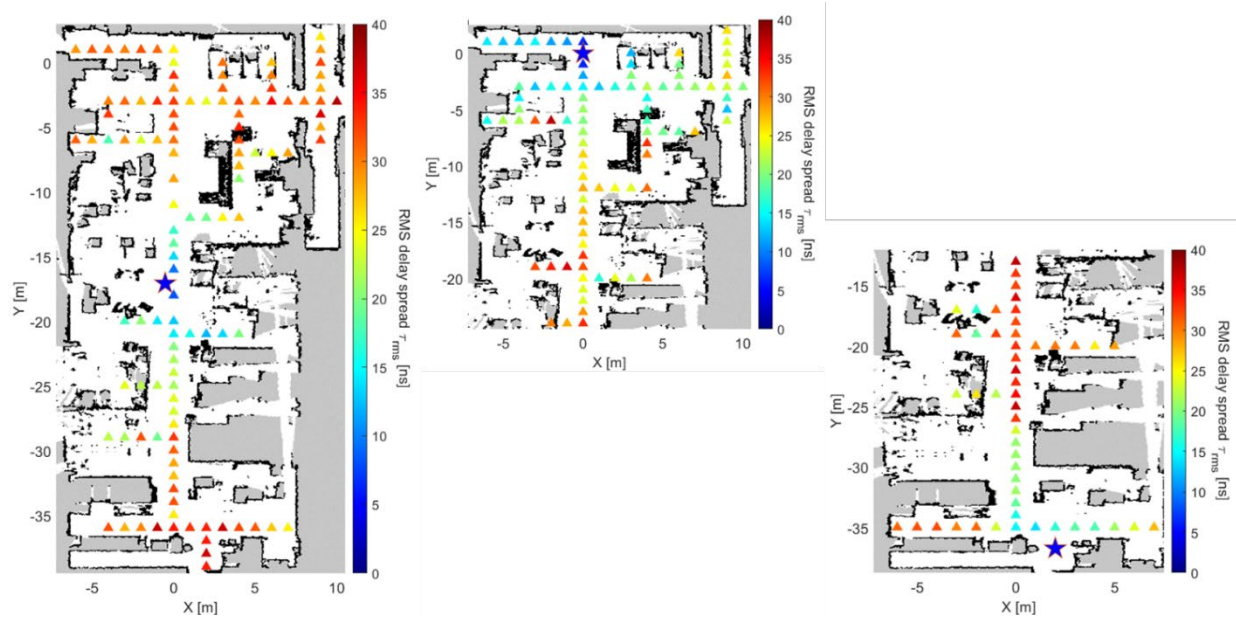


Figure 18. FR3 channel delay spreads

Estimated delay spreads are collected to empirical cumulative distribution functions (CDF) and subsequent curves are illustrated in *Figure 20* for the three frequency ranges. CDF curves are plotted separately for the LOS and NLOS links. Moreover, corresponding delay spread CDF curves from the 3GPP Indoor Factory (InF) model [25] are drawn for comparison. Numerical mean and standard deviation values for FR1, FR3, and FR2 are collected to summary Table 23, Table 24 and Table 25, respectively (see Section 5).

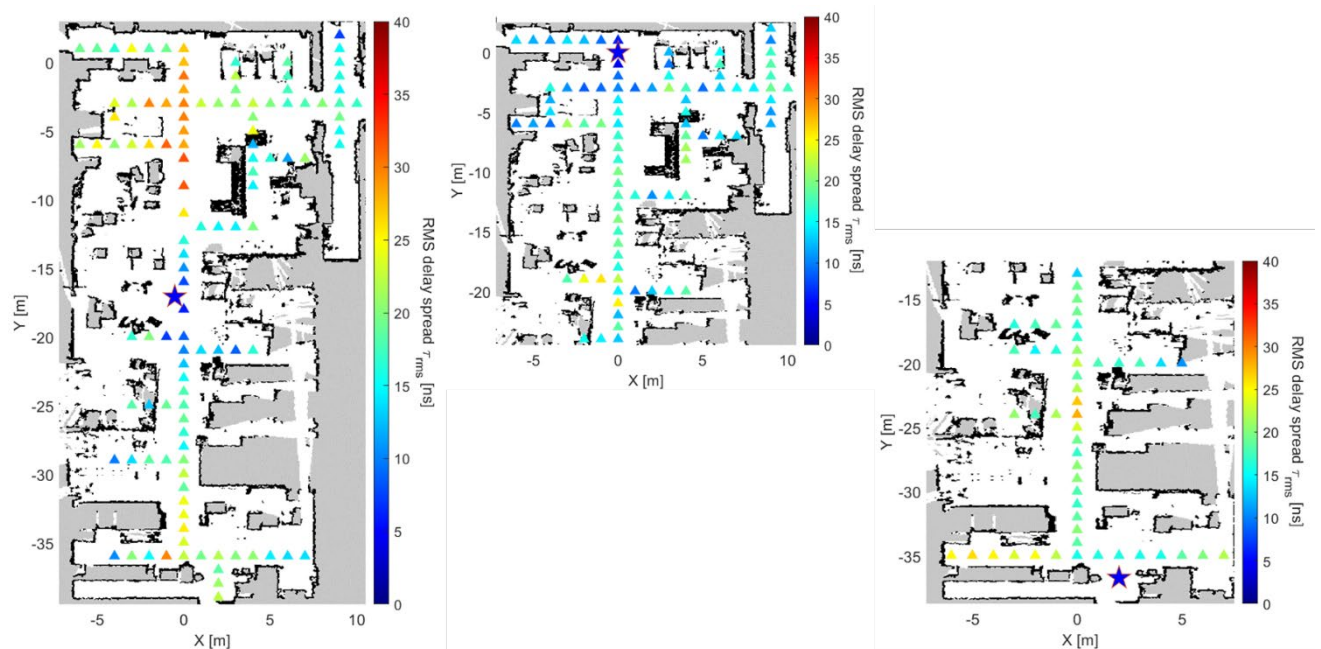


Figure 19. FR2 channel delay spreads

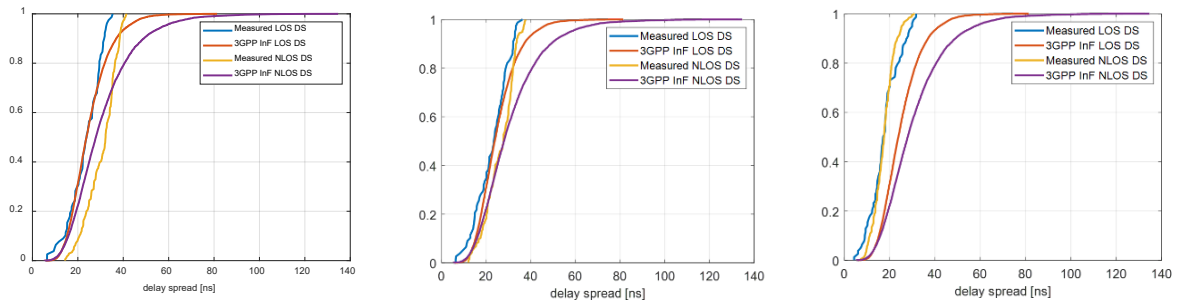


Figure 20. Delay spread CDF FR1 (left), FR3 (middle) and FR2 (right)

Results in *Figure 20* show a good agreement between the measurements and the 3GPP models for the FR1 and FR3 bands, and a slight overestimation of median delay spread values of the 3GPP model in the FR2 band. This can be explained by the fact that the 3GPP model is not frequency dependent and does not adequately account for the increased sparsity of the radio channel at mmWave frequencies. Furthermore, for all frequency bands, the extreme values of the delay spread CDF are never reached: this can be attributed to the peculiarities of the analysed scenario, which has limited dimensions, and in which it is not possible to reach the delay spread values characteristic of very large industrial scenarios.

3.3.3.2 K-Factor analysis

Measured and estimated Rician K-factor values are illustrated for the three measured frequency ranges FR1, FR3, and FR2 in layout plots *Figure 21* - *Figure 23*, respectively. There are separate sub-figures for each of the three Tx locations. The Tx location is denoted by a blue pentagram and Rx locations with coloured triangles. The colour indicates the K-factor in decibels. The shortest links are in LOS state and show higher K-factor. However, many apparent LOS links have even negative K-factor, which probably results from numerous metallic surfaces of the environment providing strong reflections comparable to the LOS path.

Estimated delay spreads are collected to empirical cumulative distribution functions (CDF) and subsequent curves are illustrated in *Figure 24* for the three frequency ranges. Even though the K-factor was estimated for each link, the CDF curves are plotted only for the NLOS links. Moreover, corresponding K-factor CDF curves from the 3GPP Indoor Factory (InF) model [25] are drawn for comparison. When inspecting the CDF curves, we can observe that measured K-factor values are significantly smaller than those of the 3GPP model across the frequency bands. Still, most differences are more observable at FR1. At the median density, the generated 3GPP curve shows more than 5 dB higher K-factor values than the measured data. Overall, the measured K-factor values are more tightly packed closer to the 0 dB range than the reference model, clearly stating that the Rician characteristic of the fading is less evident in this measurement campaign than the 3GPP standard channel model would expect. A typical condition for Rician fading channel is a single dominant path and several weaker ones. A possible explanation for the lower-than-expected K-factor in measured data is the presence of several strong reflected paths from surrounding metallic objects. Numerical mean and standard deviation values for FR1, FR3, and FR2 are collected to summary *Table 23*, *Table 24* and *Table 25*, respectively (see Section 5).

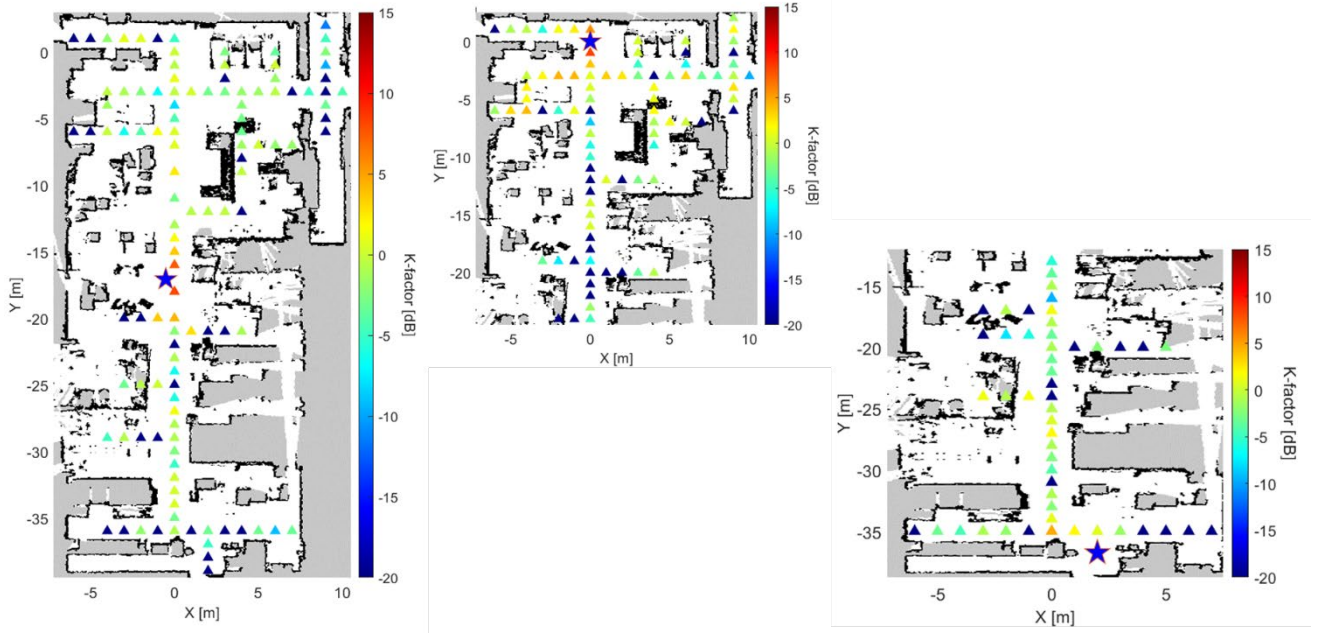


Figure 21. Measured FR1 channel K-factors

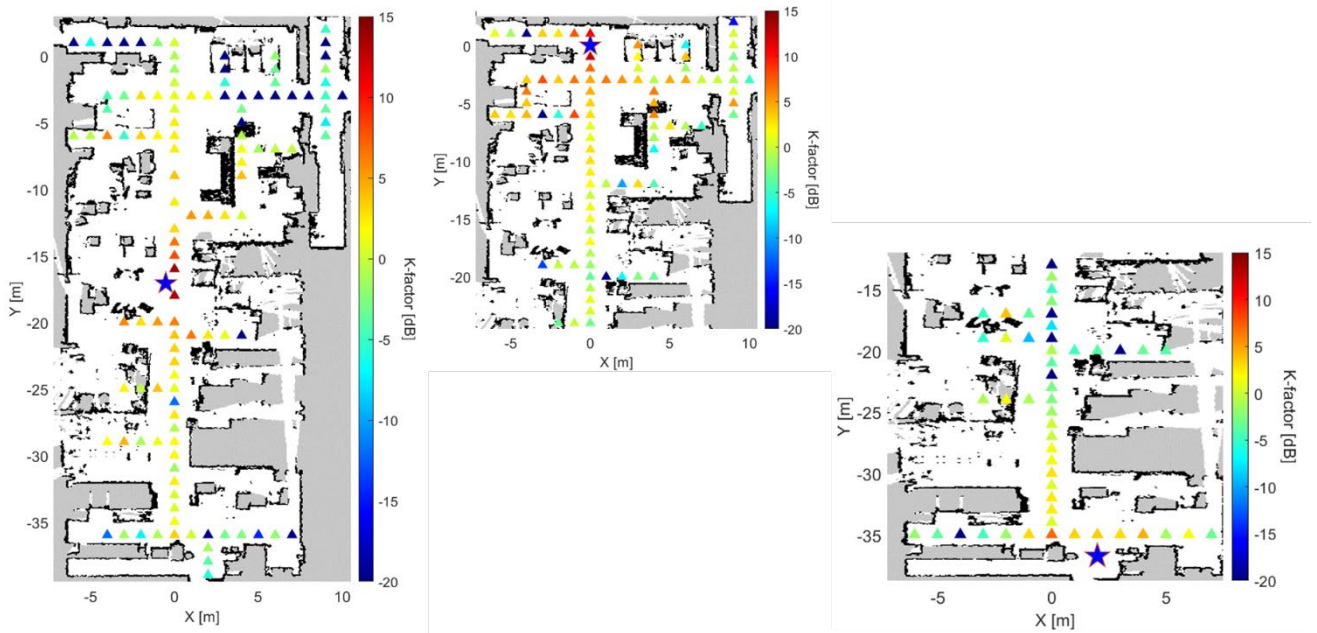


Figure 22. Measured FR3 channel K-factors

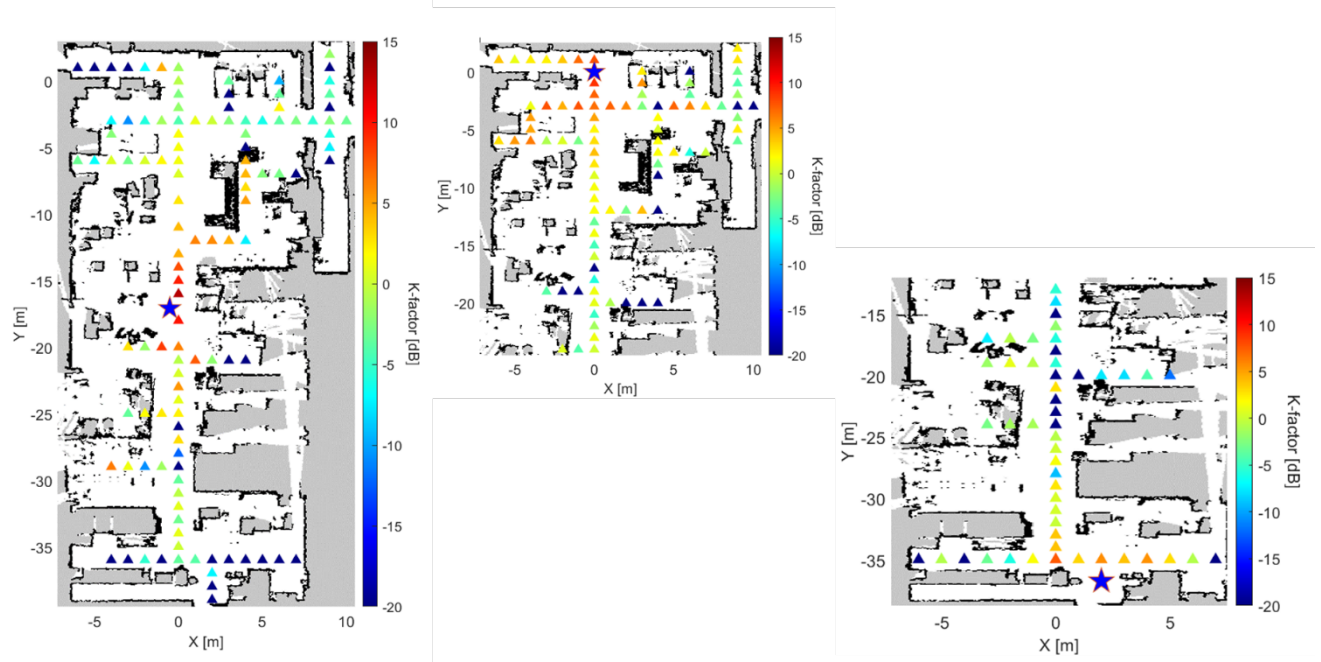


Figure 23. Measured FR2 channel K-factors

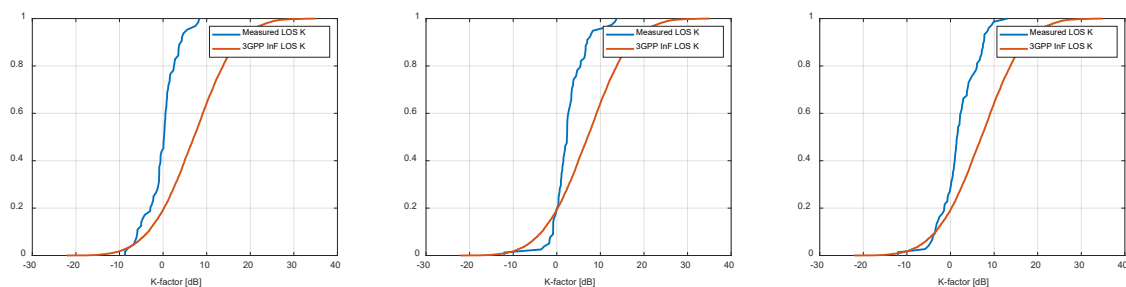


Figure 24. Channel K-factor CDF extracted from FR1 (left), FR3 (middle) and FR2 (right) measurements and comparison with 3GPP

3.3.3.3 Pathloss analysis

Measured and estimated distance-dependent path losses are illustrated for the three measured frequency ranges FR1, FR3, and FR2 in layout plots Figure 25 - Figure 27, respectively. There are separate sub-figures for each of the three Tx locations. A blue pentagram and Rx locations with coloured triangles denote the Tx location. The colour indicates the path loss in decibels. As expected, we can observe that the delay spread increases with increasing link distance and correlates with the LOS/NLOS condition. Estimated path loss values are collected to empirical CDF and subsequent curves are illustrated in Figure 28 for the three frequency ranges. CDF curves are plotted separately for the LOS and NLOS links. Moreover, corresponding path loss CDF curves from the 3GPP Indoor Factory model [25] are drawn for comparison using the link distances of measured links. There are separate curves for 3GPP InF-DL and InF-SL NLOS scenarios while for LOS conditions the model is same for both InF-SL and InF-DL. Numerical path loss exponents and intercepts for FR1, FR3, and FR2 will be analyzed in detail in Section 5 along with the results from measurements in the Campus scenario (see Table 23- Table 25 in Section 5).

Estimated path loss samples, regression lines (floating intercept), and 3GPP path loss model curves are shown in Figure 29-Figure 31. We can observe that the 3GPP InF-DL NLOS curve is completely out of range

and does not characterize the measured environment. InF-SL clearly has better match to the measured values.

Empirical histograms of shadow fading, i.e., deviation between estimated path loss sample and corresponding values of the fitted path loss regression line, are depicted in *Figure 32-Figure 34*. There are separate histograms for LOS and NLOS condition and the three measured frequencies.

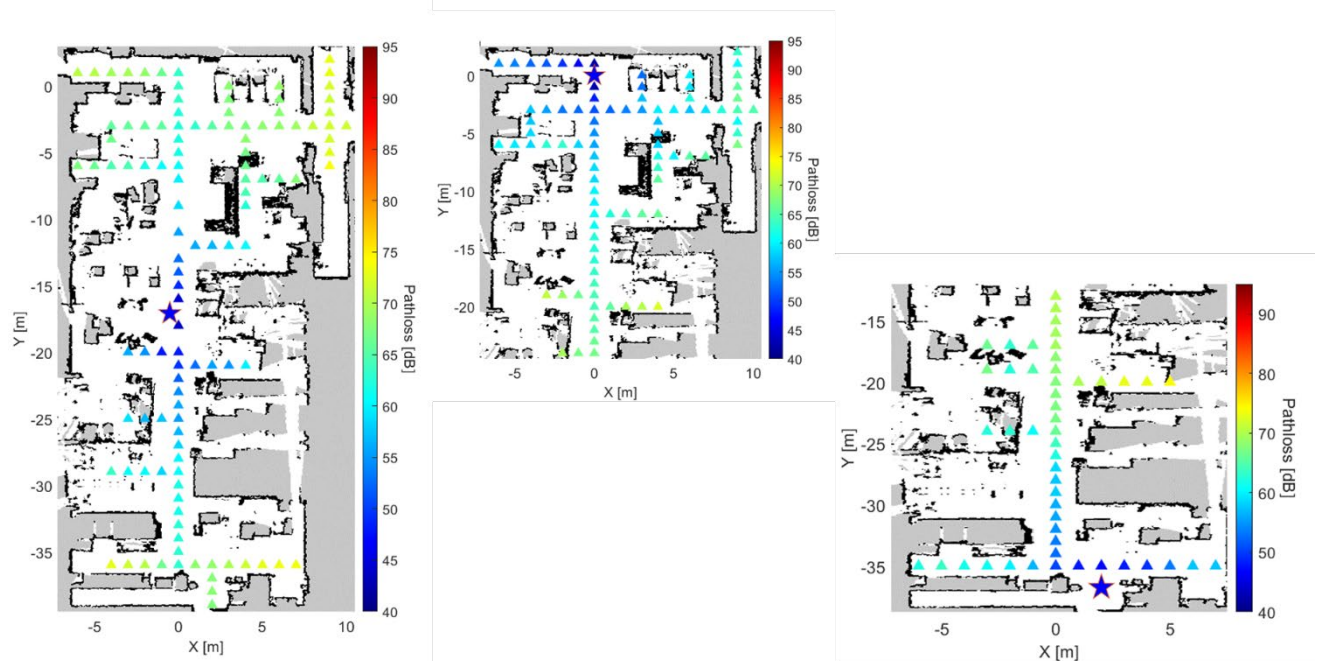


Figure 25. Measured FR1 channel pathloss

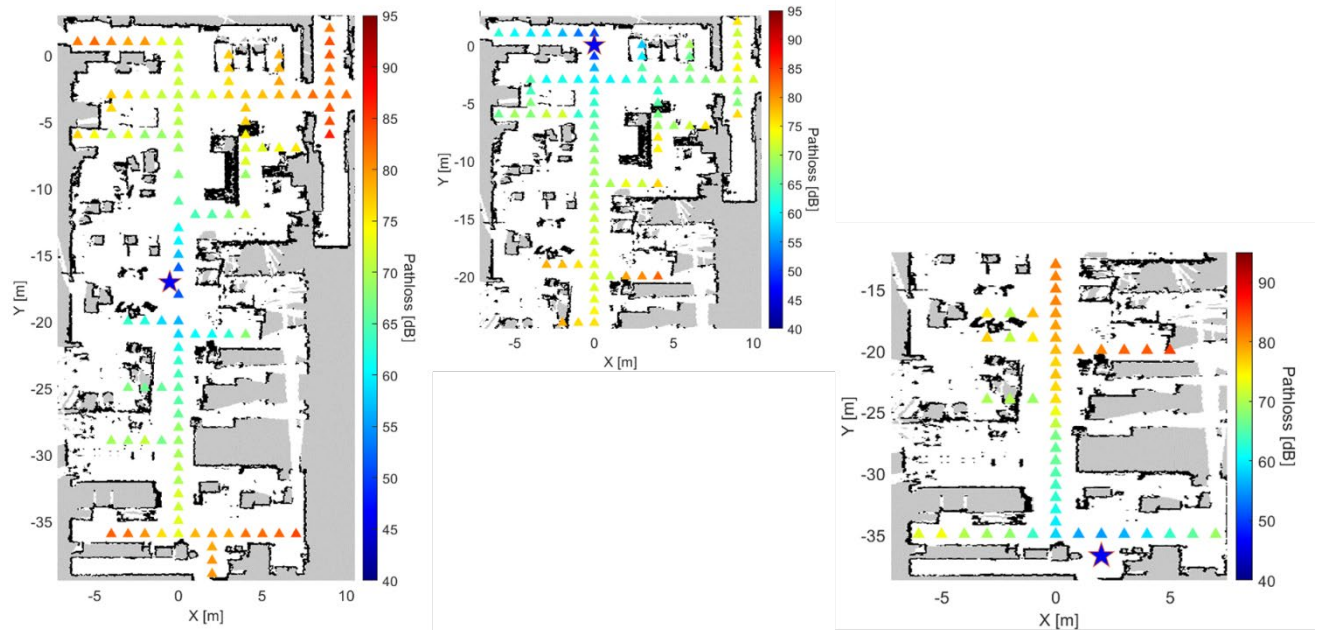


Figure 26. Measured FR3 channel Pathloss

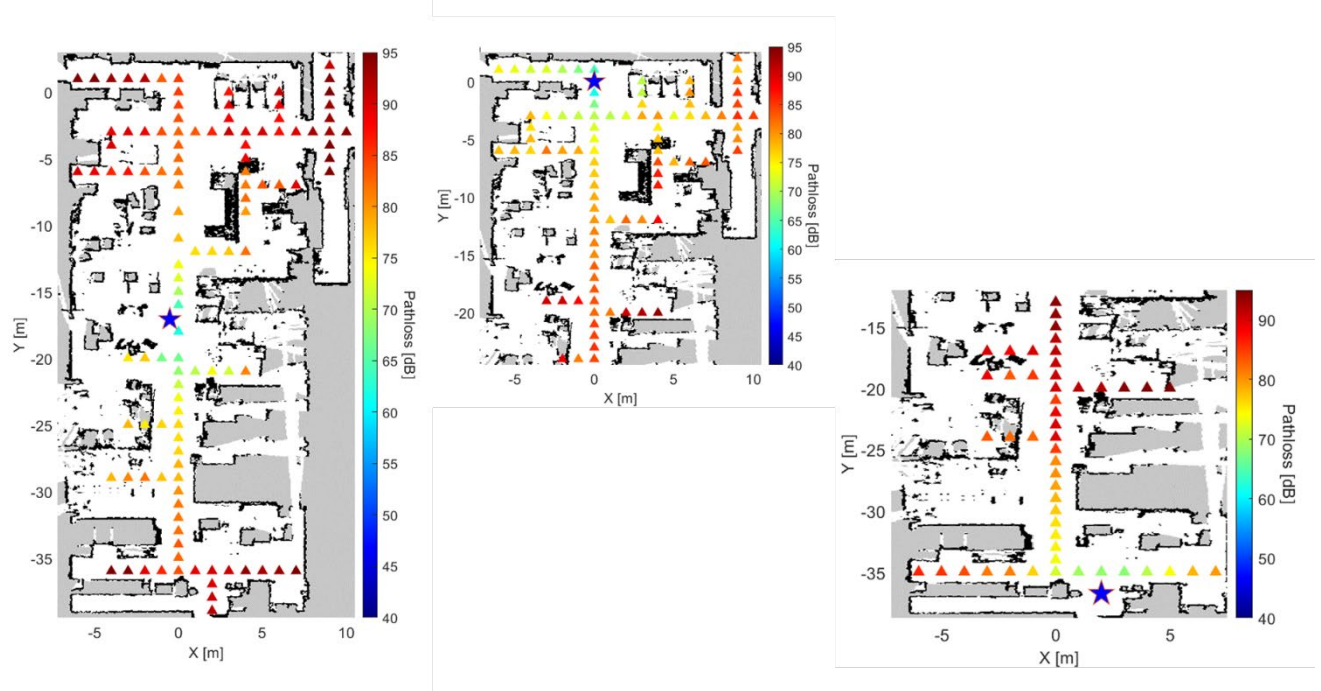


Figure 27. Measured FR2 channel Pathloss

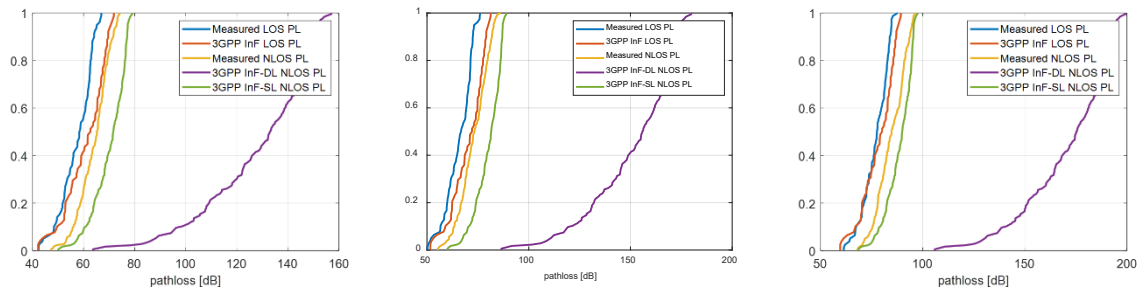


Figure 28. Pathloss CDF extracted from FR1 (left), FR3 (middle) and FR2 (right) from measurements and comparison with 3GPP

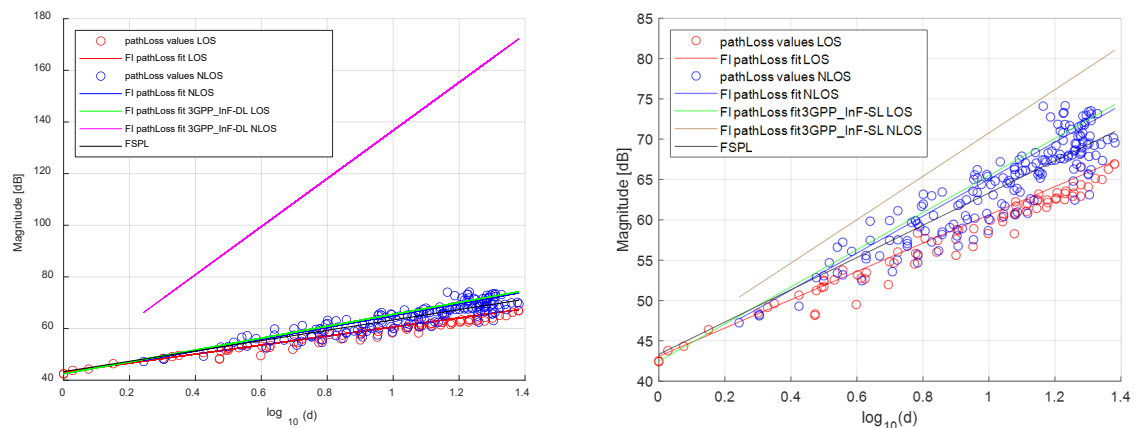


Figure 29. Pathloss floating intercept fit of FR1 channel and comparison with 3GPP InF-DL (left) and InF-SL (right) pathloss models

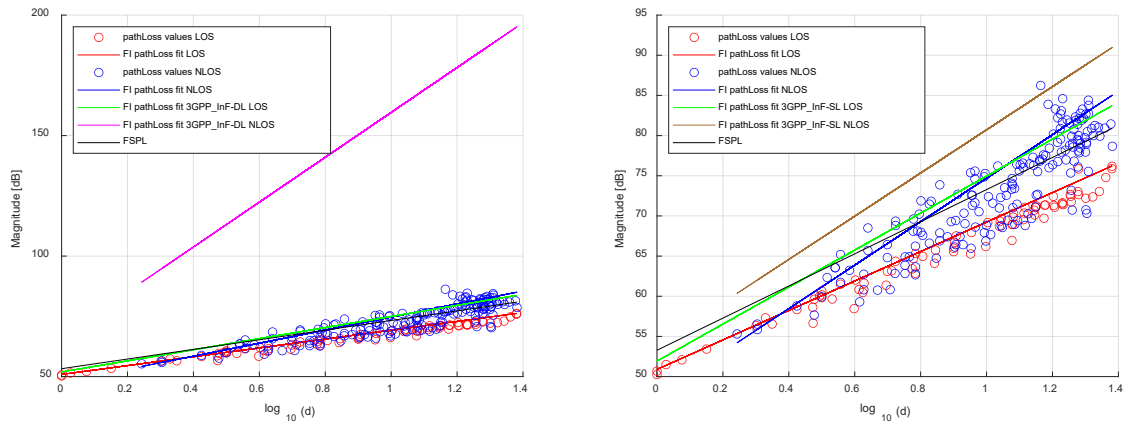


Figure 30. Pathloss floating intercept fit of FR3 channel and comparison with 3GPP InF-DL (left) and InF-SL (right) pathloss models

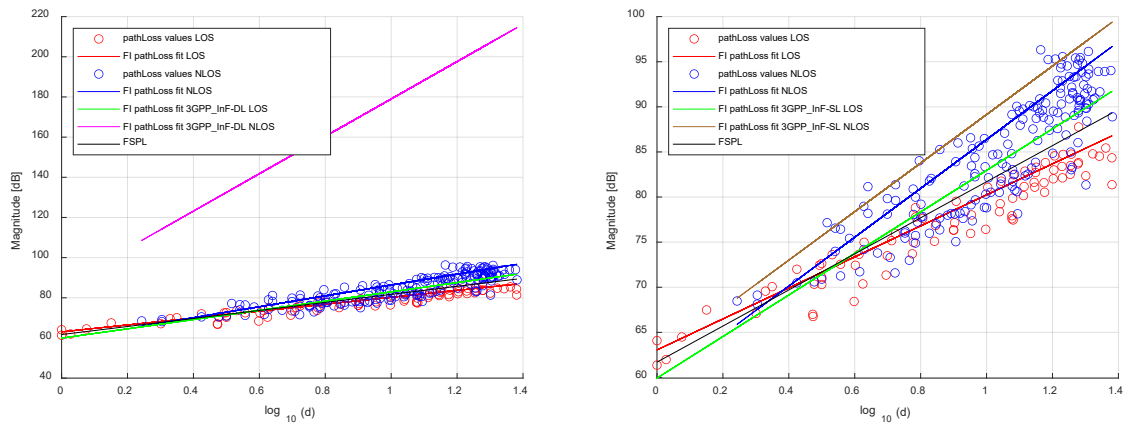


Figure 31. Pathloss floating intercept fit of FR2 channel and comparison with 3GPP InF-DL (left) and InF-SL (right) pathloss models

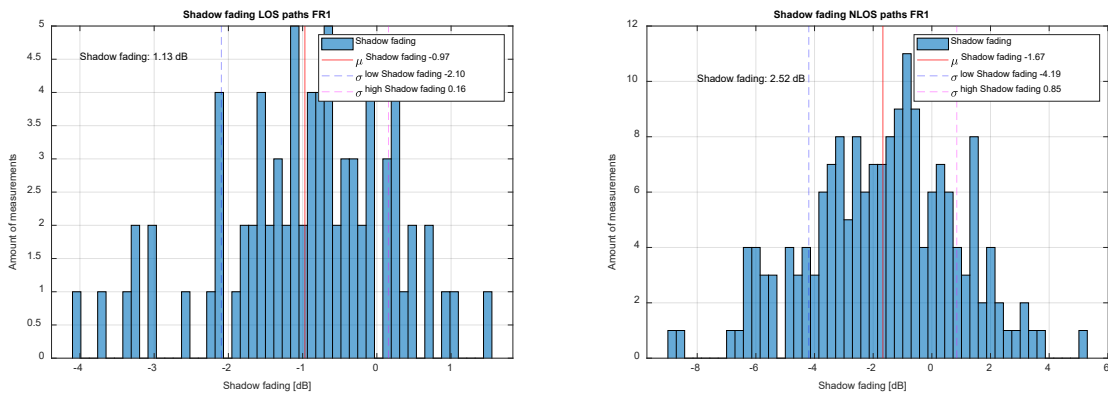


Figure 32. Shadow fading LOS (left) and NLOS (right) for FR1

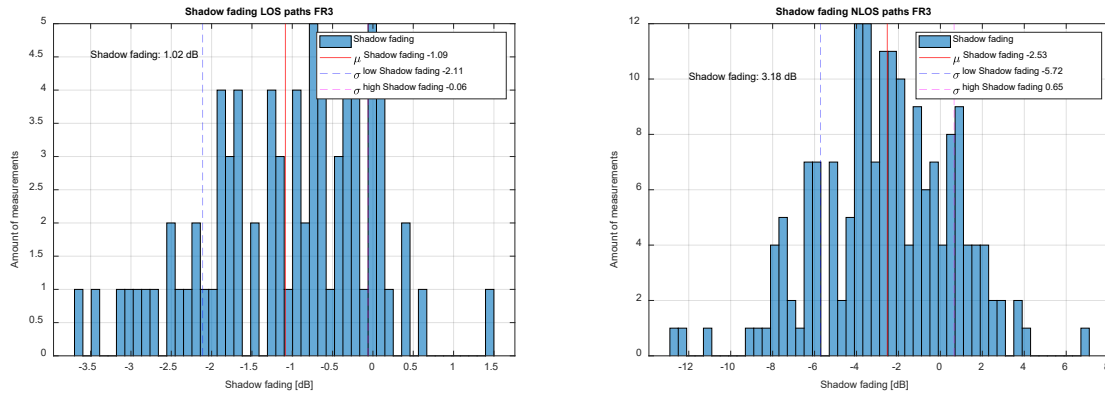


Figure 33. Shadow fading LOS (left) and NLOS (right) for FR3

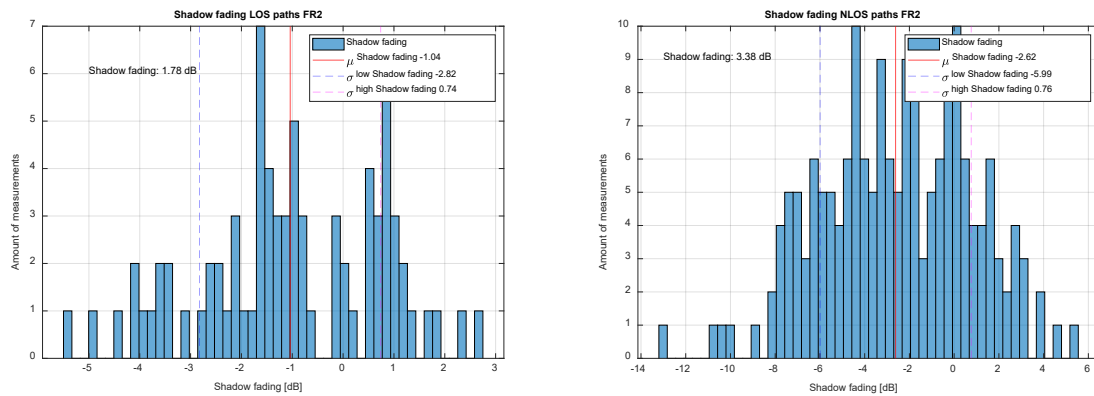


Figure 34. Shadow fading LOS (left) and NLOS (right) for FR2

Figure 34 (left) illustrates the distribution of shadow fading measurements presented as a histogram for LOS at the FR2 frequency band. The shadow fading follows a Gaussian-like distribution with a mean value of approximately 1.78 dB, as indicated by the dashed vertical line. The standard deviations for low and high shadow fading are 2.82 dB and 0.74 dB, respectively, highlighting a higher variability in lower shadow fading regions compared to high shadow fading. The symmetry around the mean suggests that shadow fading in this environment is relatively balanced, although the spread of the data suggests some variability in signal attenuation, likely due to environmental obstacles. This characterization can inform channel modelling and link-budget planning in scenarios with similar shadowing conditions.

Figure 34 (right) represents the distribution of shadow fading measurements in NLOS conditions for FR2, showing a wider and more variable range compared to the LOS case. The mean shadow fading is approximately 3.38 dB, as denoted by the dashed vertical line. The standard deviation is notably different for low and high shadow fading: 5.59 dB for low fading and 0.76 dB for high fading. This indicates that lower shadow fading experiences significantly greater variability, while high shadow fading is more consistent. The broader spread and the presence of extreme values (ranging from approximately -14 dB to +6 dB) suggest that the environment has more complex and diverse propagation conditions, possibly due to significant variations in obstacles and reflectors. These observations are crucial for refining models of shadowing effects in environments with heterogeneous propagation characteristics.

3.3.4 GSCM model parametrization and spatially consistent example channel model from WP5 POC

The large-scale propagation channel parameters (LSPs), including PDP, K-factor, and pathloss extracted from the FR3 measurements described in Section 3.3.3 were complemented by the spatial parameters of [25] indoor factory dense clutter (InF-DL) channel model for the given link geometries, i.e., TX-RX locations. The collection of these parameters was then applied to the TX- RX locations trajectory from LOS to NLOS conditions, as depicted in Figure 35, by utilizing the Keysight Channel Studio Geometric Channel Modelling (GCM) software tool and generating a spatially consistent and time-continuous dynamic channel model following the [25] implementation recipe. The model was then emulated with the state-of-the-art Keysight FR3 low-latency PROPSIM channel emulator and channel characteristics, such as PDP and Doppler spectrum were validated using Keysight PNA-X Network Analyser and Keysight UXA Signal Analyser, respectively. The validation setup is shown in Figure 36. The validation results for PDP and Temporal Autocorrelation Function are illustrated in Figure 37 to Figure 38 where the measured and modelled characteristics perfectly match. This demonstrates the measurement and modelling accuracy of the Keysight software and hardware. The Doppler spectrum for the derived channel model over the UE route is also shown in Figure 39.

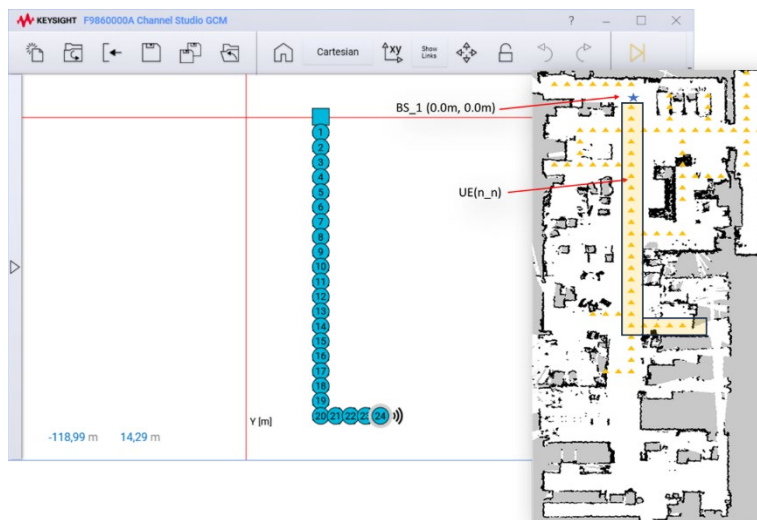


Figure 35. Channel model implementation in F9860000A Keysight Channel Studio GCM.

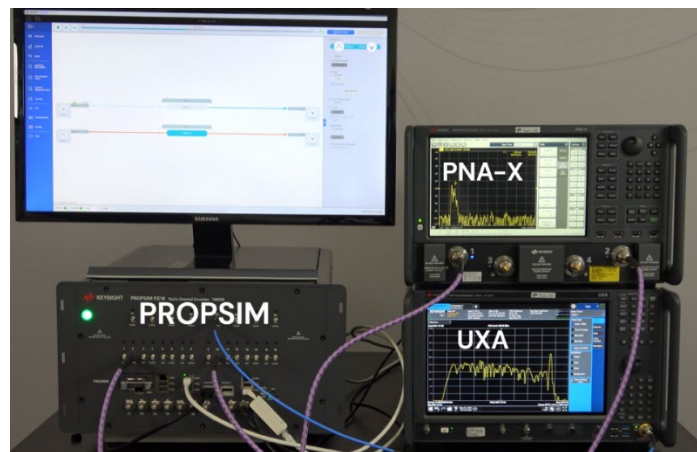


Figure 36. Emulating generated channel model with Keysight low-latency F8820B PROPSIM channel emulator and validating model characteristics with Keysight N5247B PNA and N5247B UXA.

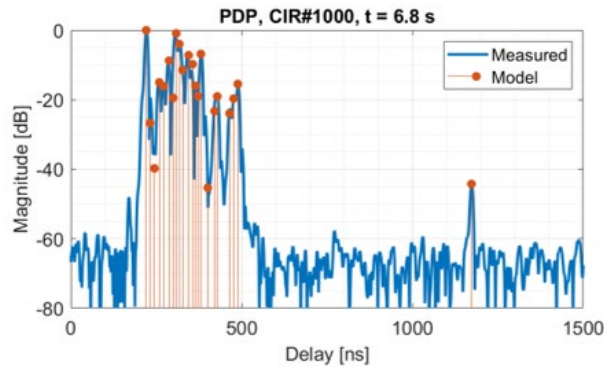


Figure 37. PDP validation for RX position no. 6 (from Figure 80) of the derived channel model.

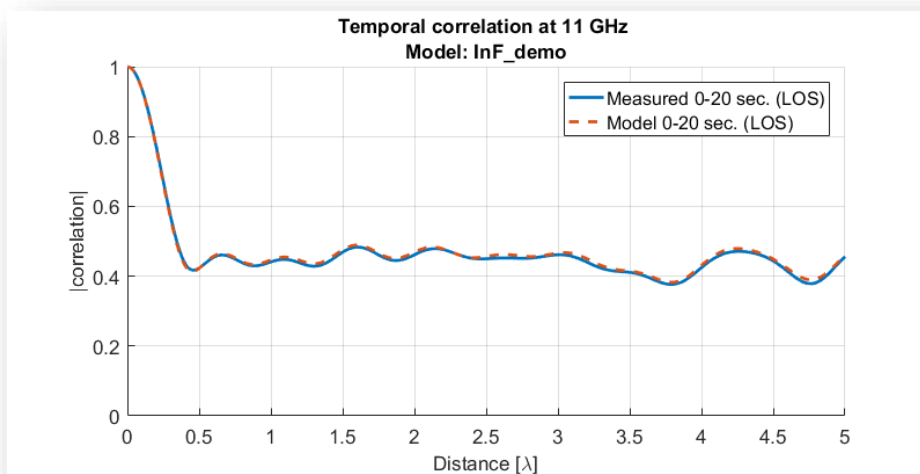


Figure 38. Model and measured Temporal Autocorrelation Function (TCF) for the derived channel model over the UE route.

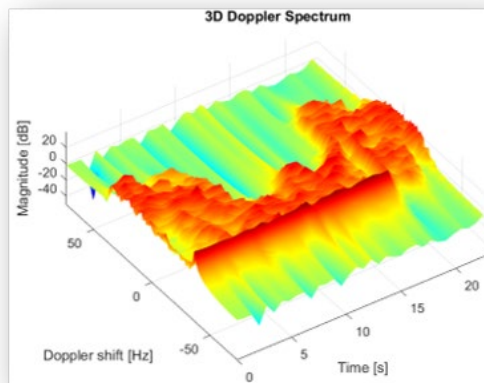


Figure 39. Measured Doppler spectrum for the derived channel model over the UE route.

3.3.5 Summary

In this section, we have analysed channel transfer functions measured in a factory-like production lab located at Aalborg University at FR1, FR2, and FR3 frequency bands, using a vector network analyser and omnidirectional antennas. The objective was to study radio propagation in industrial environments at the so-called bands for short-range communication scenarios. We found general trends of increasing delay spread, Rician K-factor, and path loss with increasing link distance. This is not a surprise, since the last one is evident by definition, and the two former observations are well aligned with similar studies on various radio frequencies. We compared measured large-scale parameters: delay spread, Rician K-factor, and pathloss against their corresponding 3GPP Indoor factory reference models by comparing empirical CDFs. Measured delay spreads were found to match the reference model in the median range densities. Measured K-factors were overall found to be quite low reaching 10 dB only in the most extreme cases. This indicates that even in the clear LOS condition the LOS component does not dominate. Instead, there are several strong paths in addition to the LOS path. It can be presumed that the strongly reflecting metallic structures in the industrial hall provide a rich delay spread without attenuating the gain of these delayed paths significantly. Therefore, the power ratio of the strongest LOS paths remains close to those of the reflected paths. The reference model K-factors were found to be overall some 5 – 10 dB higher than the measured values. The measured pathloss for the densely cluttered reference model was found to be significantly higher than the measured pathloss, indicating that the densely cluttered reference model does not characterize the measured environment, which has large open spaces and corridors. For the sparsely cluttered reference model, the difference was less compared to the measured values but still some 10 dB higher.

4 PROPAGATION MEASUREMENTS AND MODELLING FOR IN-VEHICLE AND OUTDOOR2VEHICLE SCENARIOS

In order to make the communication between wireless nodes in a vehicle feasible, it is necessary to investigate the characteristic of radio propagation in short-range and cluttered environments such as the different zones, spaces and technology components inside a car.

However, at the moment in the literature there are only a few studies related to propagation for in-vehicle sub-networks. In the present chapter, the outcomes of several measurement campaigns are presented with the aim of providing beyond-state of the art knowledge on radio channel characteristics in in-vehicle and outdoor-to-vehicle scenarios. Such measurement campaigns and studies have been carried at AAU and CNIT and they complement each other, as different kind of vehicles are analysed, with different configurations and locations of Tx/Rx and antennas, and involving multi-band investigations, with frequencies ranging from below-6GHz, up to the sub-THz bands (99-101 GHz, and 110-170 GHz, also known as D-band).

4.1 IN-VEHICLE MEASUREMENTS AT AAU

The results presented in this sub-chapter are based on the work in [2], summarizing the studies on in-vehicle propagation carried out at AAU in the framework of the 6G-SHINE project. In-vehicle wireless networks are important for improving smart transportation systems and interaction among vehicles and their users. However, few works in the current state of the art were found to analyse the in-vehicle channel characteristics in multiple frequency bands [3] - [11], [64]. In the current work, the focus is on the bands below 7 GHz and millimeter-wave (mmWave) band. Different locations distributed across the engine compartment of both the van and car were chosen to measure the CIRs.

Two vehicles were used in the measurements: a van (Ford Transit Custom model) and a car (Benz B200d model). The presented in-vehicle channel measurements are divided into two groups:

- The first group measurements are conducted in the engine bay and aim to study the channel impulse responses (CIR) and delay characteristics.
- The second group measurements are conducted in the passenger cabin and aim to study the power-angle-delay profile (PADP) and angular spread.

The first group of measurements, conducted in the engine bay, is essential for understanding wireless communication between sensors and control units. The second group of measurements, conducted in the passenger cabin, is crucial for studying wireless communication interactions among vehicles and the people inside the car.

S_{21} for each pair of Tx antenna and Rx antennas were recorded using R&S ZNA43 VNA. To calibrate the system response before data collection, back-to-back measurements were performed. The channel measurements were conducted in two different bands. A summary of the measurement settings and antenna specifications is shown in *Table 12*.

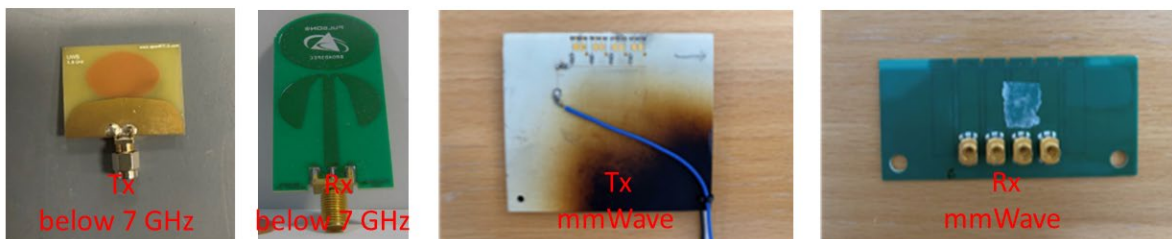
Table 12: Specification of the engine bay measurements

Parameters	Below 7 GHz	mmWave band
Frequency band [GHz]	4-6.5	25-27.5

Frequency points	626	
Bandwidth [GHz]	2.5	
Transmitted power [dBm]	10	
IF bandwidth [Hz]	1000	500
Tx antenna type	planar monopole	endfire antenna
Tx antenna gain [dBi]	0.82	3.8
Tx antenna HPBW [°]	elevation: 65 azimuth: omni directional	elevation: 60 azimuth: 90
Rx antenna type	planar monopole	endfire antenna
Rx antenna gain [dBi]	3	-0.3
Rx antenna HPBW [°]	elevation: 70 azimuth: omni directional	elevation: 70 azimuth: 100

For both bands, the measured frequency bandwidth is 2.5 GHz with 625 frequency points, which results in a 0.4 ns delay resolution. A delay range of 250 ns would allow a maximum measurement range of 75 m. With the increase of frequency, a lower intermediate frequency (IF) bandwidth is used to maintain a better dynamic range of the measurement system. The selection of the antennas to be used in the engine bay scenario is challenging, because the physical size of the antennas must be small enough to secure an easy installation in the engine bay. Moreover, the antenna patterns used in both frequency bands must be similar to eliminate the effects of antenna patterns on the measured results. The photos of the antennas used for both frequency bands in the channel measurements are shown in *Figure 40*.

Antennas for the measurements in the engine bay



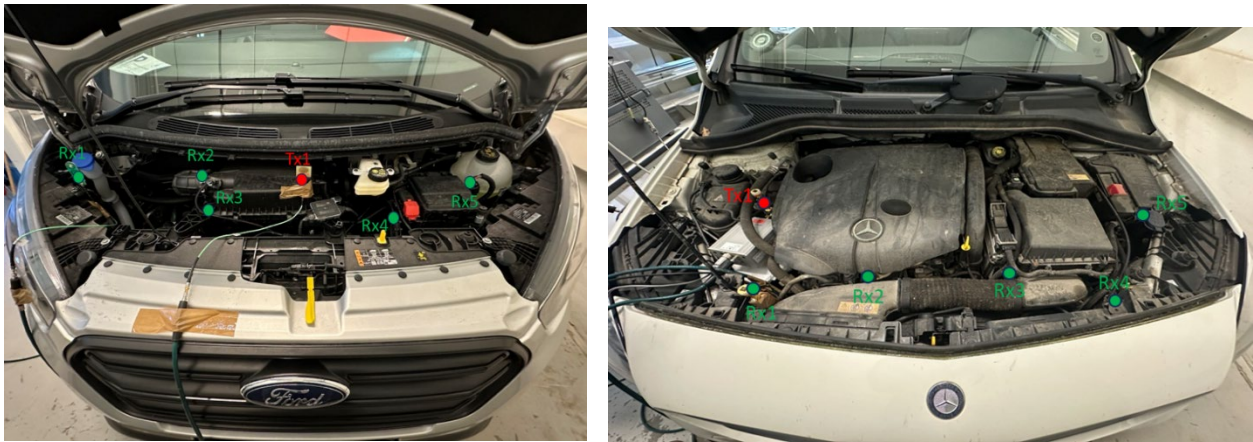
Antennas for the measurements in the passenger cabin



Figure 40. Photos of the antenna used in the measurement campaigns

For measurements in the lower frequency band, planar monopoles and biconical antennas, both with omni-directional patterns in the horizontal plane are employed. Endfire antennas with wide half power beamwidth (HPBW) in both horizontal and vertical planes are chosen for the measurements in mmWave bands owing to the lack of small omni-directional antennas in the mmWave bands. Note that all employed antennas are vertically polarized.

During the measurement within the engine bays of both the van and the car, the Tx is fixed while the Rx is moved to 5 different locations, as indicated in *Figure 41*. To approximate the realistic scenarios, vehicles hood was closed during the measurements in the engine bay.



(a)

(b)

Figure 41. Measurement locations in the engine bay of the (a) van and (b) the car

For estimating and improving the link budget and data rate in wireless networks using multi-antenna systems, spatial information about the MPCs is of importance. To evaluate the channel spatial profiles for different scenarios inside the vehicle, directional scanning schemes presented in [12] and [13] were used. The measurement system is illustrated in *Figure 42*.

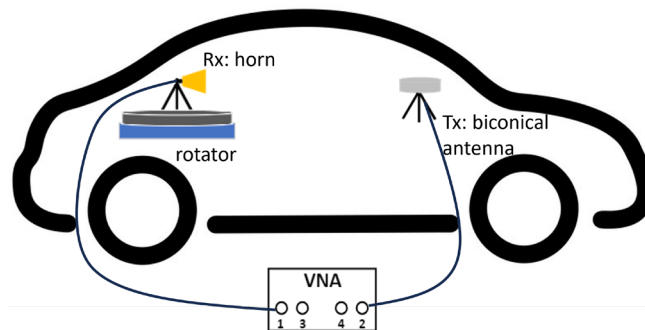


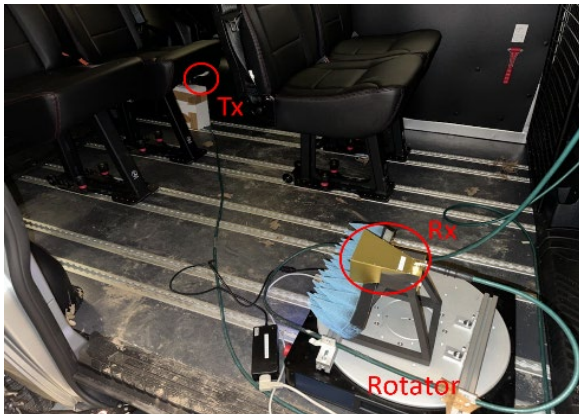
Figure 42. Diagram of the measurement system for measurements in the passenger cabin

A biconical antenna [14] with omnidirectional pattern in the azimuth plane was used as Tx antenna. It operates in both the lower frequency and mmWave bands. Moreover, two horn antennas [15] were selected as Rx antennas for both bands. The photos of the antennas were shown in *Figure 40*. The Rx antenna was mounted on a rotator. During the measurement, the Tx antenna was fixed while the Rx antenna was rotated in azimuth plane with a step of 10° . For each orientation of the Rx, the channel frequency response was measured by the VNA for each band with 501 frequency points. Further details about the measurement settings and the antenna specifications are summarized in *Table 13*.

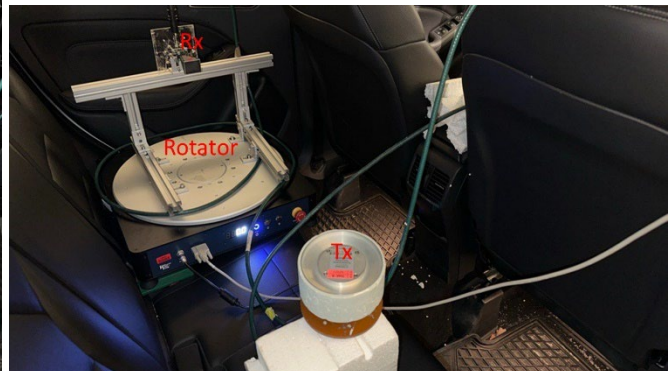
Table 13: Specification of the channel spatial measurements

Parameters	Below 7 GHz	mmWave band
Frequency band [GHz]	4.4-6.4	28-30
Bandwidth [GHz]	2	
Frequency points	501	
IF bandwidth [Hz]	1000	500
Rotation step [°]	10	10
Tx antenna type	biconical antenna	
Tx antenna gain [dBi]	4	4
Rx antenna type	horn antenna	
Rx antenna gain [dBi]	10	20
Rx antenna HPBW [°]	azimuth: 38	azimuth: 17
Scenario	van: LOS car: LOS	van: LOS car: LOS

The measurements in the passenger cabin were conducted in a LOS scenario for both the van and the car. The scenarios inside the van and the car were denoted as scenario 1 and 2 respectively. In scenario 1, both the Tx and Rx antennas were located on the floor of the passenger cabin as illustrated by *Figure 43 (a)*. In Scenario 2, the Tx and Rx antennas were positioned on the passenger seats of the car, as shown in *Figure 43 (b)*.



(a)



(b)

Figure 43. Photos of the channel spatial measurements in (a) Scenario 1 and (b) Scenario 2

Equations for estimation of the CIR, the RMS delay spread and the PADP can be found in [16]. The measured CIRs for seven pairs Tx-Rx are presented in *Figure 44*.

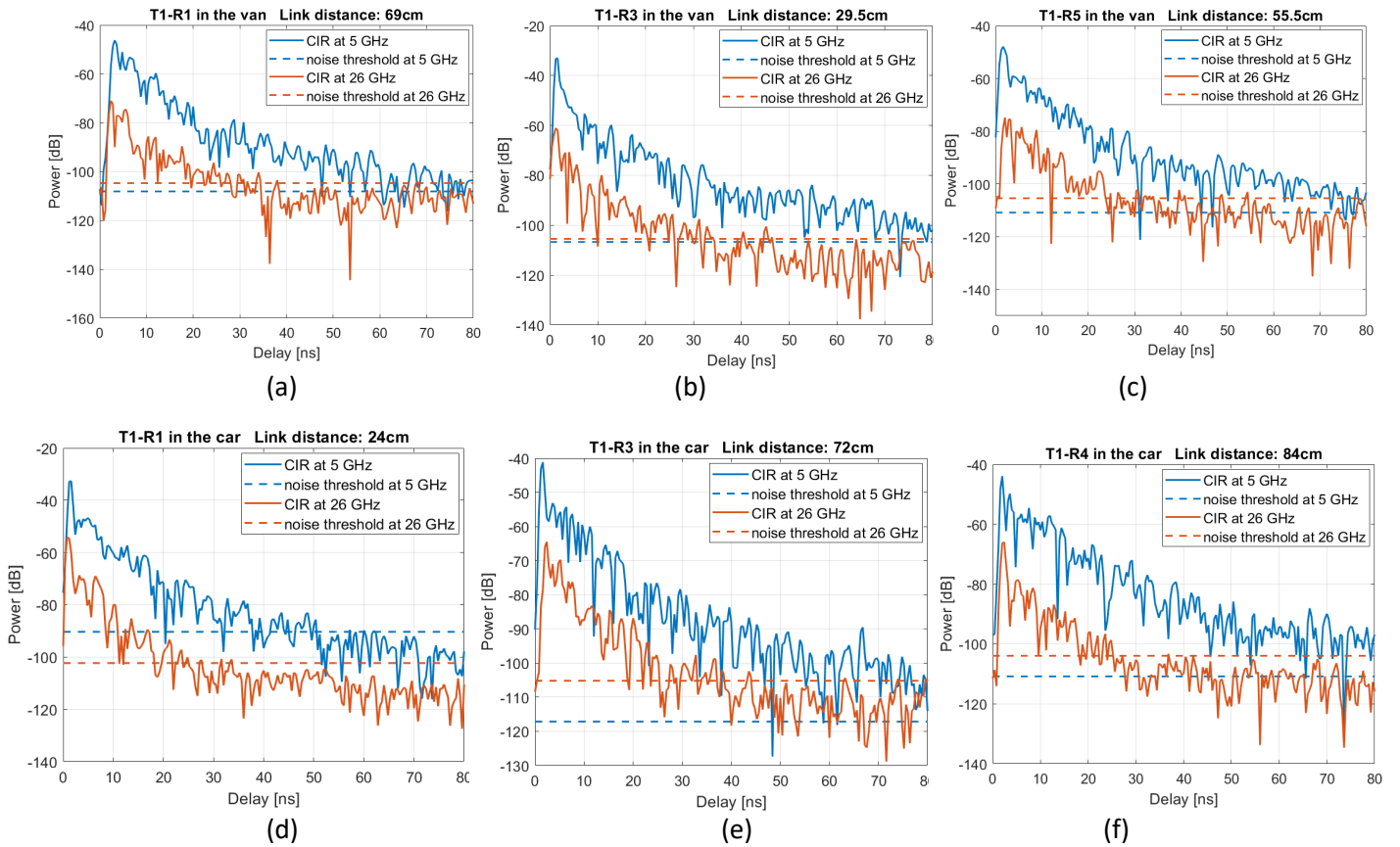


Figure 44. Measured CIRs for (a) Tx1-R1 in the van, (b) Tx1-Rx3 in the van, (c) Tx1-Rx5 in the van, (d) Tx1-Rx1 in the car, (e) Tx1-Rx3 in the car and (f) Tx1-Rx4 in the car

As one could expect, for the measurement with Tx1-Rx3 in the engine bay of the van, the power of the LOS path is much larger compared to the other multipaths, because there is less scattering within such a short distance. Similar results can also be observed for the measurements with Tx1-Rx2 / Rx4 in the engine of the van. When the link distance is longer, e.g., Tx1-Rx1/R5, the MPC reflected by the ceiling of the van and the paths scattered by the edge of the inner objects become more emphasized. The depth of the engine bay of the van is larger than that of the car and the components of the engine are distributed with different heights, which results in a more complicated and rich propagation scenario and CIRs with various shapes. For the Tx1-Rx1/Rx2 pairs, the CIRs measured in the engine bay of the car have a strong LOS path and several weak MPCs due to the small distance. However, with the increase of the distance between the Tx-Rx pair, the MPC becomes more recognizable in comparison with LOS path level, i.e. the case for the pair Tx1-Rx4.

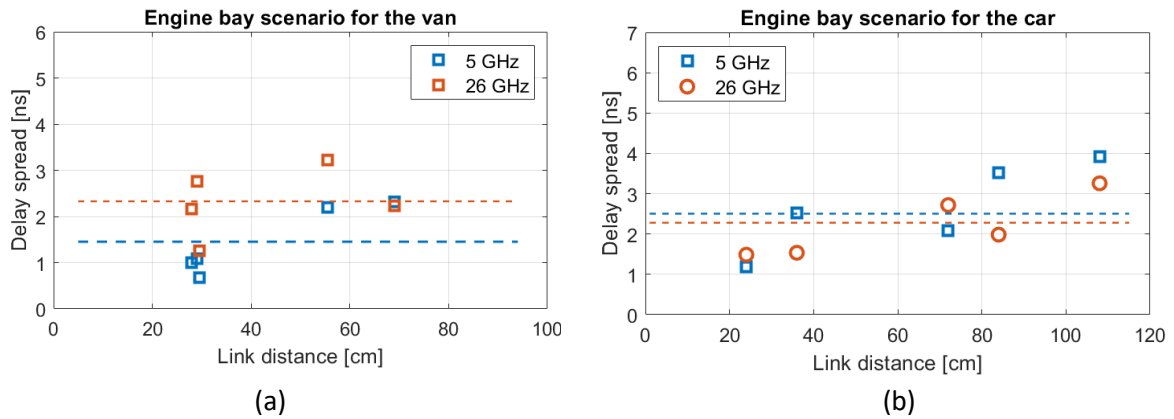
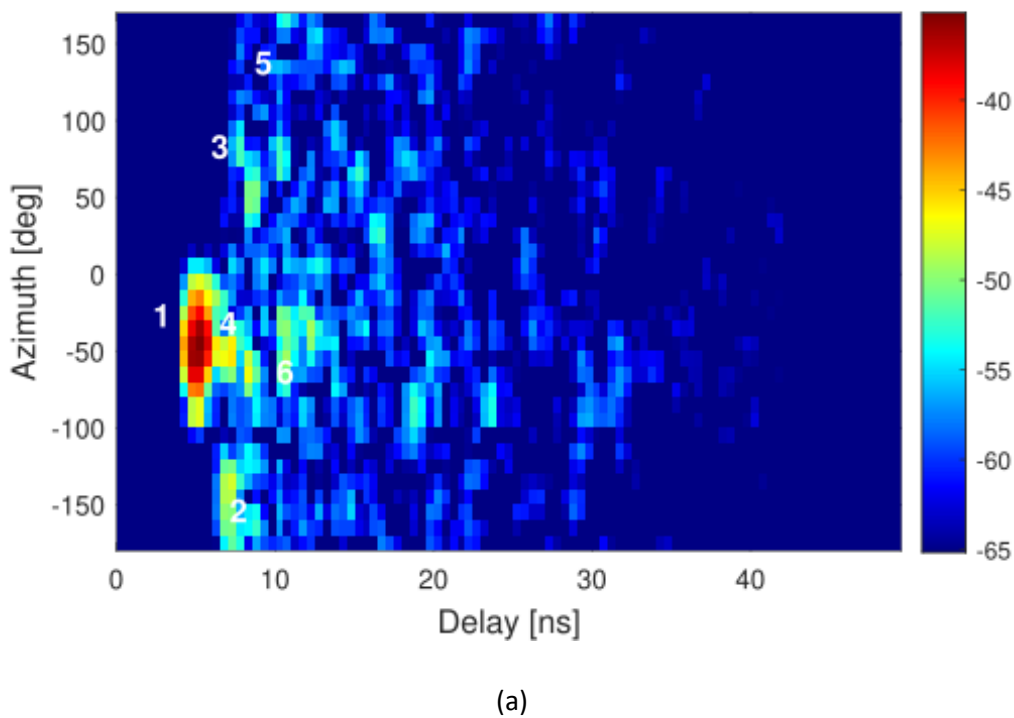
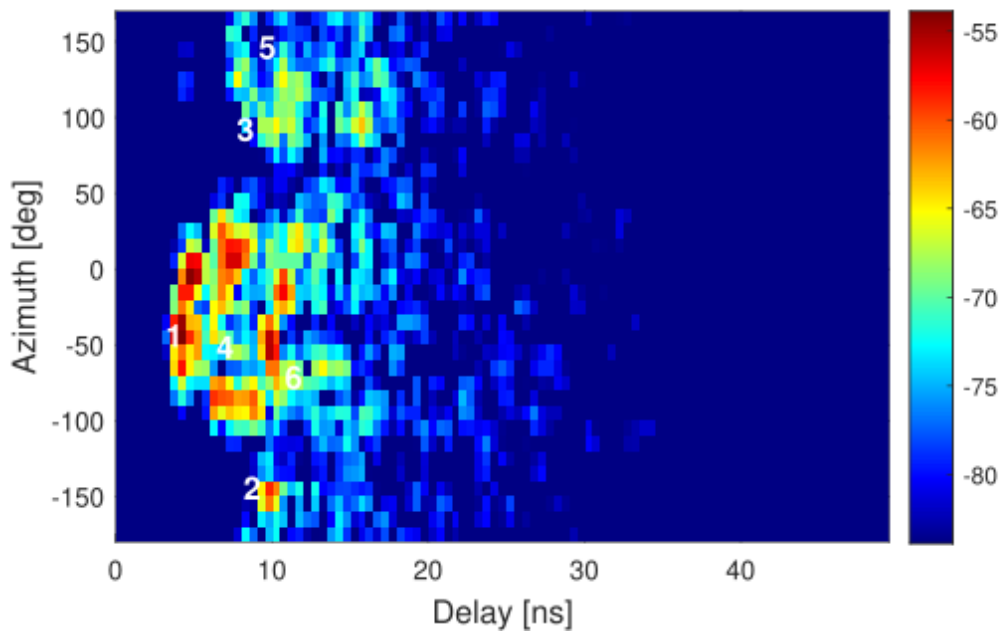


Figure 45. RMS delay spread results for measurements (a) in the van and (b) car, where the mean values are denoted by dashed lines.

The RMS delay spread results in the van are presented in Figure 45(a). It ranges from 0.67 to 2.19 ns for the lower frequency band and from 1.26 to 3.22 ns for the mmWave band. The average value of RMS delay spread for the mmWave band is 2.33 ns and is more than 50 % higher than the average value of RMS delay for the lower frequency band (i.e. 1.45 ns). The results for the RMS delay spread in the car are shown in Figure 45(b). In this case, it ranges from 1.2 to 3.91 ns with an average value of 2.5 ns for the lower frequency band. For the mmWave band, the range is from 1.49 to 3.26 ns with an average value of 2.26 ns. The similarity between these two frequency bands is due to the fact that the same major MPCs are detected based on their CIRs. Furthermore, the number of identified MPCs is similar in most cases. Owing to the longer distances between the Tx and the Rx, the maximum delay spreads for these two bands are larger than that obtained in the van.





(b)

Figure 46. Measured PADPs in Scenario 1 at (a) low frequency band and (b) mmWave band

Figure 46 illustrates the PADPs for two frequency bands measured in the Scenario 1 (inside the van, as presented in Figure 43(a)). The directional antenna used as the Rx antenna at the low-frequency band has approximately twice the HPBW of the antenna used at mmWave band, which results in a lower angular resolution. For both frequency bands, rich multipath environments are observed and the major MPCs are detected within a delay range of 40 ns. As illustrated in Figure 46, several dominant MPCs can be identified in both frequency bands. The LOS path has an angle of arrival (AOA) in the azimuth plane of -40° to -50° .

The trajectories of the identified MPCs, as indicated in Figure 47, are derived from the geometry information of the passenger cabin and the MPC parameters. Paths 2 and 3 are results of single bounce reflections from the side passenger doors and front wall of the passenger cabin, respectively. Path 4 is produced by scattering from the edges of the metal chair legs, resulting in notable variations in power levels relative to LOS path power in different frequency bands. Path 5 is a double bounce reflection path from the front wall and side door of the passenger cabin.

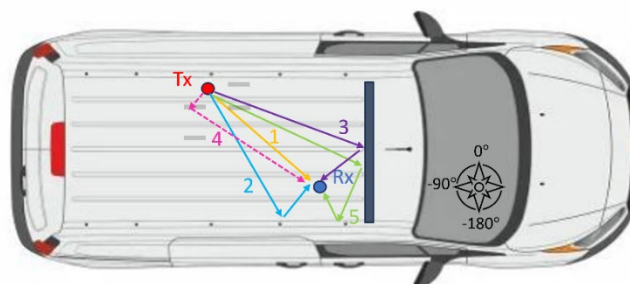
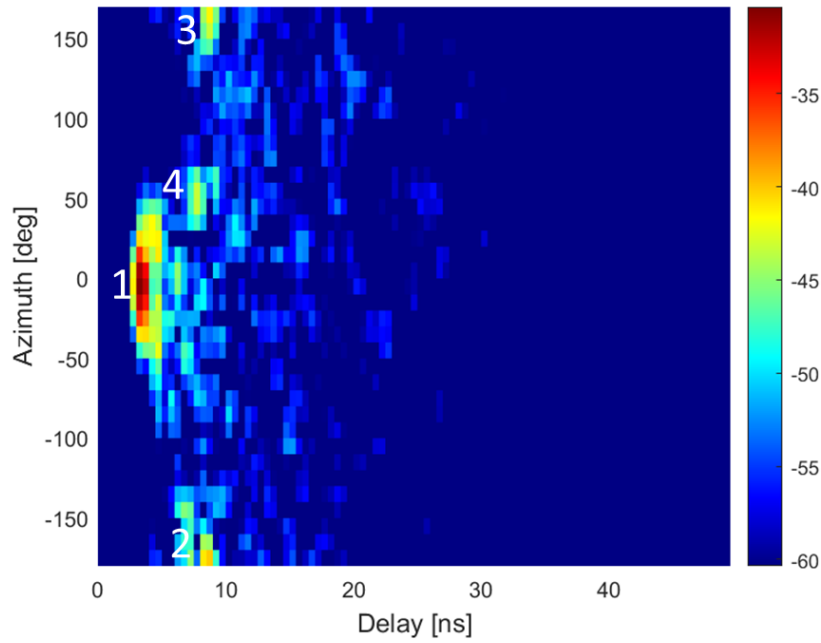
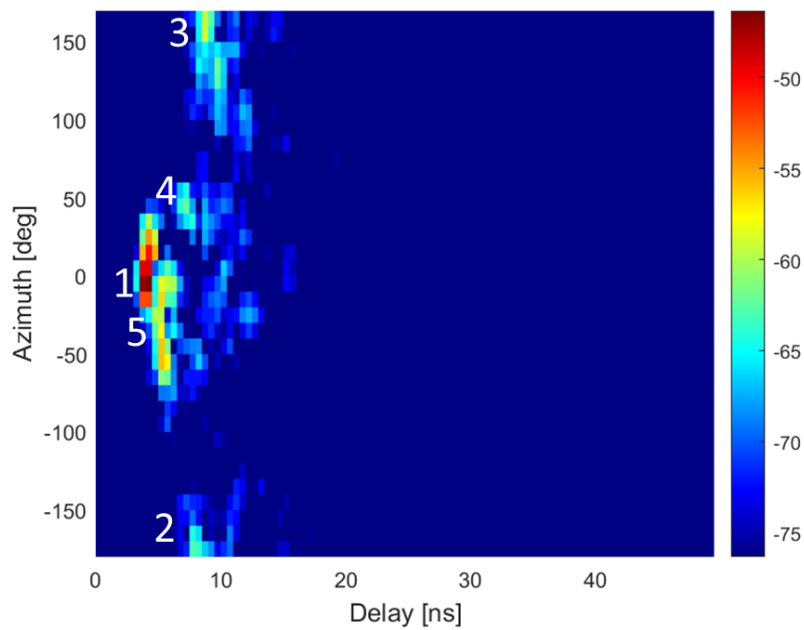


Figure 47. Trajectory of the main MPCs in relation to geometry of Scenario 1



(a)



(b)

Figure 48. Measured PADPs in Scenario 2 at (a) low frequency band and (b) mmWave band

Figure 48 presents the PADPs for two frequency bands measured in the Scenario 2 (inside the car, as presented in Figure 43 (b)). It can be observed that a LOS path and several weak MPCs could be detected in both bands. Path 1 is the LOS path. Paths 2 and 3 are the single reflections from the left passenger sides and windows. Path 4 is the reflection from the passenger back seats. For the mmWave band, one could distinguish path 5, which is a single bounce reflection path from the back sides of the front seats. Due to mounting considerations, the Rx antenna for the low frequency band is much higher than that of the mmWave band. Path 5 in the low frequency band is not as dominant as in the mmWave band.

4.1.1 Analysis of in-cabin LOS measurements in the car

This sub-section reports further LOS measurements performed inside the cabin of the Benz 200d car (see previous subsections). In this measurement setup, the transmitter antenna was positioned on the dashboard of the car. The wideband omnidirectional antennas were employed, featuring a gain ranging between 1 and 3 dB. As shown in Figure 49, the receiver antenna was placed in different locations depending on the scenario: on the side door for Scenario A, on the back seat for Scenario B, and on the front seat for Scenario C, shown in Figure 49 (c).

In the following, the channel characteristic in terms of path loss and RMS delay spread are analysed for the three different scenarios across various frequency ranges, 4-6.5 GHz, 25-27.5 GHz and 99-101.5 GHz, providing a comprehensive understanding of their behaviour under different conditions.

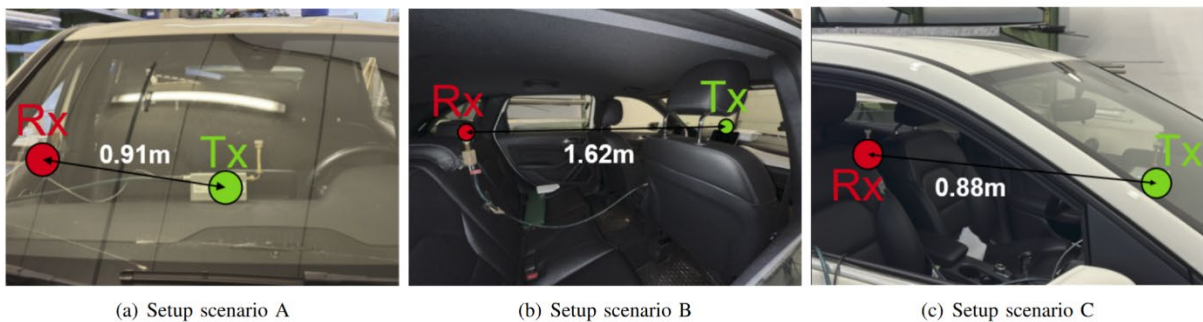


Figure 49. Images depicting various in-vehicle Line-of-Sight scenarios, with the following link distances: Scenario A – 0.91 m, Scenario B – 1.62 m, and Scenario C – 0.88 m

The Root mean square (RMS) delay spread is computed using the formula previously described in Section 3.3.2.

The calculation of PL involves a detailed analysis of the various propagation paths present within the Power Delay Profile. The PDP provides valuable insights into how signals arrive at a receiver over time, accounting for different multipath components caused by reflections, diffraction, and scattering in the environment.

To identify the significant propagation paths within the PDP, we employ a one-dimensional search technique that focuses on detecting local maxima. This method helps pinpoint the peaks in the PDP, which correspond to the primary paths that contribute to signal reception.

Once we have conducted this analysis, we assume that a total of N distinct paths has been identified. Considering a N distinct paths, the path loss value is calculated by summing all N MPCs. In this calculation, the effects of the transmitting and receiving antenna gains are explicitly removed. This is achieved by subtracting the antenna gains from the total received power, ensuring that the resulting path loss value is not influenced by the specific characteristics or performance of the antennas. As a result, the path loss measurement is antenna independent. The path loss value is given by:

$$PL(dB) = -10\log_{10}\left(\sum_{n=1}^N \frac{P_n}{G_{Tx}G_{Rx}}\right) \quad (4.1)$$

where the term P_n represents the power of the n -th path, G_{Tx} is the gain of the transmitting antenna and G_{Rx} is the gain of the receiving antenna.

Measured Path Loss can be compared with the reference Isotropic Free Space Path Loss (IFSPL), given by:

$$IFSPL = 20 \log_{10} \left(\frac{4\pi d f}{c} \right) \quad (4.2)$$

where d is the distance between Tx and Rx.

Table 14: Overview of RMS Delay Spread, Path Loss, and IFSPL Values for Various In-Vehicle LoS Scenarios (illustrated in Fig. 49) Across Different Frequency Ranges.

scenario	In-vehicle LoS scenario								
	4 - 6.5 GHz			25 - 27.5 GHz			99 - 101.5 GHz		
	τ_{rms} (ns)	PL (dB)	IFSPL (dB)	τ_{rms} (ns)	PL (dB)	IFSPL (dB)	τ_{rms} (ns)	PL (dB)	IFSPL (dB)
scenario A	2.51	42.52	46.03	3.3	55.76	60.01 dB	0.57	70	71.64
scenario B	9.74	43.66	51.04	2.54	61.31	65.01	1.76	76.03	76.65
scenario C	5.46	40.51	45.73	2.53	55.02	59.71 dB	0.8	69.12	71.35

Table 14 summarizes root mean square delay spread (DS), path loss (PL) and Isotropic Free Space Path Loss (IFSPL) values for the LoS scenarios A, B, C and for all the frequency bands.

Observing Table 14 it can be concluded that at 4-6.5 GHz, the PL is approximately 5 dB lower than the IFSPL across the three scenarios, with Scenario B showing the largest deviation at 7.38 dB. This band also exhibits the highest delay spread at 9.74 ns, indicating the presence of more MPCs with significant power in Scenario B compared to the others. Generally, DS values in this frequency range are larger than those in higher bands, attributed to reduced propagation and scattering losses. The enclosed nature of the vehicle, with windows closed and complex internal structures, amplifies MPC effects in the lower frequency range. Furthermore, regarding frequencies in the range of 25 to 27.5 GHz, it is observed that the PL is, on average, 4 dB lower than the corresponding IFSPL. Although the mmWave bands generally exhibit higher PL compared to lower frequency bands, most of the MPCs can still be detected, significantly influencing the observed channels. The DS values in the mmWave bands are consistently comparable or lower than those in the 4–6.5 GHz range, but significantly higher than those in the 99–101.5 GHz range. Overall, the channel characteristics in the mmWave bands resemble those of the lower frequency bands more than those of the sub-THz bands.

Finally, for frequency bands between 99 GHz and 101.5 GHz the calculated PL in this band is much closer to the IFSPL compared to the other two bands, with a maximum difference of 2.23 dB in scenario C. As mentioned earlier, the LoS path has significantly more power than the other MPCs, which means the scattering paths have less impact on the channels at sub-THz frequencies. Scenario B shows the largest DS among the three scenarios due to a greater link distance. However, its DS values are the smallest across the three frequency bands because of the extremely high propagation and scattering losses in sub-THz bands.

4.1.2 Summary

The main conclusions of the presented work in this sub-chapter are:

- Two vehicles were used in the measurements: a van and a car.
- Two groups of in-vehicle measurements were performed. The first group measurements were conducted in the engine bay and aimed to study the CIR and delay characteristics. The second group measurements were made in the passenger cabin, which aimed to study the PADP and angular spread.

- Below 7 GHz (lower frequency) and mmWave bands were measured. For both bands, the measured frequency bandwidth was 2.5 GHz with 625 frequency points, which resulted in a 0.4 ns delay resolution.
- During the measurement within the engine bays of both the van and the car, the Tx was fixed while the Rx was moved to 5 different locations. For both van and car cases, when the distance between the Tx and the Rx was comparatively short, the power of the LOS path was much larger compared to the other MPC due to the less scattering. Moreover, the depth of the engine bay of the van was larger than that of the car and the components within the engine were distributed with different heights, which resulted in a more complex and rich propagation scenario and CIRs with various shapes. The similarity of the RMS delay spread in the car between the two frequency bands was owing to that the same major MPCs were detected based on their CIRs.
- The measurements in the passenger cabin were conducted in a LOS scenario for both the van and the car. The PADPs were obtained, because the Rx was rotated. The trajectory of the main MPCs in relation to cabin geometry for Scenario 1 was given. For scenario 2, information and explanations about the possible scattering objects contributing to the significant MPCs in the derived PADP were included.
- The main radio channel characteristics such as Path Loss and Delay Spread have been analysed for the lower frequencies, mm-wave, and sub-THz bands for different in-cabin LoS configurations and ranges inside the car. It has been shown that generally the mm-wave and the lower bands have similar behaviour: most of the MPCs are still significant in the mm-wave band, despite the higher free-space losses. This can be attributed to the enclosed and complex propagation environment which generates a significant amount of scattering, due to the presence of many metal components in the vehicle. On the other hand, a higher degree of “channel sparsity” is observed in the sub-THz band, with propagation characteristics that approaching free-space propagation and DS values decreasing up to one order of magnitude compared to lower frequencies.

4.2 IN-VEHICLE MEASUREMENTS AND OUTDOOR-TO-VEHICLE MEASUREMENTS AT CNIT

In the present sub-section, the measurement campaign carried out at CNIT, and its main results are presented and discussed. Such measurements involve both in-vehicle and outdoor-to-indoor propagation with vehicles and are mainly focused on the new frequency bands envisioned for 6G-and-beyond systems, i.e. the mid-band FR3, and the sub-THz frequencies.

4.2.1 Measurement setup

The measurement setups utilized by CNIT for this project consist of two main configurations, each designed for specific frequency ranges: FR3 (8-12 GHz) and the sub-THz D-band (110-170 GHz).

For both setups, a Keysight PNA-X Network Analyzer N5242B (10 MHz – 26.5GHz) was employed to ensure precise measurements, a pair of standard horn antennas (transmitter Tx and receiver Rx) and a vehicle type. The vehicles considered in our measurement campaign are Tesla Model Y and Seat Leon. In order to perform down and up-conversion to extend the frequency range to the D-band the VNA was equipped with VDI Extenders WR6.5.

For FR3 measurements, horn A.R.R.A mx820 horn antennas with a gain of 15-16 dBi were used. For the D-band, we employed VDI conical horn antennas with a gain of 21-23 dBi.

In some measurement campaigns, a rotating positioner was also used, on which the receiving antenna was placed. Figure 50 and Figure 51 show the photos of the setups of the measurements at FR3 frequencies and at D-Band frequencies. Table 15 and Table 16 summarize the parameters and characteristics of the measurement setups for the different frequency ranges.



Figure 50. Pictures of the measurements campaign at sub-THz (D-Band).

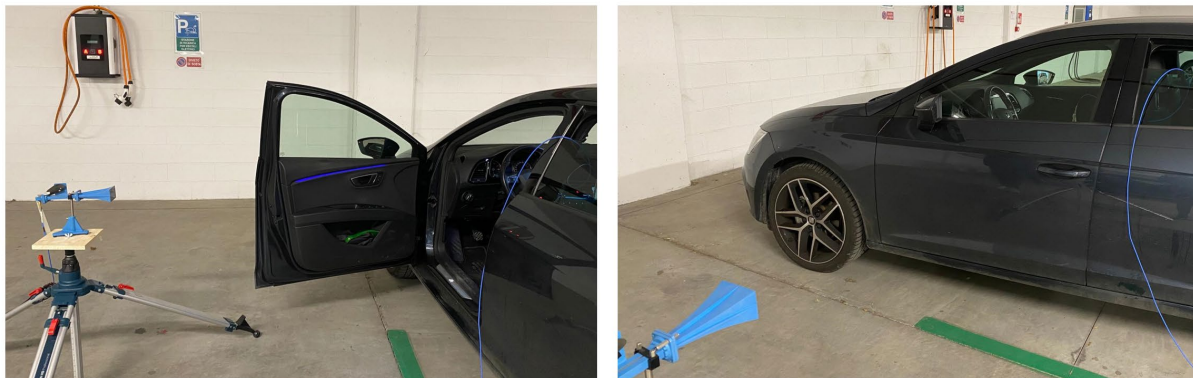


Figure 51. Pictures of the measurements campaign at FR3 (X-Band).

Table 15: Parameters and characteristics of the measurement setup at sub-THz (D-Band).

Sub-THz (D-Band) measurement setup	
VNA:	Keysight PNA-X Network Analyzer N5242B (10 MHz – 26.5GHz)
Extenders:	VNA'S VDI Extenders WR6.5
Calibration Kit:	VDI Type A/ Type B TRL Calibration Kit WR6.5CK
Antenna type:	VDI conical horn WR6.5
Antenna Gain (dBi):	21-23 dBi
Antenna Diameter:	10.8 mm
Start – Stop Frequencies:	110 - 170 GHz
Bandwidth:	60 GHz
Sample Points:	1601
Time domain resolution:	0.0167ns

Transmitted Power:	10 dBm
---------------------------	--------

Table 16: Parameters and characteristics of the measurement setup at FR3 (X-Band).

X-Band measurement setup	
VNA:	Keysight PNA-X Network Analyzer N5242B (10 MHz – 26.5GHz)
Calibration Kit:	Keysight 80533D 3.5 mm
Antenna type:	horn A.R.R.A mx820
Antenna Gain (dBi):	15-16 dBi
Start – Stop Frequencies:	8 - 12 GHz
Bandwidth:	4 GHz
Sample Points:	915
Time domain resolution:	0.25 ns
Transmitted Power:	dBm

4.2.2 In-vehicle scenarios

The following are the various indoor vehicular measurement setups conducted for both D-band and FR3 frequencies. The analysed scenarios include:

- **Seating Position Scenarios** where the Tx and Rx are positioned on the seats (driver's seat and rear seat on the driver's side), as shown in Figure 52:
 - Both antennas facing each other.
 - Antennas back to front.

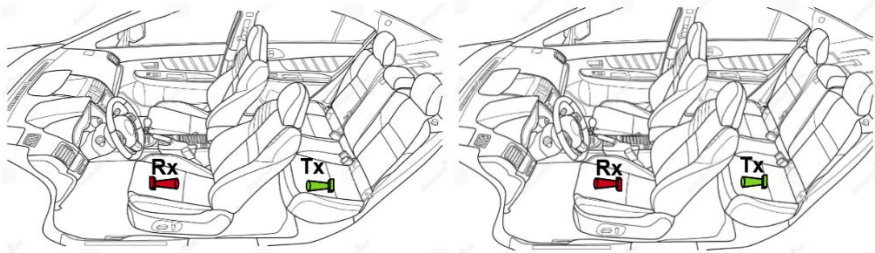


Figure 52: Seating position scenarios.

- **Floor Position Scenarios** where Tx and Rx are placed on the floor of the vehicle, one in front on the driver's side and the other behind, also on the driver's side, as shown in Figure 53:
 - Both antennas facing each other.
 - Antennas back to front.
 - Rx rotated 90° inward toward the interior of the vehicle.

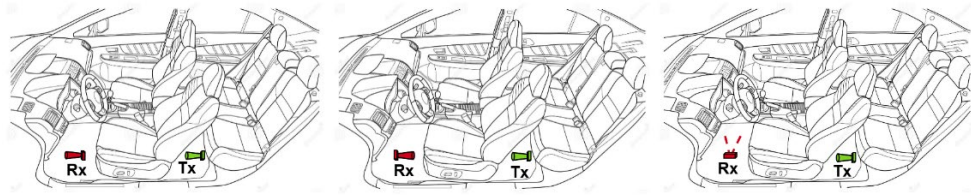


Figure 53. Floor position scenarios.

- **Combined Floor and Seat Scenarios:** where the Rx is placed on the floor on the driver’s side, while the Tx is positioned on the seat behind the driver, as shown in Figure 54:
 - Both antennas facing each other.
 - Antennas back to front.
 - Rx rotated 90° inward toward the interior of the vehicle.

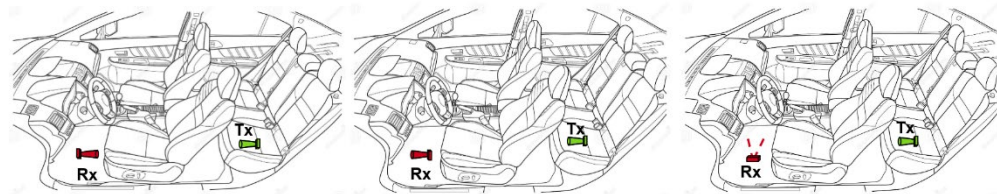


Figure 54. Combined floor and seat scenarios.

Table 17 reports the distance between Tx and Rx in the different in-vehicle scenarios.

Table 17: Link distances different scenarios and frequencies.

Link distances at different scenarios and frequencies	
Scenario Tx-Rx on the seats (8-12GHz)	1.4 m
Scenario Tx-Rx on the ground (8-12GHz)	1.15 m
Scenario Tx-Rx on the seats (110-170GHz)	0.55 m
Scenario Tx-Rx on the ground (110-170GHz)	0.45 m

At FR3 frequencies, another measurement setup has been established for analysing the power angle delay profile. In this configuration, the Tx is placed on the dashboard, while the Rx is mounted on a mechanical rotator located in the trunk, as shown in Figure 55 . The receiver rotates 360° in 5° increments.

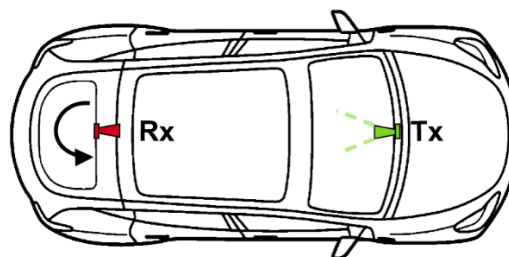


Figure 55. Measurement setup to analyse power angle delay profile.

4.2.3 Outdoor2vehicle scenarios

Further measurements were conducted to analyse key propagation parameters in outdoor-to-vehicle (O2V) scenarios, where the Tx is positioned outside the vehicle, and the Rx is located inside the vehicle. These measurements were performed at both sub-THz and FR3 frequency bands. The main measurement setups and configurations, shown in Figure 56, Figure 57 and Figure 58 are as follows:

- **Setup 1 O2V**→ The Tx is placed outside the vehicle next to the driver's side door, while the Rx is located inside the vehicle on the driver's seat. Two different configurations, illustrated in Figure 32, were considered, distinguished by the height of both the Tx and Rx:
 - *Configuration 1 setup 1*: The Tx and Rx were aligned to face each other, with the Tx at a height that illuminated the driver's side window.
 - *Configuration 2 setup 1*: The Tx and Rx were aligned face-to-face, but in this configuration, the Tx was positioned to illuminate the driver's door rather than the window.
- **Setup 2 O2V**→ The Tx is placed outside the vehicle, positioned directly in front of it, and illuminates the trunk. The Rx is located inside the trunk compartment. This configuration is used to assess the propagation characteristics between the external transmitter and the receiver within the enclosed trunk space.
- **Setup 3 O2V**→ The Tx is positioned outside the vehicle, in front of the hood, and illuminates the hood area. The Rx is placed inside the hood compartment. Two different configurations, shown in Figure 57, are examined in this configuration, where the Rx is placed at different heights inside the hood:
 - *Configuration 1 setup 3*: the Rx is positioned just beneath the hood.
 - *Configuration 2 setup 3*: the Rx is placed inside a specific compartment within the hood (present in the Tesla Model Y vehicle model), with the antenna positioned inside this enclosed space.

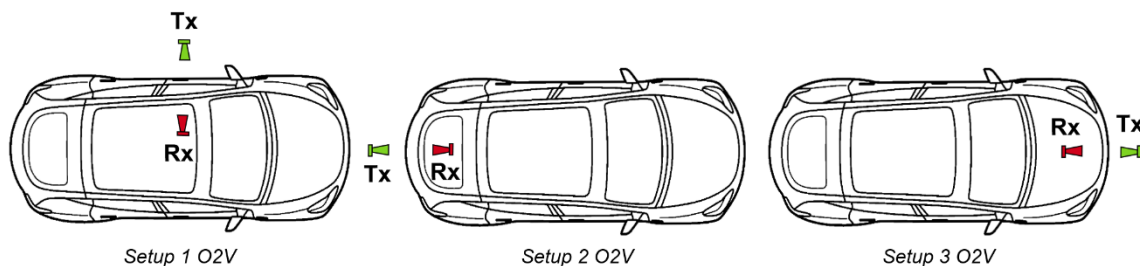


Figure 56. Different measurements setups outdoor2vehicle (O2V).

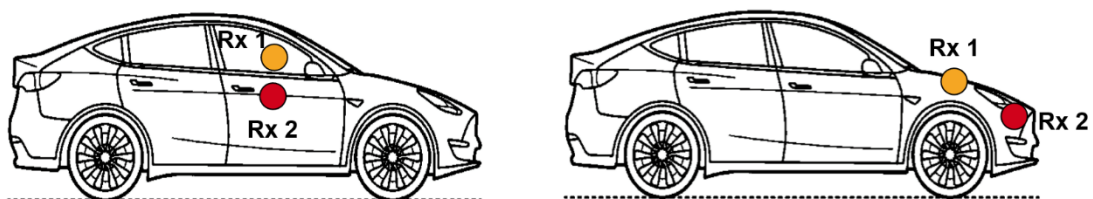


Figure 57. Different configurations for setup 1 and setup 3, where the receiver height varies.

To obtain the power angle delay profile analysis for the FR3 frequency band as part of the propagation study outputs, various O2V setups were established, as shown in Figure 58. In these setups, the receiver is mounted on a mechanical rotator inside the trunk of the vehicle, allowing it to rotate 360° in increments of 10°. Meanwhile, the Tx is positioned outside the vehicle at different locations, as shown in:

- **Setup A O2V**→Tx positioned in front of the hood, illuminating the hood area.
- **Setup B O2V**→Tx positioned in front of the trunk, illuminating the trunk compartment.
- **Setup C O2V**→Tx positioned at the side of the vehicle, near the passenger door, behind the driver.

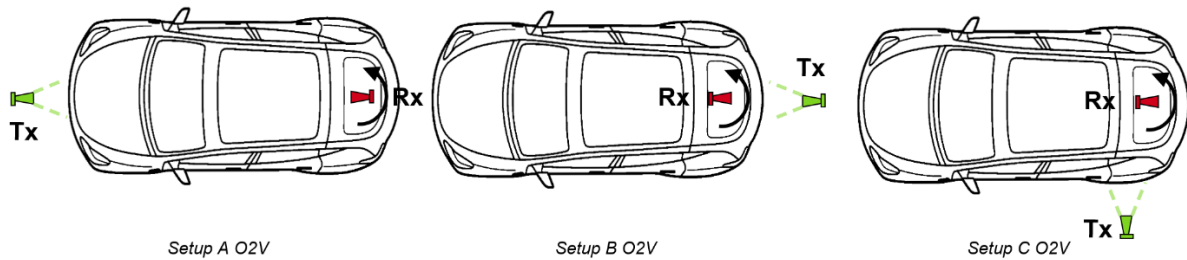


Figure 58. Different setups O2V with Rx mounted on a mechanical rotator.

This arrangement enables comprehensive measurements of the signal characteristics as the receiver captures data across a full rotation, thus providing insights into how the signal power and delays vary with different angles relative to the transmitter. By analysing these profiles, we can better understand the propagation environment and the effects of multipath propagation on signal quality.

4.2.4 Measurement post-processing and relevant propagation parameters

The main parameters derived from the measurement analysis that are useful for studying the characterization of propagation in vehicular scenarios are:

- Power delay profile (PDP).
- Root mean square (RMS) delay spread (DS).
- Path loss (PL).
- Isotropic free space path loss (IFSPL).
- Penetration loss (L).
- Power angle delay profile (PADP).

4.2.4.1 Power Delay Profile and Associated Propagation Parameters

The VNA measures the complex parameter S_{21} , which is used to derive the channel frequency response (CFR) $H(f)$. The entire measured frequency band can be preliminarily divided into smaller sub-bands before extracting the multipath components in the time domain. This approach offers several advantages, especially when analysing the channel characteristics across different frequency ranges. Once the frequency band is divided into sub-bands, the time-domain representation of the multipath components can be obtained for each sub-band individually. This method allows for more accurate modelling and characterization of the channel.

For the measurements conducted in the D-band, given the very large bandwidth of 60 GHz, a subdivision into smaller sub-bands was implemented. Specifically, for each sub-band, a bandwidth of 6 GHz was considered.

On the other hand, for the measurements at FR3 frequencies, the number of sub-bands is approximately 2 to 3, with each sub-band having a bandwidth of around 1.5 to 2 GHz.

To obtain the channel impulse response (CIR), the CFR is first filtered with a Hamming window before transitioning to the time domain using the IFFT. The Hamming window is applied to reduce aliasing and discontinuities, as the channel frequency response $H(f)$ is not periodic. By smoothing the edges of the CFR, the Hamming window $W(f)$ helps to minimize abrupt changes, which can lead to artifacts in the time-domain representation. The CIR, then, is given by:

$$h(\tau) = \mathcal{F}^{-1}[W(f) \cdot H(f)] \quad (4.3)$$

Therefore, the PDP is expressed by:

$$P(\tau) = |h(\tau)|^2 \quad (4.4)$$

To analyse the dispersion of multipath components (MPCs) in the time domain, we evaluated the Root Mean Square Delay Spread across different frequencies and scenarios.

The calculation of the delay spread is based on the time delays of the MPCs in the PDP relative to the main component. It is, in fact, calculated using the formula previously described in Section 3.3.2 and only the components that exceed the noise threshold are considered.

Another parameter obtained from the various measurement campaigns at different frequencies and for each sub-band is the isotropic free space path loss, calculated using the formula in the Section 4.1.1.

4.2.4.2 Penetration Loss Analysis

An analysis of signal attenuation in vehicular scenarios was conducted at both sub-THz at D-Band and FR3 frequencies, considering both outdoor-to-vehicle and in-vehicle configurations. Transmission losses due to various vehicle components were evaluated across different frequency ranges.

Penetration loss measurements for certain vehicle components were carried out on two different vehicles (i.e. Tesla Model Y and Seat Leon) to assess whether the materials used in different cars exhibit significant differences in signal attenuation.

In the O2V scenario, penetration loss values were obtained for specific vehicle components, including the window, door, hood (in the case of the Tesla Model Y), and trunk.

In the in-vehicle scenario, transmission loss was studied through the seatback and the area beneath the seat, which is not completely open but contains materials like plastic and metal.

To evaluate the attenuation of the various components, the Tx and Rx antennas are aligned horizontally, and the obstructing obstacle is placed between them. Regarding the calculation of penetration loss, we used two different methods. These methods were then compared to ensure greater reliability of the results.

The first method is based on time gating, which isolates the main path peak in the CIR using an appropriate time window. This is done both in the calibration measurement for the line-of-sight (LoS) scenario and in the obstructed line-of-sight (OLoS) measurement, where an obstacle is present between the antennas. The corresponding power values are obtained from the isolated peaks, and then the difference in dB units is calculated between the power from the calibration measurement and the power from the OLoS measurement.

The second method that involves averaging the differences between the CFR values from the calibration measurement for LoS and OLoS measurements, for each frequency range of interest.

4.3 MODELING OF PROPAGATION IN IN-VEHICLE AND OUTDOOR2VEHICLE SCENARIOS AT FR3 AND D-BAND FREQUENCIES

In the following, we further investigate in-vehicle propagation in other frequency bands not analysed in the previous sections, and in particular the mid-band FR3 and the higher sub-THz frequencies (D-band, from 110 to 170 GHz). Furthermore, with reference to the above-mentioned bands we also study the behaviour of outdoor-to-indoor propagation with vehicles, which is important to establish the feasibility of inter-vehicle communications or communication between subnetworks located in different vehicles.

4.3.1 In-vehicle Results

This section reports the analysis of parameters related to the study of channel propagation in an in-vehicle OLoS environment. The results cover penetration loss analysis due to obstructing objects inside the vehicle, as well as evaluations of parameters associated with the PDP, such as path loss and RMS delay spread. Additionally, an analysis of the PADP is provided.

4.3.1.1 Path loss and RMS delay spread results for in-vehicle scenario, at FR3 and sub-THz frequencies

The results of the path loss and RMS Delay Spread analysis at frequencies FR3 and D-Band pertain to the in-vehicle OLoS scenarios, which are depicted in Figure 59. The distance between Tx and Rx are reported in Table 17.

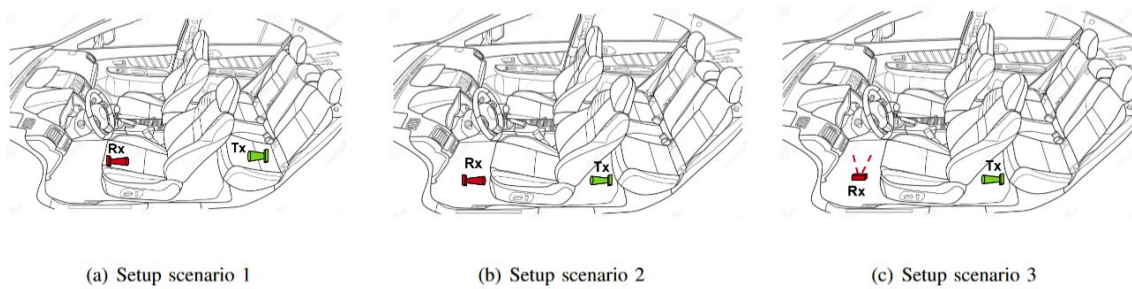


Figure 59. Pictures of the various OLoS scenarios: Scenario 1, Scenario 2, and Scenario 3.

Table 18: RMS Delay Spread, Path loss and Isotropic Free-Space Path Loss for the In-vehicle OLoS scenarios shown in Fig. 59.

In-vehicle OLoS scenario D-Band frequencies									
sub-Band	scenario 1			scenario 2			scenario 3		
	τ_{rms} (ns)	PL (dB)	IFSPL (dB)	τ_{rms} (ns)	PL (dB)	IFSPL (dB)	τ_{rms} (ns)	PL (dB)	IFSPL (dB)
110 – 116 GHz	0.45	83.99	67.48	0.39	74.29	66.57	5.67	107.48	-
116 – 122 GHz	0.42	84.20	67.93	0.28	75.51	67.02	3.30	106.93	-
122 – 128 GHz	0.34	84.34	68.36	0.35	74.59	67.44	4.17	109.96	-
128 – 134 GHz	0.42	86.69	68.77	0.27	74.74	67.85	3.41	109.30	-
134 – 140 GHz	0.34	85.18	69.16	0.45	76.84	68.24	4.17	110.09	-
140 – 146 GHz	0.51	85.42	69.53	0.46	76.05	68.61	4.43	108.89	-
146 – 152 GHz	0.71	87.49	69.88	0.77	75.45	68.97	5.55	111.07	-
152 – 158 GHz	0.55	85.51	70.23	0.71	74.81	69.31	3.93	111.18	-
158 – 164 GHz	0.73	87.43	70.55	0.71	75.31	69.64	6.03	111.35	-
164 – 170 GHz	0.90	89.12	70.87	0.99	76.09	69.96	8.18	111.89	-

In-vehicle OLoS scenario X-Band frequencies									
sub-Band	scenario 1			scenario 2			scenario 3		
	τ_{rms} (ns)	PL (dB)	IFSPL (dB)	τ_{rms} (ns)	PL (dB)	IFSPL (dB)	τ_{rms} (ns)	PL (dB)	IFSPL (dB)
8 – 10 GHz	0.55	49.9	54.55	1.14	52.5	52.35	7.6	72.17	-
10 – 12 GHz	0.4	50.01	56.19	1.09	54.9	54.1	6.8	75.51	-

The results are summarized in *Table 18* in terms of RMS DS, and measured PL, for different sub-bands in the measured frequency bands. For Scenarios 1 and 2, the values of isotropic free space path loss are also reported as a reference. Looking at the table we can conclude that at 8-12GHz in Scenario 1, the gap between PL and IFSPL is of a few dBs, while in Scenario 2, this difference is nearly negligible. Consequently, the attenuation from the vehicle's interior furnishings has a limited effect on communication within the FR3 band. In Scenario 3, however, both PL and DS values are much higher compared to the first two scenarios. This increase is likely due to the receiver being oriented towards the passenger side.

At D-Band frequencies, instead, we conclude that, PL values for all three OLoS scenarios are significantly higher than the corresponding IFSPL values due to obstructed line-of-sight conditions. In scenario 2, lower PL values result from the clutter under the seat partially blocking the line of sight less than the seat backrest. However, these values still exceed the IFSPL, indicating that even minor obstructions can notably reduce signal intensity.

Scenario 3 shows further increases in PL as the directional antenna is rotated 90 degrees towards the passenger side. This also leads to a significant rise in DS compared to Scenarios 1 and 2, primarily due to greater attenuation of the line-of-sight path. Despite this, communication is still viable through reflections off the car's sidewalls and furnishings, as the PDP reveals multiple multipath components above the noise threshold. Additionally, *Table 18* indicates a slight increase in delay spread with frequency across all OLoS scenarios in the D-Band, suggesting that penetration losses for the direct path diminish more rapidly than those from reflected paths in the surrounding environment.

4.3.1.2 Penetration loss results in-vehicle OLOS SCENARIO

In this section we report the study evaluated transmission loss across various in-vehicle obstructed line-of-sight scenarios, focusing on two specific obstructions: the seat backrest, within two vehicle models (Tesla Model Y and the Seat Leon) and the area under the seat within Tesla Model Y, where plastic components partially block the LoS path.

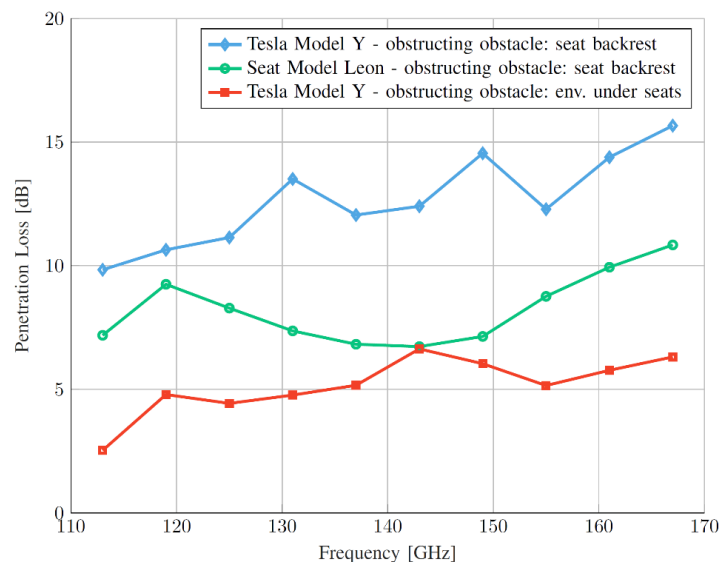


Figure 60. Penetration loss values at D-Band frequencies for obstructing obstacles, including the seat backrest of the Tesla Model Y, the seat backrest of the Seat Leon, and the area beneath the seats of the Tesla Model Y.

Figure 60 shows the graph of the penetration loss values as a function of frequency across the 110–170 GHz range, representing signal attenuation due to both the obstruction from the seat backrest and

environmental factors beneath the seat. In this case, the penetration loss values were calculated for each of the sub-bands into which the entire bandwidth was divided.

The red line represents signal attenuation when the line of sight is blocked by the area under the seat in the Tesla Model Y. Notably, in the D-Band frequency range, this under-seat obstruction leads to a non-negligible attenuation, with values near 2 dB at 113 GHz, and increasing to approximately 6.3 dB at 167 GHz.

The blue and green lines illustrate penetration loss values when the line of sight between antennas is blocked by the seat backrest, for the two measured vehicles. These results highlight that the Tesla Model Y's seat backrest causes higher attenuation than that of the Seat Leon. Specifically, the Seat Leon's penetration loss ranges from 7.18 dB at 113 GHz to 10.84 dB at 167 GHz, while the Tesla Model Y shows losses from 9.83 dB to 15.66 dB. A summary of the average penetration loss and its standard deviation over the whole D-Band, for different obstructions and vehicles is presented in Table 19.

Table 19: Mean penetration Loss and standard deviation values in in-vehicle scenario at sub-THz.

Obstruction Obstacles	Mean Penetration Loss [dB]	σ [dB]
Seat backrest Tesla Model Y	12.65	1.86
Seat backrest Seat Leon	8.23	1.42
Environment under the seat	5.16	1.17

Observing the results in Table 19, it is evident that the penetration values for the Tesla Model Y seat backrest are higher compared to the Seat Leon backrest. This is most likely due to the thickness of the backrest, which appears to be thicker, and also the materials used. The two seat backrests show higher transmission losses compared to the area under the seat, as even though there are plastic or other materials under the seat, these are likely less obstructive than the backrest.

The analysis of penetration loss within the frequency range of 8 to 12 GHz reveals that the obstructions created by the seat backrest, as well as the area under the seats, have minimal impact. The results indicate that the penetration loss due to these factors is negligible, measuring approximately between 0 and 1 dB.

4.3.1.3 Power angle delay profile in in-vehicle scenario

This section delves into the analysis of the power angle delay profile within a vehicular environment, focusing on the effects of antenna positioning and obstructions on signal propagation. The vehicle considered for the spatial analysis is the Tesla Model Y.

In this analysis of the power angle delay profile, at 8-12 GHz, within a vehicular environment, we examined a specific scenario where the Rx is located inside the trunk, mounted on a mechanical rotator. The Tx, on the other hand, is positioned on the dashboard and directed towards the trunk, as shown in Figure 61. In this configuration, the receiving antenna is situated at the height of the headrest of the front seat. When the Rx faces the Tx, they achieve a nearly unobstructed line of sight.

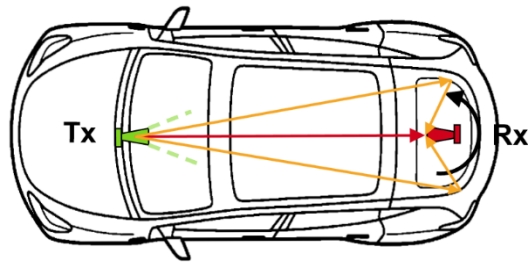


Figure 61. In-vehicle scenario evaluated for PADP result.

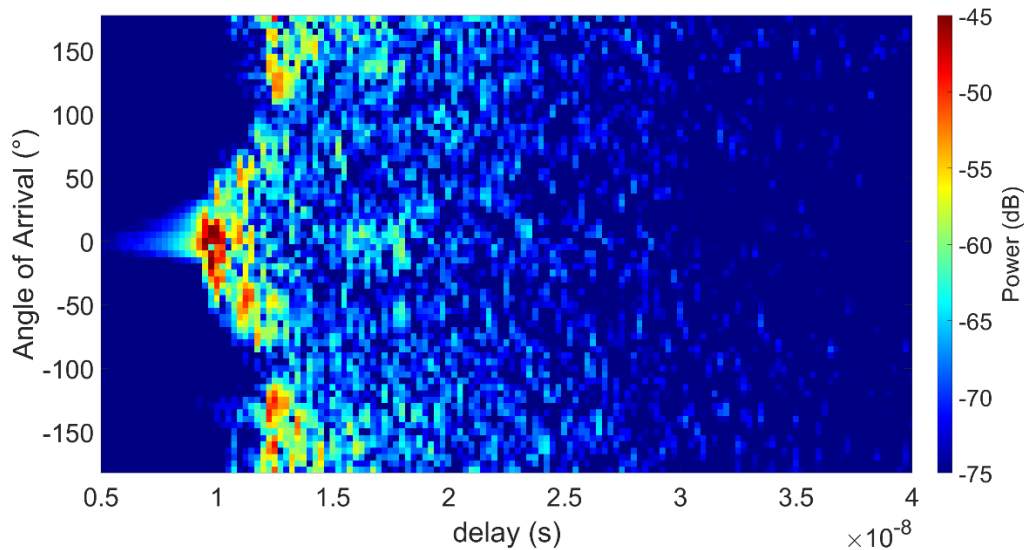


Figure 62. PADP result for in-vehicle scenario.

Firstly, the graph of the Power Angle Delay profile (PADP), shown in Figure 62, indicates that, in this specific scenario, the paths from the Tx to the Rx exhibit symmetry due to reflections and multipath components within the vehicle. From the graph presented in Figure 62, we can conclude that at approximately 0°, when Tx and Rx are aligned, the maximum power intensity is recorded at -45 dBm. This power peak is attributed to the direct path, occurring at about 3 m, as shown in Figure 61, which corresponds to the distance between Tx and Rx. The power level remains around -50 dBm until the receiver is rotated to approximately 40° and -40°. However, when the receiver is positioned at angles of approximately 90° to 100° and -90° to -100°, a significant drop in power is observed. Additionally, there are other observable power peaks with a value of approximately -50 dBm when the receiver is rotated approximately 120° and -120° for symmetry in the analysed scenario. These peaks may result from reflections of the signal transmitted from Tx, which bounce off one side of the metal trunk and are then redirected to the receiver, thus traveling a longer distance, as shown in orange in the Figure 61.

4.3.2 Outdoor2vehicle scenario results

4.3.2.1 Transmission loss results in O2V scenario

This section shows the results of the analysis of signal attenuation in an outdoor-to-indoor vehicular scenario, focusing on how various components of a vehicle, such as the door, trunk, window, and how, impact signal strength at both the FR3 (8-12 GHz) and sub-THz (D-Band) frequency bands.

To achieve more realistic and comprehensive results, two different vehicles were examined in relation to transmission losses associated with these components. This analysis aims to provide insights into the effects of vehicle architecture on signal propagation and attenuation in practical applications.

In Figure 63 and in *Figure 64*, the curves representing the values of penetration loss as a function of frequency are presented across the FR3 and D-band. The penetration loss values were calculated for each sub-band considered within the examined frequency range. For instance, in the FR3 band, the bandwidth was divided into three sub-bands, each with a sub-band size of 1.3 GHz, while in the sub-THz range, the bandwidth was divided into ten sub-bands, each with a size of 6 GHz, due to its wider spectrum.

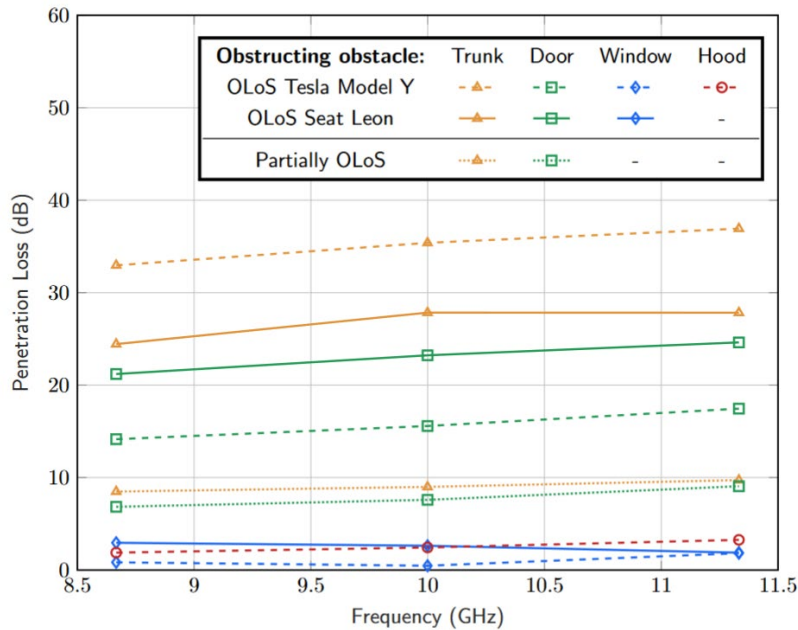


Figure 63. Penetration loss values for O2V scenario at FR3 frequencies.

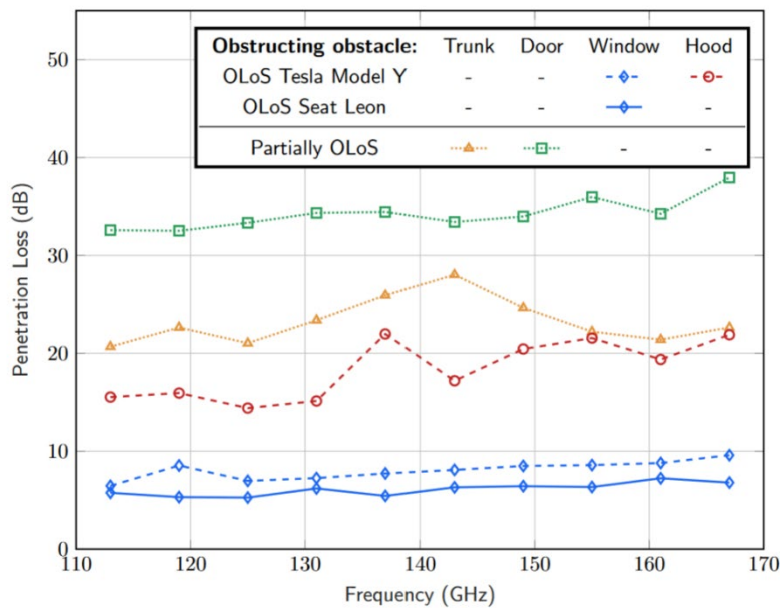


Figure 64. Penetration loss values for O2V scenario at D-Band frequencies.

4.3.2.2 Transmission loss results in o2v scenario at FR3 frequencies

In the graph shown in Figure 63, the dashed curves represent the penetration loss values in a scenario where the line of sight between the Rx and Tx is completely obstructed by an obstacle for the Tesla Model Y, while the solid curves correspond to the Seat Leon. The densely dotted curves illustrate the transmission loss values when the line of sight between Tx and Rx is not entirely obstructed but only partially, specifically when, for example, the car door and trunk are partially closed. These curves pertain to both vehicles, as they were derived by averaging the penetration loss values for each vehicle across all relevant sub-bands.

For both vehicles and across all vehicular components, the penetration loss behaviour is observed to be relatively stable.

Furthermore, the component exhibiting the lowest attenuation for both vehicles is the window, which is attributed to its relatively small thickness.

Interestingly, it is worth noting that the Tesla's hood shows transmission loss values at these frequencies comparable to those of the window. This can be attributed to the fact that the hood is significantly thinner compared to other components like the trunk or the doors.

Regarding door attenuation, it can be inferred that the door of the Seat Leon exhibits greater attenuation than that of the Tesla. Despite the relatively similar thickness of the doors between the two vehicles, this difference is likely attributed to variations in material composition. Conversely, the higher attenuation observed in the Tesla's trunk is probably due to differences in both material and thickness.

Table 20 summarizes the average penetration loss values across the entire frequency band for all vehicle components and for both cases of partial obstruction in the frequency range from 8 to 12 GHz.

For the partially OLoS scenario, both vehicles are considered. The penetration loss results for the two vehicles are averaged to obtain the outcome.

Table 20: Mean penetration Loss and standard deviation values in O2V scenario at FR3 frequencies.

Obstruction Obstacles:	Mean Penetration Loss [dB]	σ [dB]
OLoS - Window Tesla Model Y	1.04	0.70
OLoS - Window Seat Leon	2.48	0.55
OLoS - Hood Tesla Model Y	2.53	0.69
OLoS – Door Tesla Model Y	15.72	1.66
OLoS – Door Seat Leon	23.01	1.72
OLoS – Trunk Tesla Model Y	35.09	2
OLoS – Trunk Seat Leon	26.7	1.96
Partially OLoS Door	7.82	1.13
Partially OLoS Trunk	9.06	0.62

4.3.2.3 Signal Spillover Effect through Window Transmission at FR3 frequencies

For attenuation measurements in the FR3 band, the antenna's reduced directivity results in a much wider footprint radius. This broader spread of the transmitted signal power can disperse over a larger surface area, potentially affecting multiple vehicle elements beyond the specific target of the attenuation study. This phenomenon is particularly significant in transmission loss analysis involving the vehicle door, where signal spillover may occur through the window.

To better understand signal behaviour in relation to vehicle geometry, the peak signal distances were recorded under both free-space and obstructed conditions for each of the three sub-bands within the FR3 band. This approach enables a comparative analysis of signal propagation and attenuation across different obstruction scenarios, highlighting the impact of vehicle components on signal behaviour in each frequency sub-band.

Specifically, for both the Tesla Model Y and the Seat Leon, a distance difference of approximately 3 cm is observed between the signal peak in free-space conditions and with the door closed. This discrepancy is attributed to the additional path taken by the signal as it passes through the vehicle window. As illustrated in the figure, the setup geometry shows both the direct signal path through the door towards the receiver in a radial direction and the spillover signal reaching the receiver.

It can thus be concluded that, in the FR3 band signal attenuation analysis with the vehicle door closed, a certain percentage of the total power reaching the receiver arrives via spillover through the window. This effect occurs with a geometry where the transmitter is positioned approximately 2 m from the door and at a height of about 1 m from the ground, as shown in Figure 65.

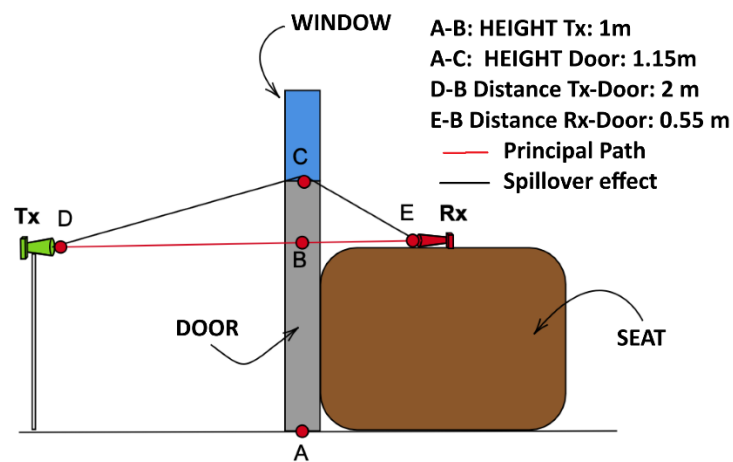


Figure 65. Geometry of the O2V scenario for evaluating penetration loss caused by the vehicle door.

4.3.2.4 Transmission loss results in O2V scenario at D-band frequencies

In the graph shown in Figure 64, the dashed curves represent the penetration loss values in a scenario where the line of sight between the Rx and Tx is completely obstructed by an obstacle for the Tesla Model Y, while the solid curves correspond to the Seat Leon.

Given that the attenuation values in the D band are significantly higher, it was not feasible to conduct an analysis of the attenuation measurements for vehicle components such as the door and trunk when they were completely obstructed, as the power of the main peak did not exceed the noise threshold. Consequently, the focus shifted to analysing scenarios in which the door and trunk were only partially closed. In the case of partial obstruction, the penetration loss values obtained from the different vehicles were averaged for each sub-band.

The graph clearly indicates that the attenuation values are significantly higher in the sub-THz range compared to the FR3 band.

Table 21 summarizes the average penetration loss values across the entire frequency band for all vehicle components and for both cases of partial obstruction in the frequency range from 110 to 170 GHz.

Table 21: Mean penetration Loss and standard deviation values in O2V scenario at D-Band frequencies.

Obstruction Obstacles:	Mean Penetration Loss [dB]	σ [dB]
OLoS - Window Tesla Model Y	8.04	0.95
OLoS - Window Seat Leon	6.10	0.66
OLoS - Hood Tesla Model Y	18.34	3.03
OLoS – Door Tesla Model Y	>= 50	-
OLoS – Door Seat Leon	>= 50	-
OLoS – Trunk Tesla Model Y	>= 50	-
OLoS – Trunk Seat Leon	>= 50	-
Partially OLoS Door	34.38	1.63
Partially OLoS Trunk	23.26	2.33

4.3.2.5 Power angle delay profile in O2V scenario

In the following section, results from the analysis of the PADPs for three specific O2V scenarios will be presented. In all three scenarios, the receiver Rx is mounted on a mechanical rotator within the trunk, while the Tx is positioned in distinct locations: in the first scenario, the Tx is placed directly in front of the trunk; in the second scenario, it is positioned in front of the vehicle’s hood; and in the third scenario, on the rear side of the vehicle, near the trunk. In each configuration, when the rotator is set to 0°, the receiver and transmitter are directly facing each other, and the receiver then rotates counterclockwise from this initial position.

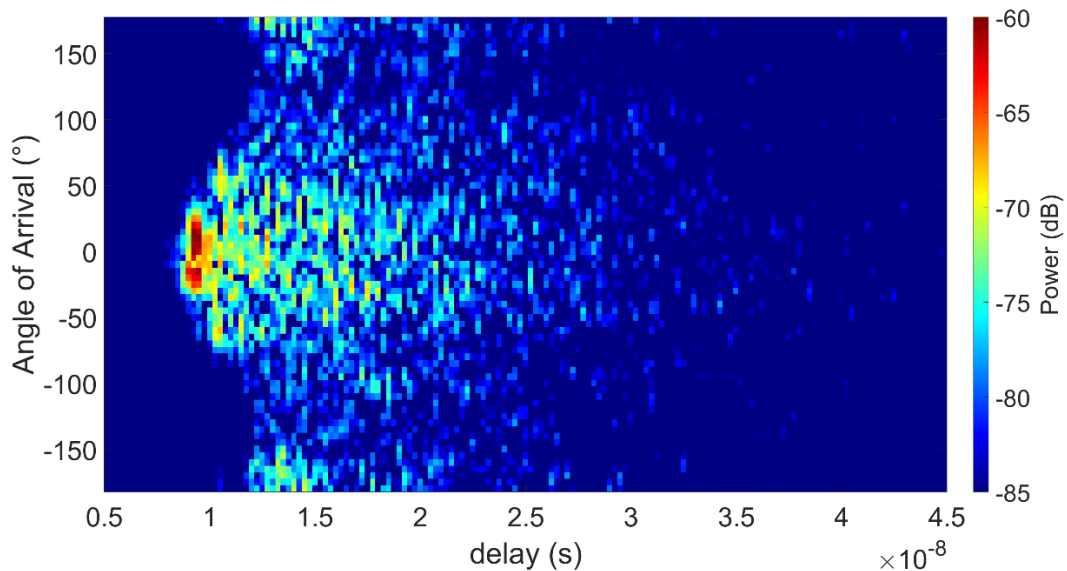


Figure 66. PADP for the O2V scenario with the Tx positioned externally in front of the trunk.

The PADP, shown in Figure 66, for the scenario in which the transmitting antenna is located externally in front of the vehicle's trunk has been analysed. This PADP illustrates that the received signal intensity is maximized when the receiving antenna is aligned with the transmitting antenna, specifically at angles of 0° achieving a peak value of -60 dBm. As the receiving antenna is rotated counterclockwise, the signal power gradually decreases, reaching a minimum of around 130°.

it is important to note that we are operating in an OLoS scenario, where the vehicle's trunk obstructs the line of sight between the Tx and the Rx. This setup explains why the received power peak is

significant only along the main path around 0° and on a few secondary paths within an angular range of approximately ±20°. When the receiver’s angle surpasses the 20-30° threshold, there is a noticeable drop in received power due to the increased obstruction caused by the trunk.

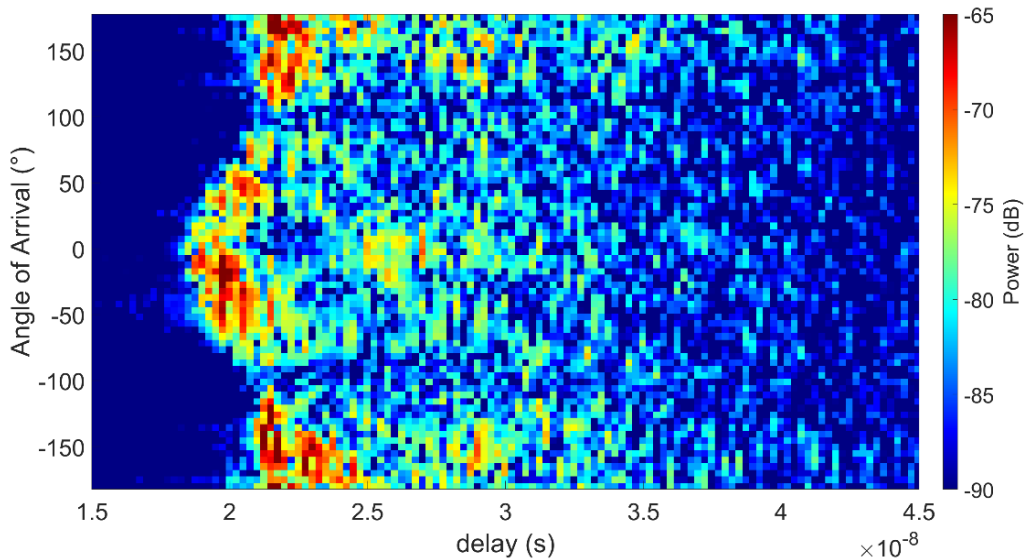


Figure 67. PADP for the O2V scenario with the Tx positioned externally in front of the hood.

Figure 67 reports the PADP result related to the scenario in which the Tx is located externally in front of the hood.

It is evident that this scenario mirrors, albeit with differing received power levels, the in-vehicle scenario, given the similar placement of the transmitter and receiver. The key difference, of course, is that in this case, the transmitter is located outside the vehicle, as opposed to on the dashboard. As a result, the signal must pass through the vehicle’s front windshield.

In this case as well, the results reveal a symmetry attributed to the vehicle's geometry, which remains identical on both the left and right sides.

In fact, from the PADP, shown in Figure 67, we can conclude that the received signal intensity is maximized when the antennas are positioned front to front, specifically at angles of 0°. As the receiving antenna is rotated counterclockwise, the intensity decreases until it reaches a minimum around 100 and -100°, where the receiving antenna is perpendicular to the direction of the transmitter. Subsequently, the signal intensity increases again, maintaining a significant power level at 180° and -180°. This increase is likely due to a reflection occurring when the signal bounces off a metallic part of the trunk, returning towards the receiver, as shown in Figure 68.

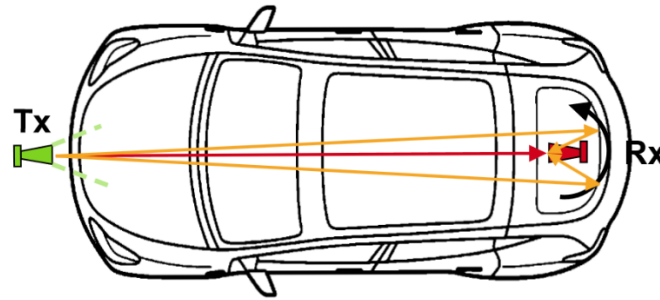


Figure 68. Main power paths detected in the PADP for the specific O2V scenario.

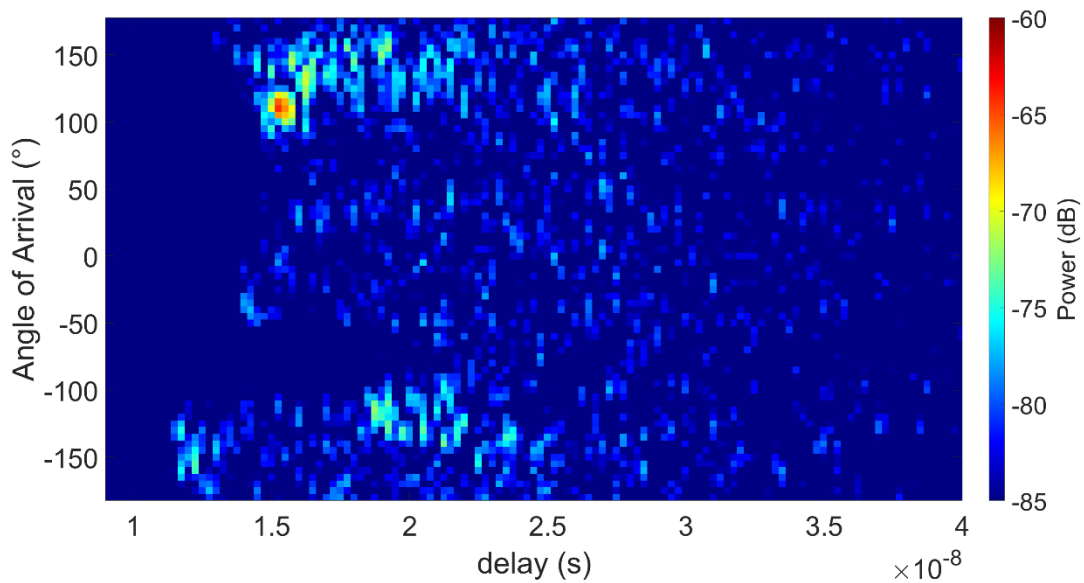


Figure 69. PADP for the O2V scenario with the Tx positioned externally on the rear side of the vehicle.

Finally, regarding the scenario in which the Tx is positioned laterally to the vehicle, the PADP shown in the Figure 69 provides a clear result: the received signal strength is minimal in the initial rotation angle (0 degrees), when the two antenna main radiation lobes are perpendicular. This 90° misalignment between the transmitting and receiving antennas reduces the efficiency of signal transfer, resulting in a weaker received signal. Furthermore, it is observed it the maximum power reaching the receiver occurs when it is oriented directly towards the Tx (the red spot happening in Figure 69 at about 100°). Another spot is clearly visible at about -120°, corresponding to a single-bounce specular reflection on the farthest sidewall of the vehicle. At all other receiving angles, the power never exceeds -75 dBm.

5 PROPAGATION MODELLING IN SHORT-RANGE OUTDOOR CAMPUS SCENARIOS

RF propagation modelling is essential for understanding how radio waves travel in short-range outdoor Device-to-Device (D2D) communication scenarios, particularly across frequency ranges FR1 (410 MHz - 7.125 GHz), FR2 (24.25 GHz - 52.6 GHz), and FR3 (7 GHz – 24 GHz). Each frequency range presents unique characteristics: FR1 offers good penetration and coverage, making it suitable for urban environments; FR2 provides high capacity and data rates, ideal for bandwidth-intensive applications; and FR3, while promising ultra-high capacity, faces challenges due to increased path loss. Effective modelling involves analysing large-scale channel parameters (LSPs) including path loss, PDP, RMS delay spread, K-factor, etc., for developing accurate channel models for various environments and conducting measurement campaigns to gather empirical data. This comprehensive approach ensures that wireless technologies can achieve optimal performance and connectivity in diverse and challenging outdoor settings.

The short-range measurement campaign for the outdoor campus scenario is briefly summarized in Table 22 below.

Table 22: Summary of measurement campaigns for the outdoor campus scenarios

Measurement information and parameters	Outdoor
Measurement location	Aalborg University (AAU) campus courtyard
Radio frequency [GHz]	2.5-4.5 (FR1)
	10 – 12 (FR3)
	28 – 30 (FR2)
Number of freq. points	2001
Tx & Rx antenna	Bi-conical (omni)
Number of links	13
Dimensions [m]	
Link distances [m]	1.6 m – 16.2 m

5.1 MULTI-BAND MEASUREMENTS IN A CAMPUS SCENARIO

In this section, we will present the delay spread, K-factor, and pathloss -analysis for Aalborg university outdoor courtyard measurement campaign. For all large-scale parameters, the measurements are first presented in a scatter plot laid on top of the figurative picture of the courtyard. Blue pentagram indicates a Tx -location and coloured triangles indicate Rx -locations. The colour depth of the Rx triangles indicates the magnitude of the measure on a colour scale provided in plots.



Figure 70. Picture of the Rx Tx locations and the courtyard site in Aalborg University

Figure 70 presents the measurement site and Rx – Tx locations. For this campaign, a total of 102 links were measured, including both LOS and NLOS links. However, the analysis in this section is based on only 13 radio links in the proximity of the Rx, i.e., Tx positions 20, 21, 22, 23, 42, 43, 44, 45, 46, 57, 65, 66 and 67 as shown in the Figure 70.

The distances between Rx – Tx locations were calculated by first calculating the delays of the strongest delay taps in LOS paths – and by trigonometric estimation for the NLOS paths. Figure 71 presents a figurative picture of the measurement site with Rx – Tx distances calculated for the LOS paths.

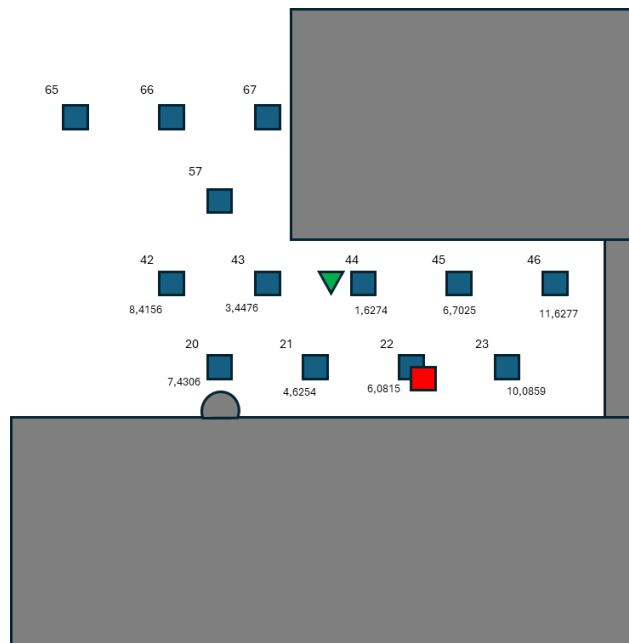


Figure 71. Figurative picture of the measurement site with calculated Rx (green pentagram) and Tx (blue square) LOS distances.

5.2 DELAY SPREAD ANALYSIS

Measured and estimated rms delay spreads are illustrated for the three measured frequency ranges FR1, FR3, and FR2 in layout plots Figure 72- Figure 74, respectively. The Tx location is denoted by a blue pentagram and Rx locations with coloured triangles. The colour indicates the rms delay spread in nanoseconds. As expected, we can observe that the delay spread increases with increasing link distance and correlates with the LOS/NLOS condition, at least on the lower frequencies. Estimated delay spreads are collected to empirical CDF and subsequent curves are illustrated in Figure 75 for the three frequency ranges. CDF curves are plotted separately for the LOS and NLOS links. Moreover, corresponding delay spread CDF curves from the 3GPP Urban Micro (UMi) reference model [25] are drawn for comparison. Numerical mean and standard deviation values for FR1, FR3, and FR2 are collected to summary *Table 23 - Table 25*, respectively.

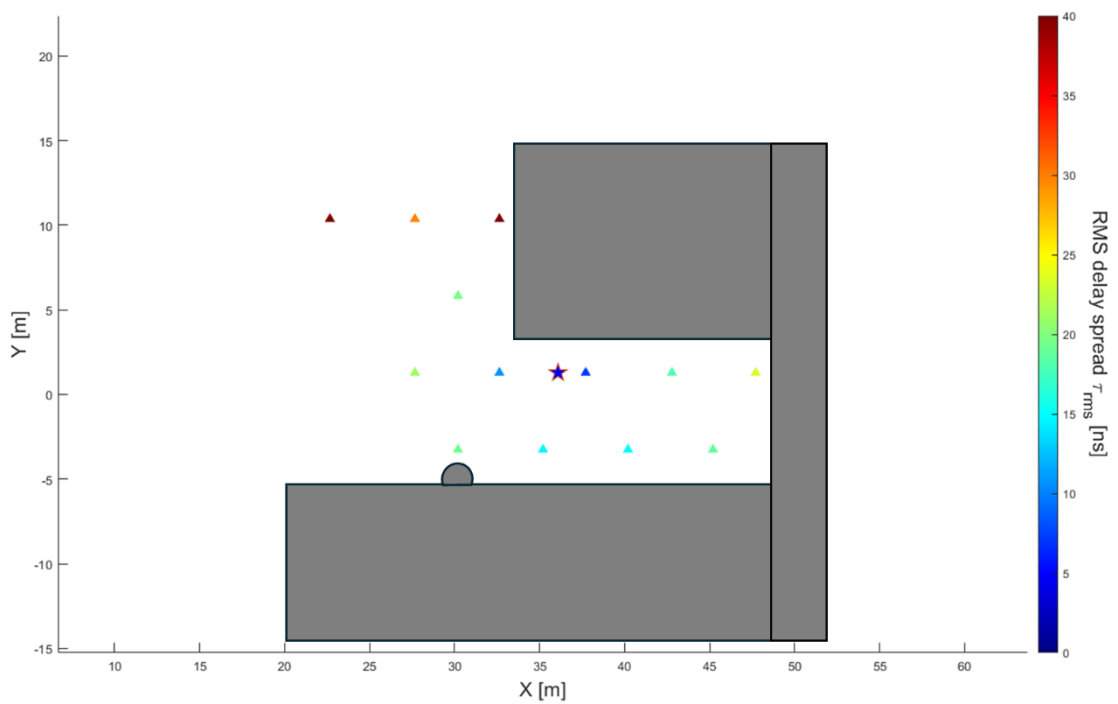


Figure 72. FR1 channel delay spread.

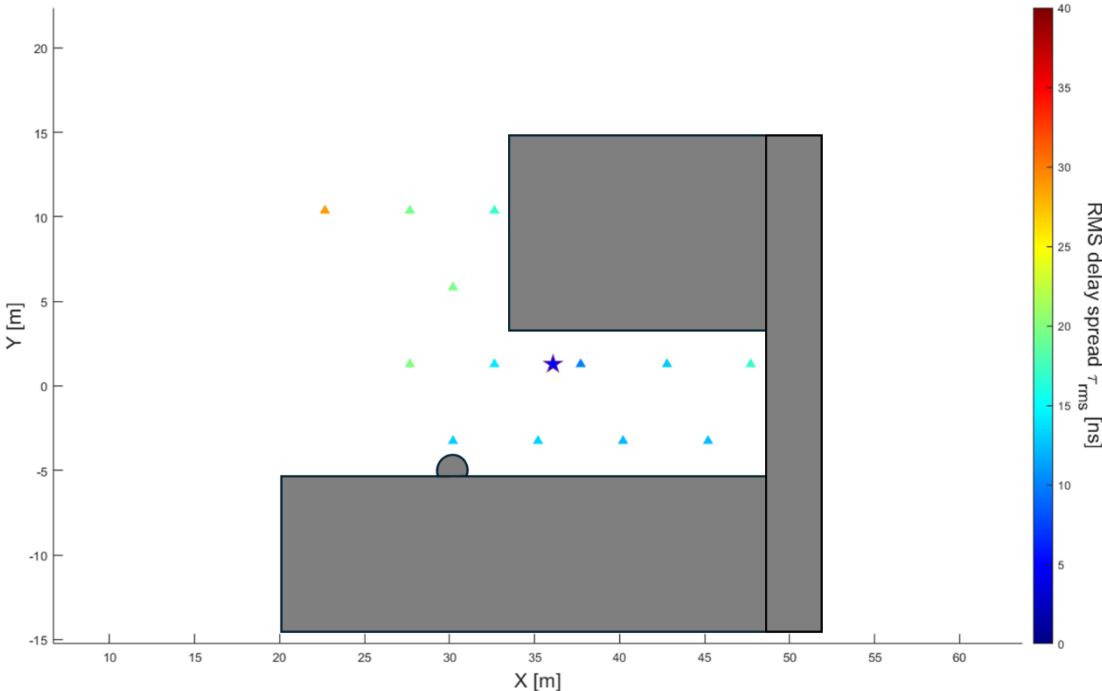


Figure 73. FR3 channel delay spread.

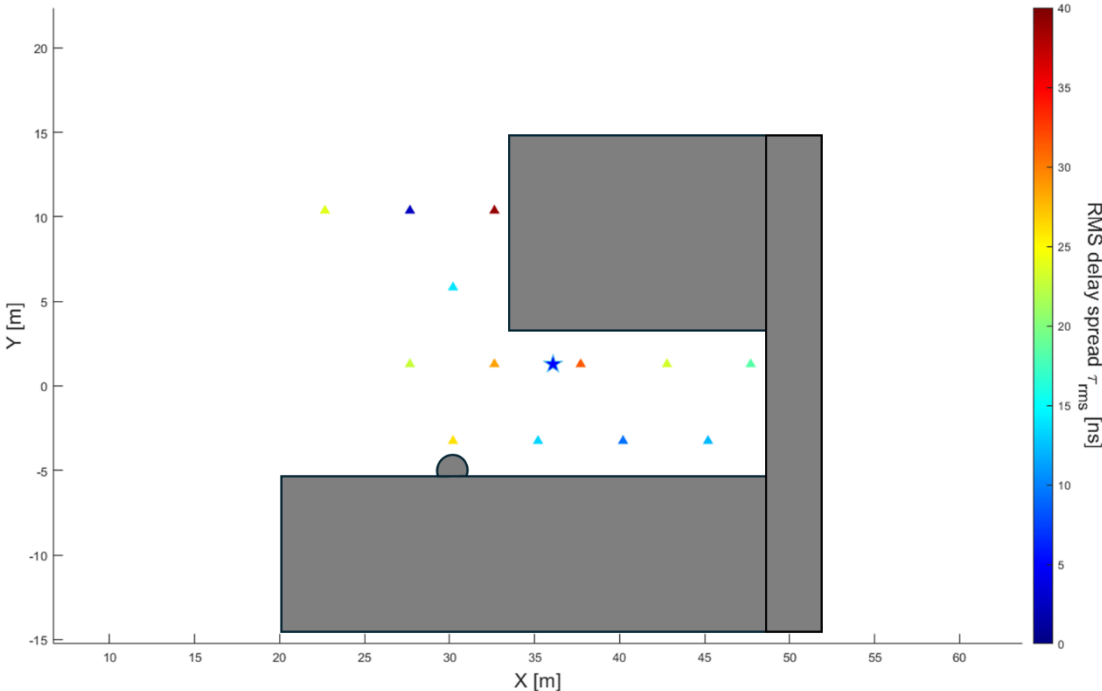


Figure 74. FR2 channel delay spreads

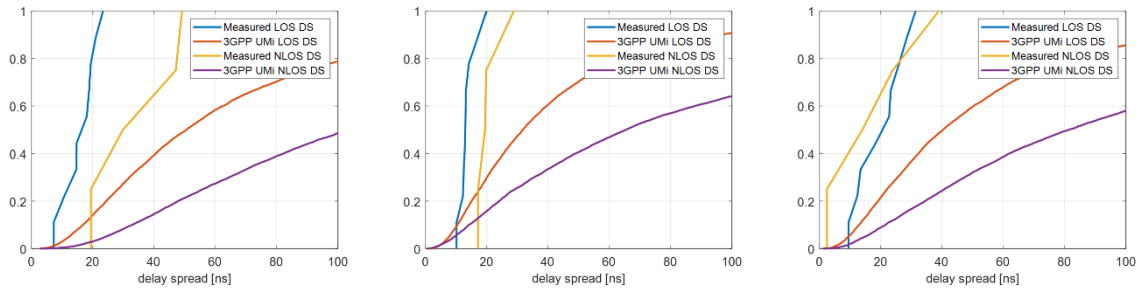


Figure 75. Delay spread CDF FR1 (left), FR3 (middle) and FR2 (right).

The CDF curves in Figure 75 illustrates that the 3GPP UMi street canyon model does not align well with the measured delay spreads. With only 13 short-range radio links causes the delay spread CDF to lag the 3GPP-UMi reference model by several tens of nanoseconds. For the measured CDFs, we see that NLOS paths show higher delay spread than LOS paths in the lower frequencies FR1 and FR2 but for the higher frequencies this is not the case. Due to insufficient measurement data to satisfy the statistical requirement, it is difficult to align measurements and 3GPP model. Furthermore, the 3GPP Umi street canyon doesn't restrict the evaluation for short-range communication links. The aim of this analysis is to understand if 3GPP models can be reliably used for short-range communication use cases or new updates are required in them. However, our analysis for these short-range outdoor communication scenarios is inconclusive to address this specific aspect, primarily due to insufficient amount of measurement data for statistical analysis. On the other hand, these measurements could be effectively used for calibrating raytracing simulations so that synthetic data can be generated for channel modelling purposes. This exactly highlights the importance of calibrated raytracing simulations, which could serve a suitable alternative for acquiring data for deterministic propagation channel modelling.

5.3 K-FACTOR ANALYSIS

Measured and estimated Rician K-factor values are illustrated for the three measured frequency ranges FR1, FR3, and FR2 in layout plots *Figure 76-Figure 78*, respectively. There are separate sub-figures for each of the three Tx locations. The Tx location is denoted by a blue pentagram and Rx locations with coloured triangles. The colour indicates the K-factor in decibels.

Generally, the closer LOS Tx locations show higher K-factor values, although some closer LOS Tx positions show higher K-factor than some further LOS Tx positions. This may be due to the scattering environment as these locations are often close to building walls or some other irregular shapes in walls. We can observe that in the higher frequencies, the K-factors of the LOS paths are higher in decibels.

Estimated delay spreads are collected to empirical CDFs and subsequent curves are illustrated in *Figure 79* for the three frequency ranges. Even though the K-factor was estimated for each link, the CDF curves are plotted only for the NLOS links. Moreover, corresponding K-factor CDF curves from the 3GPP Urban Street Canyon model (UMi) [25] are drawn for comparison. When inspecting the CDF curves, we can observe that measured K-factor values are significantly smaller than those of the 3GPP model. At the median density, the generated 3GPP curve shows more than 5 dB higher K-factor values than the measured data. The difference is the biggest in the lowest frequency range FR1. Overall, the measured K-factor values are more tightly packed closer to the 0 dB range than the reference model, clearly stating that the Rician characteristic of the fading is less evident in this measurement campaign than the 3GPP standard channel model would expect. A typical condition for Rician fading channel is a single dominant path and several weaker ones. A possible explanation for the lower-than-expected K-factor in measured

data is the presence of several strong reflected paths from surrounding building walls and their shapes. Numerical mean and standard deviation values for FR1, FR3, and FR2 are collected to summary *Table 23*, *Table 24* and *Table 25*, respectively.

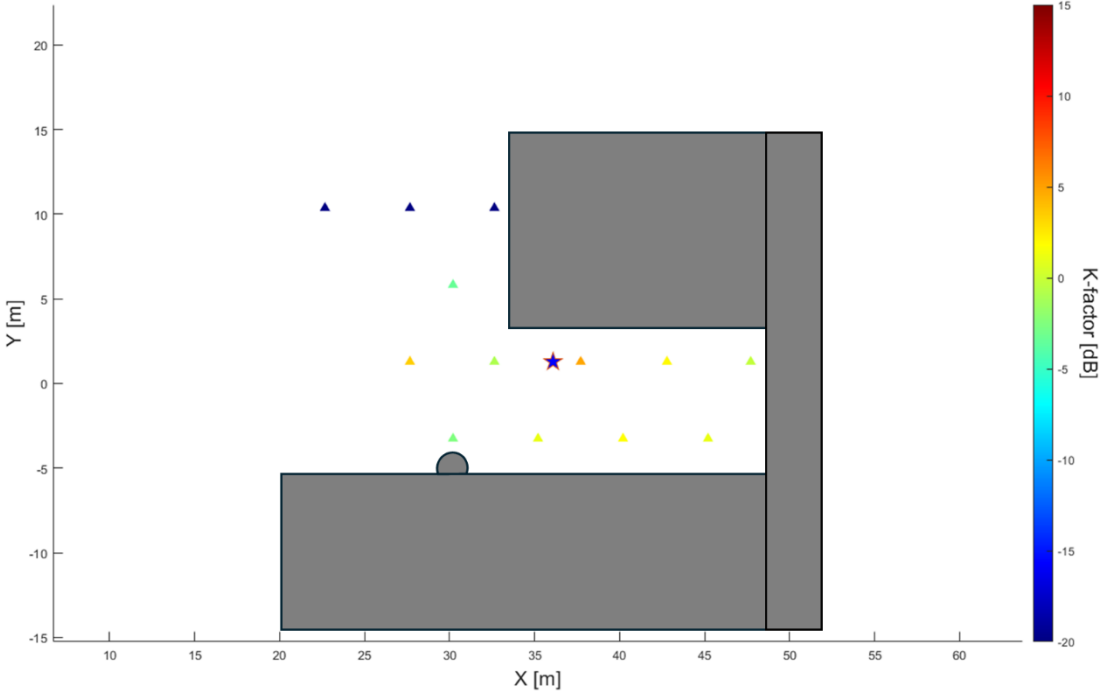


Figure 76. FR1 channel K-factors

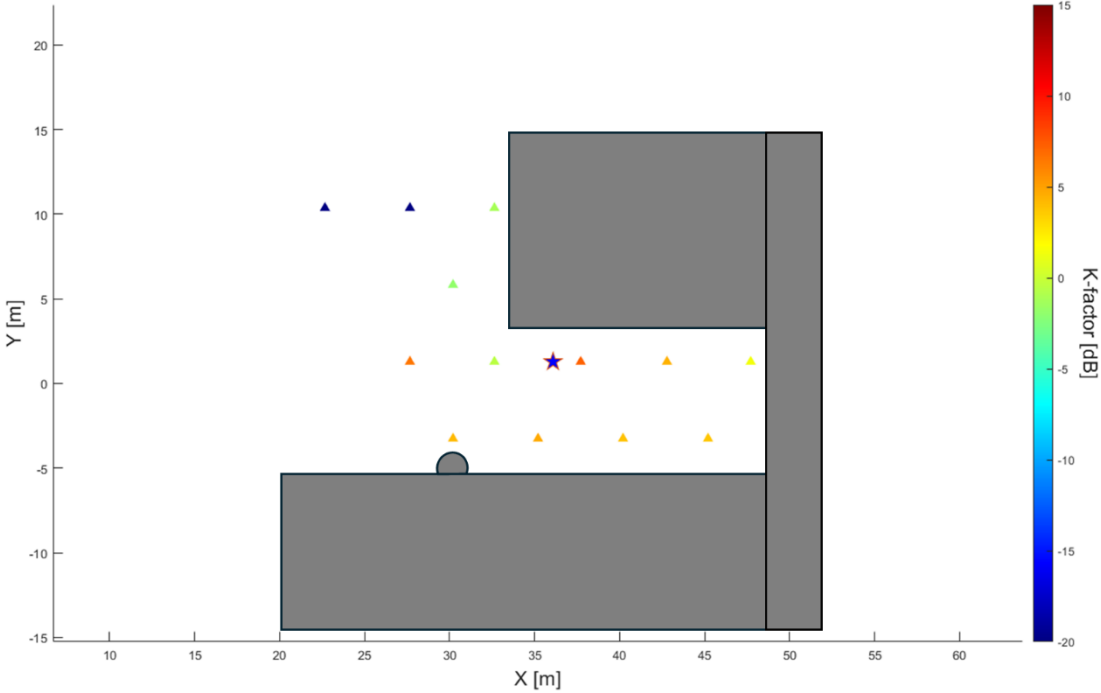


Figure 77. FR3 channel K-factors

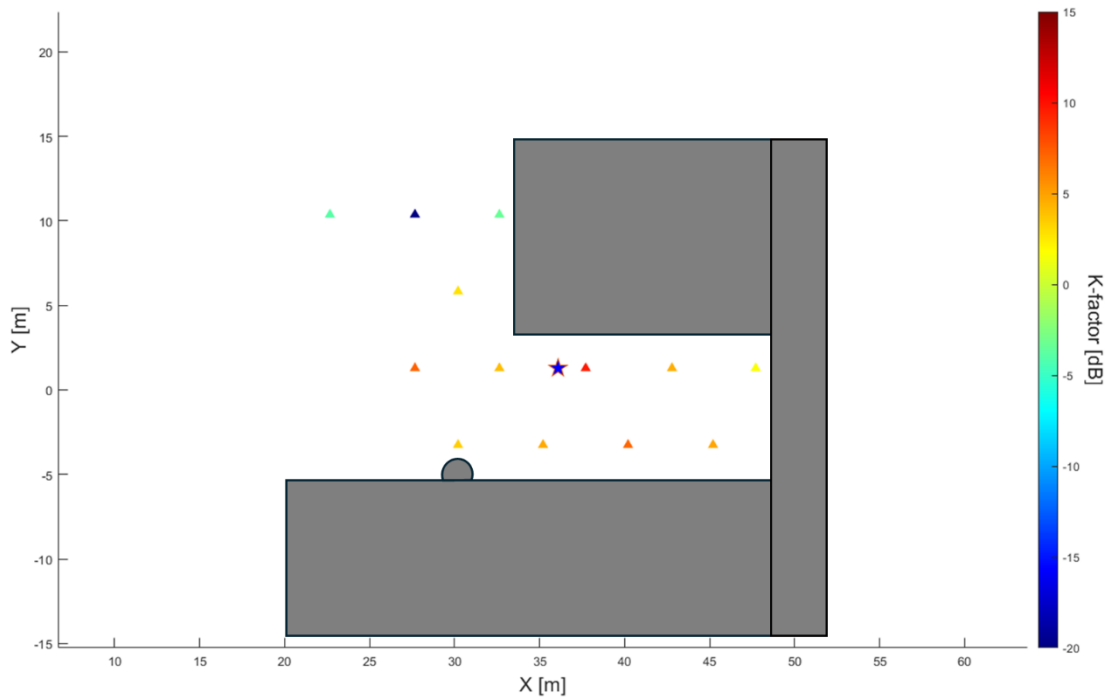


Figure 78. FR2 channel K-factors

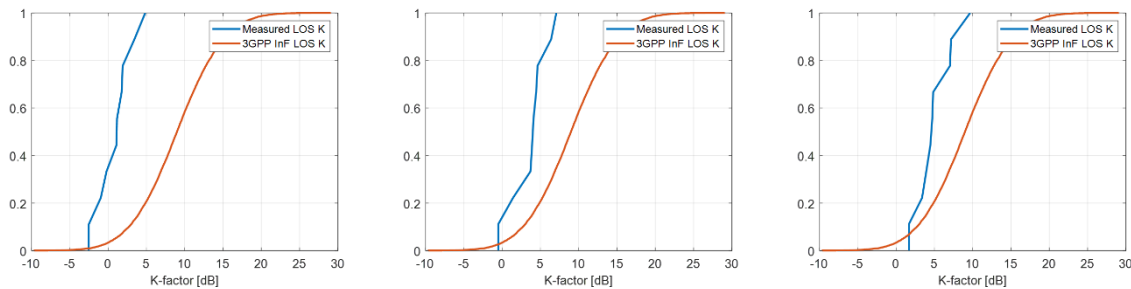


Figure 79. K-factor CDF FR1 (left), FR3 (middle) and FR2 (right)

5.4 PATHLOSS ANALYSIS

Measured and estimated distance-dependent path losses are illustrated for the three measured frequency ranges FR1, FR3, and FR2 in layout plots Figure 80 -Figure 82, respectively. There are separate sub-figures for each of the three Tx locations. The Tx location is denoted by a blue pentagram and Rx locations with coloured triangles. The colour indicates the path loss in decibels. As expected, we can observe that the delay spread increases with increasing link distance and apparently correlates with the LOS/NLOS condition. It is also expected that the rise in pathloss with respect to Rx – Tx link distance is higher in the higher frequencies and is very distinct in the case of FR2 frequencies.

Estimated path loss values are collected to empirical CDF and subsequent curves are illustrated in Figure 83 for the three frequency ranges. CDF curves are plotted separately for the LOS and NLOS links. Moreover, corresponding path loss CDF curves from the 3GPP Urban Street Canyon (UMi) [25] are drawn for comparison using the link distances of measured links.

Estimated path loss samples, regression lines (floating intercept), and 3GPP path loss model curves are shown in *Figure 84*. We can observe that the measured LOS pathloss line is very close to the FSPL line in all frequencies. When compared to the 3GPP-UMi model for LOS paths, we can see that the fitted 3GPP-UMi line has a much steeper slope than what is the case in the measured LOS curve. This same trend can be seen in the CDF curves in *Figure 83*. The 3GPP model expects a little steeper rise in pathloss, although in the densities of the CDF and middle ranges of the floating intercept plot, these measures are very close to each other. For the NLOS paths the measured pathlosses and the 3GPP-UMi reference model are somewhat close to each other, although the low amount of available NLOS paths makes these results somewhat inaccurate.

For both, the measured and the 3GPP-Umi model pathlosses, the pathloss exponents and shadow fading were extracted. Shadow fading is determined by calculating the standard deviation of the pathloss measures differing from the calculated floating intercept fit line. Numerical path loss exponents and intercepts for FR1, FR3, and FR2 are collected to summary Table 23, Table 24 and Table 25, respectively.

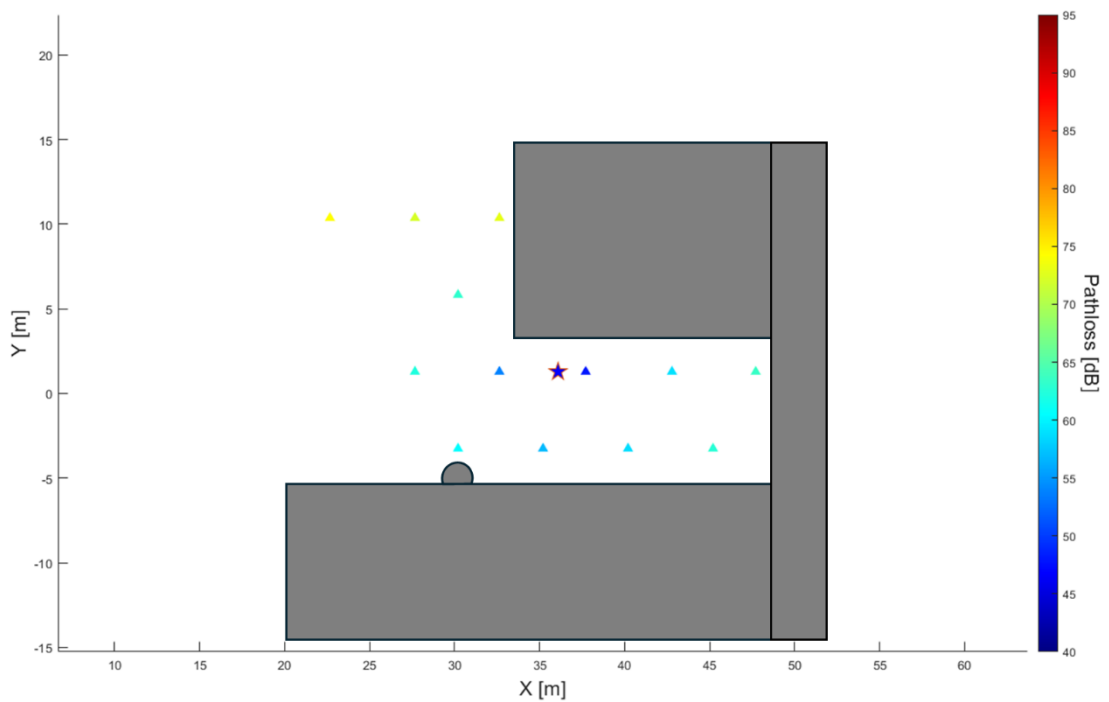


Figure 80. FR1 channel pathloss.

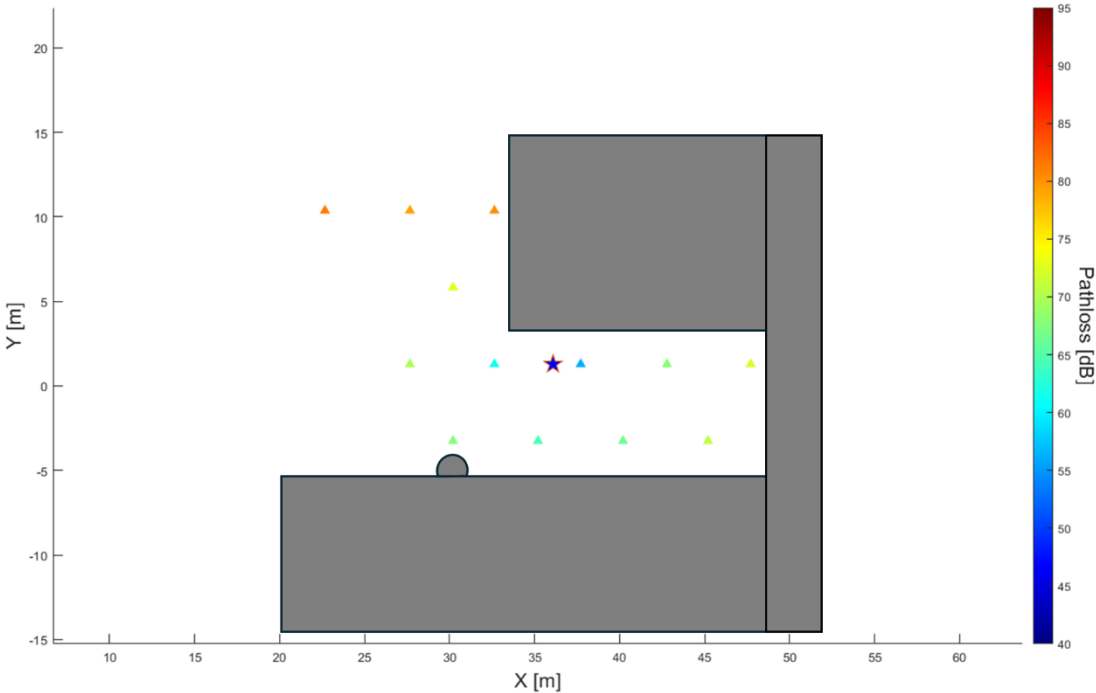


Figure 81. FR3 channel Pathloss

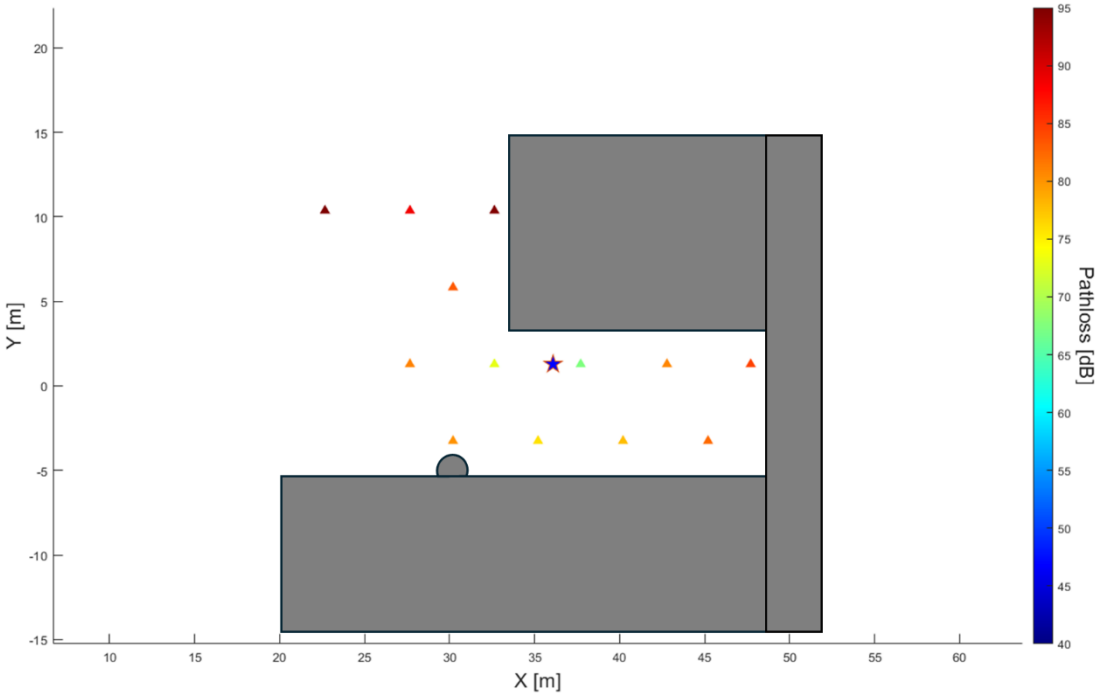


Figure 82. FR2 channel Pathloss

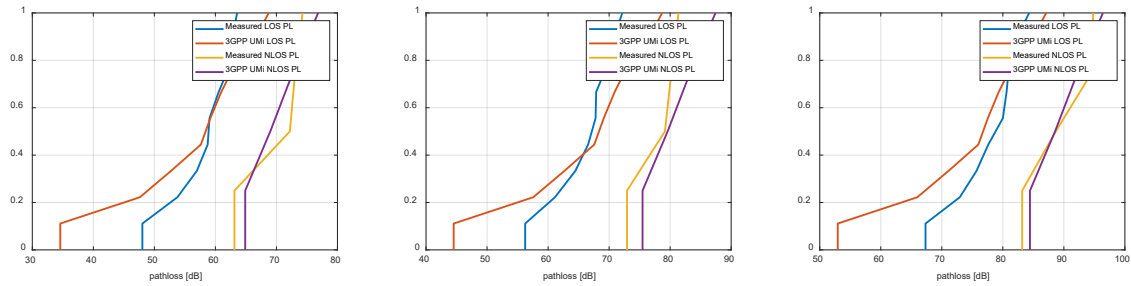


Figure 83. Pathloss CDF FR1 (left), FR3 (middle) and FR2 (right)

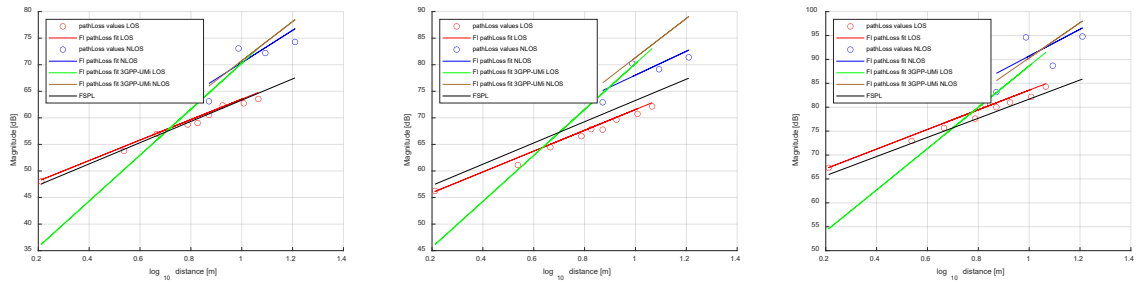


Figure 84. Floating intercept fit of measured FR1(left), FR3 (middle) and FR2 (right) and 3GPP UMi model pathloss

5.5 COMPARISON OF LSPS WITH 3GPP 5G INF CHANNEL MODELS AND DISCUSSION

In the following we compare the LSPs for the Campus scenario, studied in the present section, and the LSPs for the industrial scenario already presented in Section 3, with reference 3GPP models. In particular, Table 23 compares measured and 3GPP-modeled propagation parameters for InF (Indoor Factory) and UMi (Urban Micro) outdoor campus environments under LOS and NLOS conditions for FR1 frequency band. Measured path loss (PL) values, including the exponent and mean, are generally lower than 3GPP predictions, indicating less severe propagation loss in real environments. Delay spread (DS) and shadow fading (SF) also show lower variability in measurements compared to the models, reflecting more stable propagation conditions. The K-factor (representing the dominance of the line-of-sight component) is higher in LOS scenarios, with 3GPP overestimating its values in some cases. Indoor environments exhibit lower path loss and delay spread than urban environments, consistent with fewer obstacles and confined propagation paths. Overall, 3GPP models appear conservative, often overestimating losses and variability, underscoring the need to validate them with real-world measurements for better accuracy in network planning.

Table 23: Statistics of estimated FR1 (2.5-4.5 GHz) large-scale parameters and comparison to corresponding 3GPP model parameters.

	InF measured		InF 3GPP		UMi measured		UMi 3GPP	
	LOS	NLOS	LOS	NLOS	LOS	NLOS	LOS	NLOS
PL exponent	17.53	22.93	SL: 23.03 DL: 23.03	SL: 26.89 DL: 93.08	19.27	30.43	43.23	36.87
PL intercept [dB]	43.08	42.11	SL: 42.48 DL: 42.48	SL: 43.88 DL: 43.63	44.26	39.96	27.05	33.88
PL μ [dB]	57.44	64.15	SL: 65.45 DL: 65.45	SL: 73.32 DL: 145.53 DL	58.41	70.67	62.72	72.90
PL σ [ns]	6.15	5.90	SL: 9.02 DL: 9.02	SL: 7.01 DL: 26.66	4.68	4.42	11.60	4.87
SF σ [dB]	1.13	2.52	SL: 0.56 DL: 0.56	SL: 0.35 DL: 2.73	0.47	2.46	0.80	0.20
DS μ [ns]	23.43	30.63	25.03	30.70	16.42	36.35	73.81	155.62
DS σ [ns]	6.90	6.66	8.89	14.11	4.81	12.34	79.89	178.67
K-factor μ [dB]	-3.70	-7.31	7	-	1.17	-15.85	9	-
K-factor σ [dB]	8.30	8.58	8	-	2.10	7.20	5	-

Table 24 provides updated data comparing measured and 3GPP-modeled propagation parameters for InF (Indoor Factory) and UMi (Urban Micro) scenarios under LOS and NLOS conditions for the FR3 frequency band. Measured PL exponents and intercepts are consistently lower than 3GPP values, highlighting less severe propagation losses in real environments, particularly in InF NLOS and UMi NLOS cases. DS is generally smaller and less variable in measured data, especially for UMi LOS and NLOS, where urban reflections dominate. Shadow fading (SF) shows significantly lower variability in measurements compared to 3GPP predictions, reflecting more stable environments. K-factor values in LOS scenarios suggest stronger line-of-sight components, while NLOS cases show a weaker dominance, with 3GPP often overestimating the K-factor μ . The discrepancies between measured and 3GPP values, especially for UMi NLOS with high DS σ and PL μ in the models, emphasize the need for adapting models to better match real-world conditions for accurate network planning and systems design.

Table 24: Statistics of estimated FR3 (10-12 GHz) large-scale parameters and comparison to corresponding 3GPP model parameters.

	InF measured		InF 3GPP		UMi measured		UMi 3GPP	
	LOS	NLOS	LOS	NLOS	LOS	NLOS	LOS	NLOS
PL exponent	18.34	27.06	SL: 23.03 DL: 23.03	SL: 26.89 DL: 93.08	19.58	22.48	43.23	36.87
PL intercept [dB]	50.89	47.63	SL: 51.93 DL: 51.93	SL: 53.82 DL: 66.53	51.99	55.56	36.99	44.47
PL μ [dB]	65.84	73.07	SL: 74.90 DL: 74.90	SL: 83.27 DL: 168.43	66.29	78.42	72.67	83.49
PL σ [ns]	6.38	6.92	SL: 9.02 DL: 9.02	DL: 7.10 SL: 26.66	4.73	3.27	11.60	4.87
SF σ [dB]	1.02	3.18	SL: 0.56 DL: 0.56	SL: 0.35 DL: 2.73	0.45	1.78	0.80	0.20
DS μ [ns]	22.63	26.27	25.03	30.70	13.89	21.29	57.74	141.17
DS σ [ns]	7.30	6.50	8.89	14.11	2.73	4.48	59.65	203.02
K-factor μ [dB]	2.66	-4.03	7	-	3.91	-10.76	9	-
K-factor σ [dB]	3.82	7.95	8	-	2.18	9.24	5	-

Table 25 compares measured and 3GPP-modeled propagation parameters for InF (Indoor Factory) and UMi (Urban Micro) scenarios under LOS and NLOS conditions for the FR2 frequency band. Measured path PL values, including exponents and intercepts, are generally lower than 3GPP predictions, indicating less severe real-world losses. This is particularly evident in UMi NLOS, where the measured PL exponent is significantly smaller than the 3GPP model. DS measurements, both mean and variability, are smaller compared to 3GPP values, reflecting less pronounced multipath effects in real environments. Shadow fading (SF) shows greater stability in measured scenarios, with smaller standard deviations than 3GPP predictions, especially for LOS conditions. K-factor μ values highlight a stronger line-of-sight dominance in LOS cases, while NLOS scenarios reveal reduced direct component contributions. Overall, the discrepancies between measured and modelled parameters, particularly for DS and PL, suggest that 3GPP models tend to overestimate propagation losses and channel variability at mmWave frequency bands.

Table 25: Statistics of estimated FR2 (28-30 GHz) large-scale parameters and comparison to corresponding 3GPP model parameters.

	InF measured		InF 3GPP		UMi measured		UMi 3GPP	
	LOS	NLOS	LOS	NLOS	LOS	NLOS	LOS	NLOS
PL exponent	17.19	27.07	SL: 23.03 DL: 23.03	SL: 26.89 DL: 93.08	20.54	28.05	43.23	36.87
PL intercept [dB]	63.05	59.30	SL: 59.93 DL: 59.93	SL: 62.24 DL: 85.92	63.03	62.66	45.42	53.44
PL μ [dB]	77.03	84.67	SL: 82.90 DL: 82.90	SL: 91.69 DL: 187.82	77.97	90.31	81.09	92.46
PL σ [ns]	6.16	6.99	SL: 9.02 DL: 9.02	SL: 7.10 DL: 26.66	4.97	4.80	11.60	4.87
SF σ [dB]	1.78	3.38	SL: 0.56 DL: 0.56	SL: 0.35 DL: 2.73	0.67	3.50	0.80	0.20
DS μ [ns]	17.80	17.54	25.03	30.70	20.60	19.80	46.96	136.00
DS σ [ns]	6.55	4.62	8.89	14.11	7.21	13.41	50.33	239.94
K-factor μ [dB]	0.85	-5.80	7	-	5.21	-6.16	9	-
K-factor σ [dB]	6.41	9.00	8	-	2.25	8.41	5	-

5.6 LARGE-SCALE PARAMETERS COMPARISON BETWEEN MEASUREMENTS AND RAY-TRACING

We developed a 3D model of the Aalborg University courtyard measurement site and conducted a ray tracing simulation using the CNIT Ray-tracing tool. This simulation allowed us to compare the measured large-scale parameters with those generated by the model. The constructed 3D model, along with the simulated ray paths, is illustrated in Figure 85. We utilized the CNIT Ray-tracing tool with the parameters outlined in Table 26. Additional details regarding the ray tracing model and its main parameters can be found in [27].

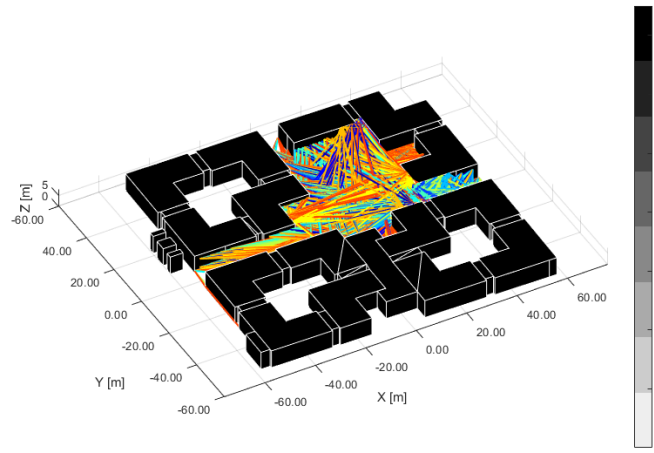


Figure 85. 3D-model of measurement site with simulated ray paths generated for the CNIT raytracing simulation

Table 26: Selected parameters for CNIT raytracing simulation

Parameter	Value
Conductivity (σ)	0.3 (concrete)
Permittivity (ϵ_R)	5.24 (concrete)
Scattering parameter (S_R)	0.45
Scattering pattern model	Directional
Scattering alpha R (width of the scattering lobe) (AR)	1.2
Scattering alpha I (width of the incident lobe) (AI)	1.2
Power division between scattering and incident lobes (K_R)	0.5
Maximum number of interactions	6
Maximum number of reflections	3
Maximum number of diffractions	2
Maximum number of reflections with scattering	1
Maximum number of diffractions with scattering	0
Maximum number of reflection and diffractions in single ray	3
Tile area	25 m ²

The simulated rays, along with their respective powers and delays, were collected, applying the same noise cut threshold used for the measured data. Delay spread was calculated in a manner consistent with the measured data. The K-factor for the simulated data was determined as the ratio of the strongest tap power to the remaining noise cut delay taps. The results are presented in Figure 86.

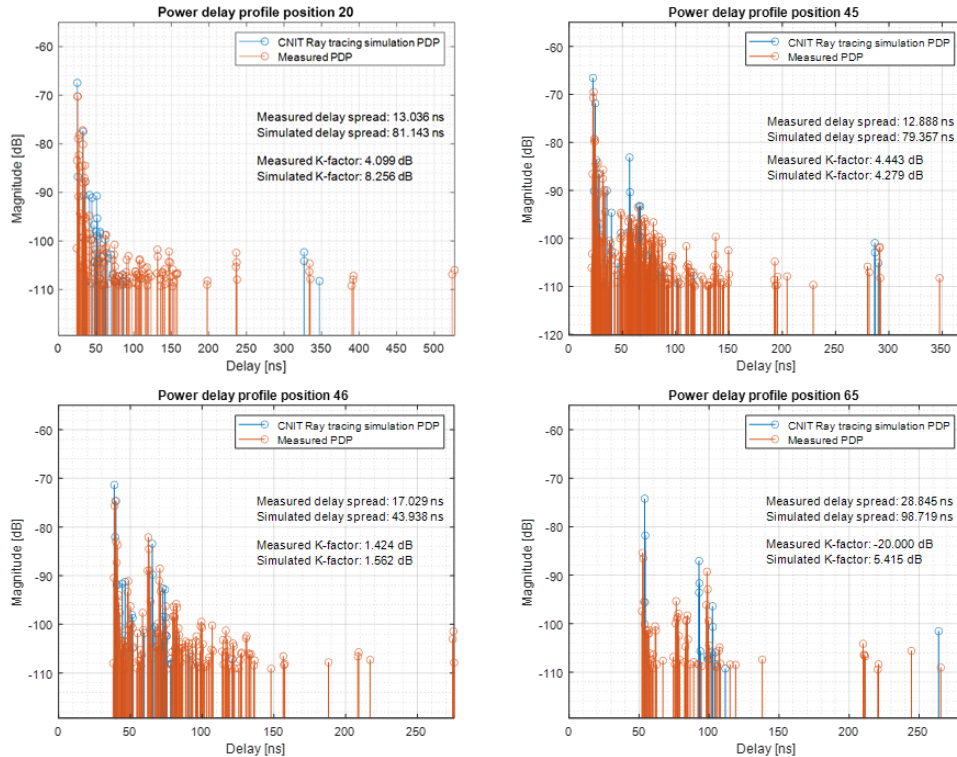


Figure 86. Measured and CNIT simulated PDPs with delay spreads and K-factors calculated (positions 20, 45, 46 and 65) FR3.

It is important to note that the 3D model used for the ray tracing simulation is quite simplistic. Accurately setting various parameters—such as permittivity, conductivity, and other coefficients related to scattering and diffraction—proved challenging for optimal results. Additionally, the model does not account for vegetation and smaller obstacles present in the courtyard.

While the ray tracing simulation’s PDP shows a somewhat close match to the measured PDP, the delay taps are notably sparser. This discrepancy may be attributed to the computational limitations of the available angular resolutions. We are eager to enhance these results in future work.

5.7 SUMMARY

This section focused on the study of propagation in short-range outdoor scenarios. Selected measurement locations from a multi-band measurement campaign in an outdoor campus scenario were collected to extract large scale channel parameters. The analysis of delay spread, K-factor, and path loss for FR1, FR3, and FR2 frequency ranges provides insights into the propagation characteristics of various environments and their comparison with the 3GPP Urban Microcell (UMi) street canyon model.

The extracted large-scale parameters were also compared with the ones obtained from the industrial measurements described in Section 3 and with the 3GPP InF model, in order to provide a comprehensive overview on different types of short-range propagation scenarios.

Delay spread measurements in the campus scenario revealed a dependency on link distance and LOS/NLOS conditions, with higher values for NLOS links at lower frequencies. However, the 3GPP UMi model does not align well with the observed data, especially for short-range links, emphasizing the need for calibrated raytracing simulations to supplement measurements. K-factor analysis showed that measured values are significantly lower than the 3GPP model, particularly at FR1 frequencies, due to multiple strong reflected paths dominating the propagation environment. For path loss, measured LOS values closely follow the free-space path loss (FSPL) line, whereas the 3GPP UMi model predicts steeper path loss, particularly for higher frequencies. NLOS path loss measurements were less consistent due to limited data, highlighting the challenge of modelling propagation in such scenarios. Overall, these findings underscore the need for refined 3GPP models or alternative approaches to better capture short-range and multipath-dominated environments.

Preliminary comparisons between measured PDPs in the campus scenario and simulations with a state-of-the-art 3D ray-tracing tool, specifically parametrized for the FR3 band, look promising.

6 CHARACTERIZING HUMAN BODY SHADOWING AT D-BAND SUB-THZ FREQUENCIES

Given the constraints in physics, such as wave propagation, and the advancements in radio frequency (RF) components, the D-band (110 GHz to 170 GHz) is expected to be the primary frequency band for the initial deployment of sub-THz systems. Over time, this will gradually extend to the upper THz band. Designing and evaluating D-band communication systems necessitates an understanding of radio channel characteristics and the development of corresponding channel models for various application scenarios. More importantly, it becomes crucial to model human blockage for consumer, in-vehicle, and industrial scenarios, where there is a high probability of humans intermittently blocking radio links causing temporal variations in the radio channel.

This study examines the impact of physical obstructions on radio signal attenuation and its temporal characteristics in the D-band. Understanding the fading behaviour caused by physical blockages is crucial for optimizing link handover protocols and quickly establishing stable communication links.

Existing experimental studies on human body shadowing, particularly in the lower mmWave band, such as 3GPP FR2, 60 GHz, and 73 GHz, are of significant interest. These studies primarily focus on modelling the attenuation levels caused by human bodies, which vary based on the relative positions of the Tx and Rx, as well as the temporal variations due to human movement. Additionally, excess attenuation is influenced by body shape, size, and material.

Several human blockage models, categorized into empirical and analytical models, are summarized in the literature [28] - [36]. Empirical models, such as piecewise linear and Gaussian distribution models, are typically derived from measurement data with best-fit parameters. Analytical models, based on knife-edge diffraction (KED) and uniform theory of diffraction (UTD), simplify human blockers into shapes like thin screens and circular cylinders. However, the predictive performance of these models for D-band human body attenuation requires further measurement-based validation.

The goal of this study is to provide initial measurement results to refine the existing diffraction model for D-band human blockage effects and to characterize its temporal variations in radio channels. These measurement results can also be used for stored channel modelling. This work is also reported in [37].

6.1 MEASUREMENT SETUP

The measurement campaign was carried out in an anechoic chamber using a VNA-based channel sounder developed at the University of Oulu. This setup primarily included a Keysight 4-Port PNA-X network analyser (N5247B), Virginia Diodes VNA extension modules, and Pasternack Enterprises WR-6 waveguide standard gain horn antennas, as depicted in *Figure 87*.

Table 27 details the setup parameters for our D-band human blockage measurements, which balanced dynamic range and frequency sweep time to facilitate quasi-time-continuous measurements considering human mobility.

During the measurements, the TX and RX antennas were mounted on positioners at a height of 1.4 meters above the ground and aligned using a laser pointer. *Figure 88* shows the trajectories of individuals walking across the point-to-point LOS link. For side-to-side movement, Case 1 and Case 2 represent a human blocker crossing the LOS link laterally and frontally, respectively. Five distinct

locations along the y-axis were chosen at $y = [0.75:0.5:2.75]$ meters, with increments of 0.5 meters. A person moved slowly from $x = -0.8$ meters to 0.8 meters at an approximate speed of 0.2 m/s. Three test subjects and one standard cylinder were selected, with their physical characteristics summarized in *Table 28*. Before the measurements, back-to-back calibration and reference measurements without human blockage were performed using the same configuration.

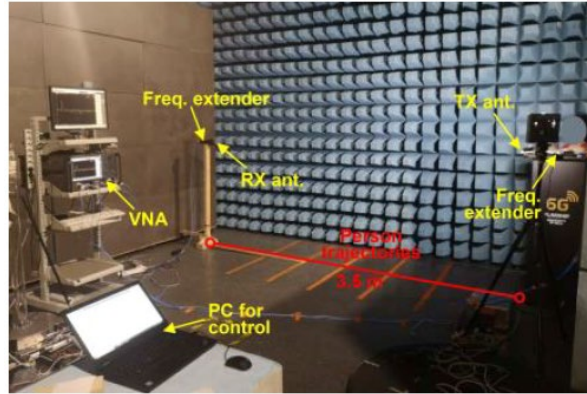


Figure 87. D-band human blockage measurement system

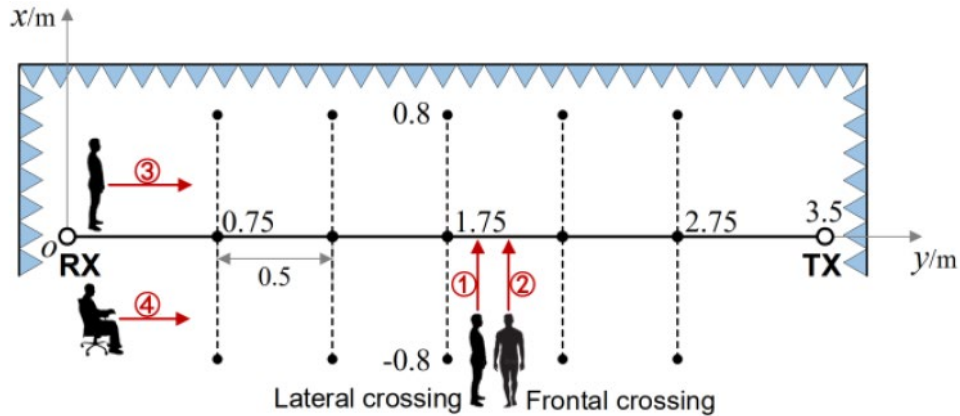


Figure 88. D-band human blockage layout and human trajectories

Table 27: Measurement setup parameters.

Parameter	Unit	Value
Frequency range	GHz	139-141
Bandwidth	GHz	2
Frequency points	/	201
Delay resolution	Ns	0.5
Max. excess delay	Ns	100
IF bandwidth	kHz	100
TX/RX antenna gain	dBi	25
TX/RX antenna 3 dB beamwidth	Deg	10

Table 28. Human measurement subjects' physical dimensions and total number of measurement sweeps.

Test person	Height [m]	Breadth [m]	Depth [m]	Number of sweeps (N)
A	1.65	0.47	0.25	400
B	1.72	0.56	0.30	400
C	1.86	0.63	0.35	400

Cylinder	2.00	ø0.36	600
----------	------	-------	-----

6.2 RESULTS AND DISCUSSION

The channel impulse response (CIR), denoted as $h(\tau)$, is obtained by applying the Inverse Fast Fourier Transform (IFFT) to discrete samples of the channel transfer functions, utilizing a Blackman-Harris window. The power delay profile (PDP) is then calculated by applying noise thresholding as:

$$\hat{P}(\tau) = \begin{cases} |h(\tau)|^2, & \text{if } |h(\tau)|^2 > 4\sigma_{noise}^2 \\ 0, & \text{otherwise} \end{cases} \quad (6.1)$$

where σ_{noise}^2 is the noise floor computed by the variance of last tens of nanoseconds of each CIR, and $4\sigma_{noise}^2$ corresponds to the noise threshold with an approximate 6 dB power threshold above the noise floor. The total power received without human blocker is P_{ref} and in turn, the excess attenuation caused by human activity is computed as:

$$A_n[\text{dB}] = P_{ref} - P_n \quad (6.2)$$

where the received power $P_n = \sum_i \hat{P}_n(\tau_i)$ is calculated as the sum of the power on each delay bin in the PDP, and the subscript $n = 1, 2, \dots, N$ denotes the index for consecutive frequency sweeps over the duration of a walk. Only the delay bins whose received power is above the noise threshold are counted.

Figure 89 illustrates the PDP of the reference measurement for the LOS link without any blockers. Figure 90 presents the measurement results when a cylinder moves across the LOS link, positioned in the middle of the TX-RX line. The temporal characterization of the shadowing event can be expressed as $A(t)$ instead of A_n , by converting the variable from the PDP index n to time t , considering the movement speed and measurement duration.

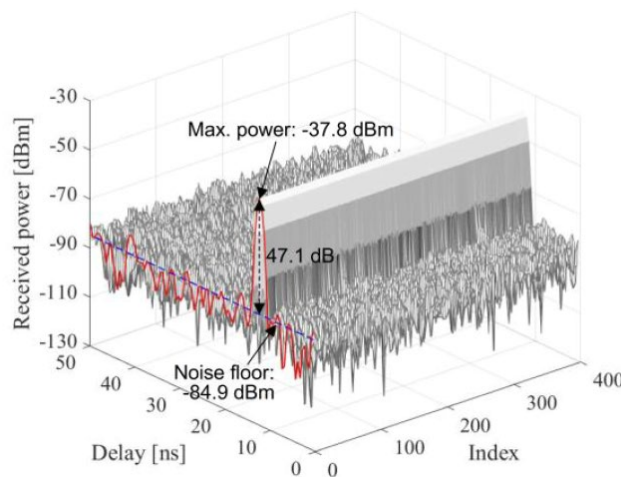


Figure 89. LOS PDP of the link without blockage

A shadowing event is detected when the excess attenuation exceeds a specific threshold. The duration of the shadowing event, t_{SE} , at a specific location along the y-axis, is defined as the time difference between the last zero crossing before and the first zero crossing after the shadowing event. Additionally, the deep fading duration, t_{DF} , is defined as the time difference between the beginning and end of $A(t)$

crossing the threshold, i.e., the fading depth Δ_F , with negative and positive slopes (denoted as t_1 and t_2 in Figure 90). The deep fading duration t_{DF} is a function of Δ_F ; the greater the Δ_F , the longer the t_{DF} .

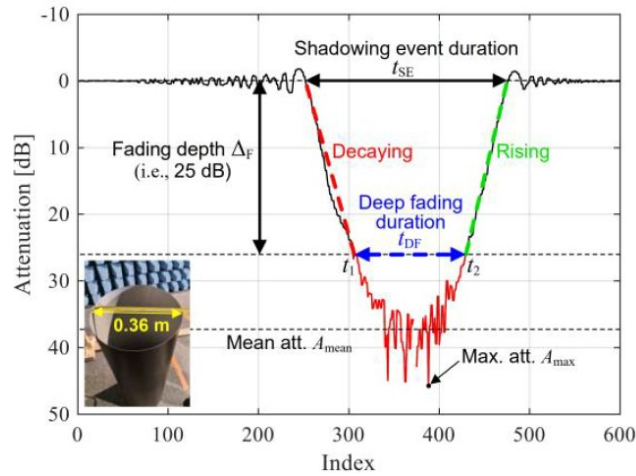


Figure 90. The reference fading pattern of the cylinder

In general, t_{SE} and t_{DF} are determined by the relative distance along the y-axis between the TX (or RX) and the blockage location, as well as the movement speed and physical characteristics of the blocker.

Figure 91 illustrates the measured human body shadowing effects for three test subjects across different trajectories. A slight channel gain is observed when a person enters the LOS path, followed by significant attenuation as the person fully blocks the LOS path. The natural swinging motion of body parts (e.g., hands, torso, and head) causes notable fluctuations before the entire body crosses the LOS path, making it practically impossible for a person to remain completely static during the measurement. The mean attenuation caused by human blockage generally increases by more than 25 dB and 30 dB when the test subjects cross the LOS path frontally and laterally, respectively. The maximum attenuation can exceed 40 dB, depending on the individual. More detailed results can be found in [37].

An alternative link should be established quickly to provide sufficient channel gain when the fading duration significantly exceeds the time delay for beam steering. When t_{DF} is normalized to a walking speed of 1 m/s, the fading duration is on the order of hundreds of milliseconds, which becomes much shorter when a human blocker crosses the direct link frontally.

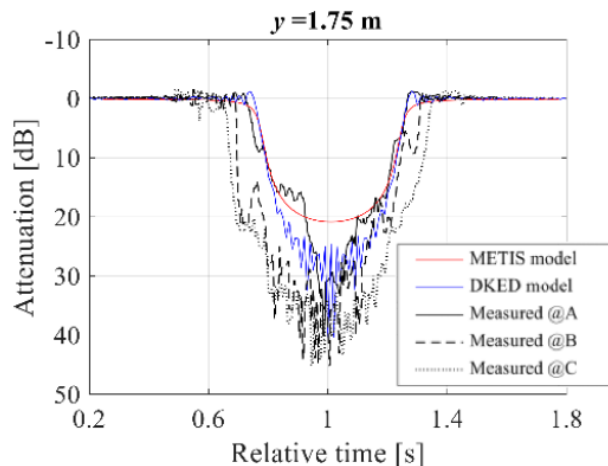


Figure 91. Comparison of D-band human blockage attenuation between measurement and theoretical models for lateral human crossing

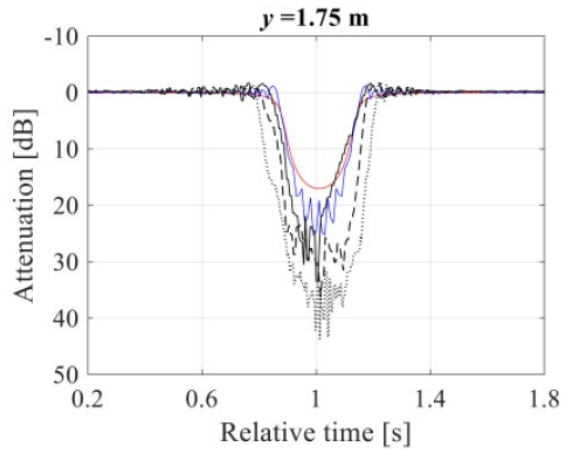


Figure 92. Comparison of D-band human blockage attenuation between measurement and theoretical models for frontal human crossing

6.3 MULTIPATH CHANNEL MODEL INTEGRATING HUMAN BLOCKAGE EFFECT MEASUREMENT SETUP

Let's assume a multipath channel model characterized by a band-/aperture-unlimited double directional power angular delay profile. The human blockage event can then be modelled as additional time variability by introducing an attenuation term $\alpha_l(t)$, resulting in the following channel transfer function:

$$\mathbf{H}(t, f) = \sum_{l=1}^{L_q} \mathbf{g}_{\text{rx}}(\Omega_l^{\text{rx}}) \sqrt{\alpha_l(t) P_l} e^{j(\theta_l + 2\pi v_l t)} e^{-j(2\pi f \tau_l)} \mathbf{g}_{\text{tx}}(\Omega_l^{\text{tx}})^T \in \mathcal{C}^{M \times N} \quad (6.3)$$

where L is the number of paths, $\mathbf{g}_{\text{rx}}(\cdot)$ and $\mathbf{g}_{\text{tx}}(\cdot)$ denote antenna patterns in the direction of Ω_l^{rx} and Ω_l^{tx} , respectively, P_l is path gain, θ_l is a random phase, v_l is Doppler shift, and τ_l is propagation delay. The attenuation term $\alpha_l(t)$ is taken directly from the measurement described in Section 6.1. *Figure 93* presents the measured double-directional channel data, illustrating blockage events on individual paths triggered by the position of the blocker (represented by blue cylinders). *Figure 94* depicts the channel gains of each path varying with normalized time, showing that only certain paths are affected by the motion of the human blocker. Alternatively, instead of a geometric description, blockage events can also be introduced randomly on multipath channels.

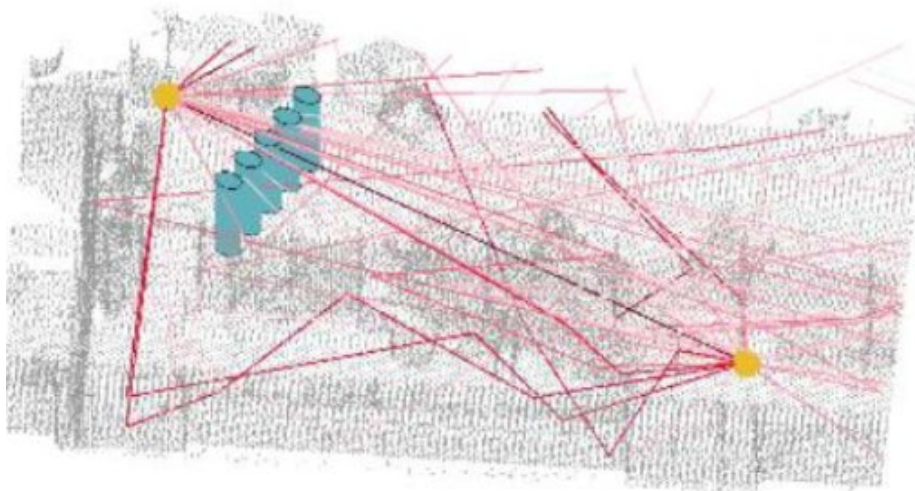


Figure 93. The blockers movement along with the trace of the individual paths

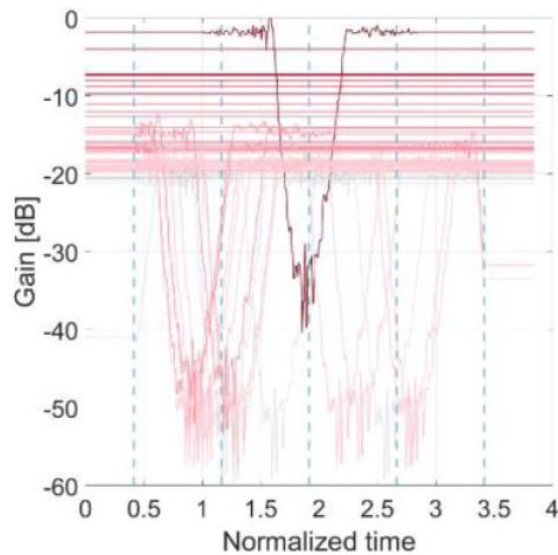


Figure 94. Channel gains over time of the individual path

6.4 SUMMARY

The reported mean attenuation caused by human blockage at 60 GHz is approximately 20 dB [37]. In the D-band, this value increases to over 25 dB and 30 dB when test subjects cross the LOS path frontally and laterally, respectively. The existing analytical models tend to underestimate these attenuation values. Future work should include further studies on the human blockage effect, as outlined below:

1. Measurement-based characterization of human body shadowing across multiple THz bands (e.g., 140, 220, and 300 GHz) using a time-domain channel sounder.
2. Analysis of the human blockage effect in various practical scenarios, such as the sitting case shown in *Figure 88* (case 4) and multi-person scenarios.
3. Development of analytical models based on measurement data by refining the existing analytical models and considering the impact of narrow beam patterns of TX and RX antennas.

Finally, the inclusion of a human blockage component in channel models can be either performed through an analytical modelling approach or a direct replay of measured attenuation patterns.

7 PROPAGATION MODELLING AND MEASUREMENTS FOR RIS-AIDED WIRELESS COMMUNICATIONS

In the present section, we aim at developing new propagation models for Reconfigurable Intelligent Surfaces (RIS), which can be used for propagation studies in different propagation environments where RIS are employed to increase coverage in blind spots, and to support the innovative physical layer solutions for RIS-aided wireless communications studied in WP3. The following section 7.1 deals with macroscopic channel models for RIS, while the next section provides the methodology for assessing the RIS performance in realistic conditions using state-of-the-art measurement systems.

7.1 DEVELOPMENT OF MACROSCOPIC RIS CHANNEL MODELS

RIS can be realized with different technologies, as briefly detailed in the next paragraph. For example, they can be built using the metasurface technology, i.e. as 2D metamaterials, realized in periodic structures composed of several “electrically small” unit cells (where each unit cell has dimensions much smaller than a wavelength). Furthermore, in many realizations available today, RIS are reflectarrays or transmitarrays, i.e. arrays of planar antenna elements with half-wavelength spacing, where each antenna element is connected to a tuneable load. Therefore, it is important to have available models for RIS reradiation that can be used in coverage or system simulations: such models should be both accurate and general enough to be independent of the adopted technology and the specific RIS implementation. This is the main idea behind the “macroscopic” RIS modelling approach, which is presented in this section of the document.

7.1.1 Reflective and Transmissive RISs

Throughout history, humans have sought to control waves, from improving room acoustics to using optical lenses and mirrors, laying the foundation for classical optics. Maxwell’s 19th-century theory of electromagnetism posed the foundation for the development of metamaterials, which manipulate waves beyond the capabilities of natural materials, leading to negative refraction metamaterials and super-resolution imaging. These advancements led to the 2D version of metamaterials: metasurfaces—thin, efficient structures for wave control — now applied in novel antennas, microwave devices, and smart electromagnetic environments. Since metasurfaces might also be reconfigured in real-time, technologies referred to as RIS or Large Intelligent Surface (LIS: with reference to the large dimensions), have emerged as a promising option to engineer the propagation environment and therefore the radio channel[38].

A RIS is a two-dimensional structure made of a substrate with a distribution of electrically small (smaller than the wavelength) metal or dielectric patches printed on it, called meta-atoms [39]. These meta-atoms vary in shape and size to achieve the desired effect on the wavefront of the re-radiated wave when illuminated by an incident wave [40]. Unlike conventional materials, RISs can reshape wavefronts by introducing phase shifts across the surface, allowing efficient control over phase, amplitude, and polarization. Therefore, RIS can infringe geometrical optics laws by realizing anomalous reflection, i.e. reflection with a different angle with respect to the specular one.

A *reflective* RIS re-radiates the incident wave towards the same side half-space whereas a *transmissive* RIS transmits a wave through its surface toward the opposite side, such as in outdoor-to-indoor propagation scenarios. In both cases, a RIS can act as a lens, which requires applying a curvature to the wavefront thus making the wave focus on a given spot, which is very useful to counter path loss for a given user position.

By applying the properties briefly illustrated above, RISs/LISs are intended to realize so-called programmable and reconfigurable wireless propagation environments, i.e., wireless environments that are not considered as external, random or uncontrollable entities but as part of the network components that must be optimized, to fulfil the stringent requirements in terms of coverage and channel characteristics of 6G networks [40]. RIS are often built using tuneable materials needed for their reconfiguration like liquid crystals, phase-change materials, MEMS or varactor/PIN diodes [41]. Their ability to dynamically change their behaviour makes them ideal for systems requiring versatility.

From a technological standpoint, the most common type of RIS is the so-called Phase Gradient Metasurface (PGM) which is conceived to apply a constant phase-gradient to the reradiated wave by means of a periodic meta-atom pattern along a given direction on the surface, therefore realizing an anomalous reflection or transmission along the same direction. PGMs are also referred to as local RIS because their effect on the reradiated wave, as well as the power-balance between the incident, dissipated and reradiated power fluxes at the surface can be considered local. Unfortunately, PGM RIS being periodic, does not reradiate only one single wave in the desired direction, but also a spectrum of parasitic waves corresponding to the propagating Floquet’s modes [42]. Parasitic modes are function of the incident direction and can be suppressed at the expense of power efficiency [43]. Other RIS technologies are available nowadays that exploit surface-wave propagation within the substrate to realize non-local designs that can suppress parasitic modes without sacrificing power-efficiency and realize quasi-perfect anomalous reflectors. Their ideal behaviour, however, only takes place for a single illumination direction of design [43]. Moreover, real-world RISs have a finite size that generate edge diffraction, while illumination conditions are usually far from being far-field, plane wave illumination with a single incident direction. Following the considerations above it is evident that:

- Electromagnetic propagation in the presence of a RIS is a complex process that involves microscopic propagation phenomena (coupling between meta-atoms, surface waves, etc.) within the structure.
- RISs are far from showing ideal behaviour, i.e. they show dissipation, scattering and multiple reradiation modes, although usually only one of them is the desired one.

While microscopic propagation phenomena are important for small-scale RIS applications like antennas and devices, only the macroscopic behaviour - particularly scattering in the radiative near-field and far-field—matters for designing large intelligent surfaces in wireless networks.

7.1.2 Power Balance on a RIS

To model RIS accurately, first a power budget must be imposed on the structure. Power balance proposed in [44] is extended by considering a general-purpose RIS that can reradiate the incident wave

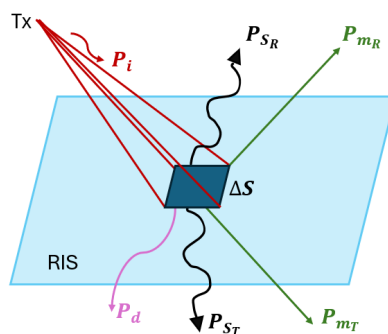


Figure 95. Bilateral power balance at a generic surface element

into both half-spaces: forward (transmission half space) and backward (reflection half space). The power balance (see *Figure 95*) is defined for the local surface element: while it is local, to consider non-uniform RIS realizations and non-plane wave illumination, that imply different incidence angles and different behaviour at different positions, non-local effects at the wavelength scale can be considered through the amplitude factor of the spatial modulation coefficient that is applied at a later stage. Thus, the power balance in at the generic surface element dS takes the following form:

$$P_i = P_S + P_m + P_d \quad (7.4)$$

where P_S is the total diffuse scattered power (due to mechanical or electrical inaccuracies), P_m is the total reradiated power in the specular and anomalous directions and P_d is the power dissipated due to material losses. Since the model accounts for a RIS that is designed to both anomalously transmit and reflect the incident wave, total diffuse scattered power is expressed as:

$$P_S = P_{S_R} + P_{S_T} \quad (7.5)$$

where P_{S_R} and P_{S_T} are the diffuse scattered powers in reflection and transmission respectively. The same holds for:

$$P_m = P_{m_R} + P_{m_T} \quad (7.6)$$

where P_{m_R} and P_{m_T} are the reradiated powers in the backward and forward, respectively. To characterize the power balance at the generic RIS surface element, we introduce the reradiation coefficients m_R and m_T that determine the fraction of incident power that is reflected and transmitted into specular and anomalous modes. It is worth mentioning that in the case of periodic or locally periodic structures, the coefficients m_R and m_T can represent the power amplitude of Floquet modes. The power balance in (7.1) can be rewritten by expressing all its terms as a function of the incident power P_i :

$$P_i = R_R^2 m_R P_i + S_R^2 m_R P_i + R_T^2 m_T P_i + S_T^2 m_T P_i + \alpha P_i \quad (7.7)$$

In (7.4), dissipated power P_d is expressed as a function of incident power by using the dissipation parameter α that is the percentage dissipated in the substrate. In the above equation a reduction factor R^2 is applied to both backward and forward reradiation modes. Moreover, differently from the definition of S^2 in [45], the diffuse scattering coefficient S^2 is redefined as the ratio between total diffused power in the reflection (transmission) half-space and total reradiated power in the reflection (transmission) half-space. For both the diffuse scattering coefficient S and the reduction factor R , subscripts "R" and "T" are used to distinguish between the reflection and the transmission half-space, respectively. If we assume a perfectly smooth RIS and without physical or electrical imperfections, there would be no scattered power ($S_R = S_T = 0$) and the reduction factors R_R and R_T would become equal to 1: then in this case (7.4) would reduce to:

$$1 = m_R + m_T + \alpha \quad (7.8)$$

Here m_R , m_T and α are parameters that range from 0 to 1. Furthermore, this set of parameters may depend on the angle of incidence of the illuminating wave, which changes along the RIS surface for near-field illumination. Therefore, the power balance in (7.4) and (7.5) holds only locally. However, for far-

field illumination this power balance can be applied globally to the whole RIS. Combining (7.4) and (7.5), the following relations between S and R are obtained:

$$S_R^2 + R_R^2 = 1 \quad (7.9)$$

$$S_T^2 + R_T^2 = 1 \quad (7.10)$$

Equations above shows that the higher the diffused power in reflection, the lower the reradiated power. The same holds true for the forward half-space. As known from electromagnetic theory, in non-ideal conditions, RIS can generate multiple parasitic reradiation modes (e.g. Floquet's modes of periodic structures). Let us assume that in general RIS reflects N propagation modes and transmits K propagating modes. To account for multiple propagation modes, we denote with m_{R_n} the reflected power coefficient of the n^{th} propagation mode and with m_{T_k} the retransmitted power coefficient of the k^{th} propagation mode. Then eq. (7.5) can be extended to the case of multiple reradiation modes as:

$$1 = (R_R^2 + S_R^2) \sum_{n=0}^N m_{R_n} + (R_T^2 + S_T^2) \sum_{k=0}^K m_{T_k} + \alpha \quad (7.11)$$

Where $\sum_{n=0}^N m_{R_n}$ and $\sum_{k=0}^K m_{T_k}$ represent total power reradiated in the backward and forward half-space, respectively. In the summations above the indices $n = 0$ and $k = 0$ indicate the specular propagating modes. The power balance ensures that each reradiation mechanism is properly considered in the perspective of a macroscopic but physically sound modelling of a RIS.

7.1.3 Antenna-Array-Like vs ray-based modelling approach

Full-wave electromagnetic methods are impractical for large-scale RIS simulations due to their complexity, so simpler, more efficient models are preferred. However, accurate analysis of RIS performance within wireless networks still requires electromagnetically consistent models that account for non-ideal effects, key RIS parameters, wave transformations, losses, and reradiation distance [45]. Motivated by these considerations, a few research investigations have recently addressed macroscopic scattering from finite-size RIS based on different methods and modelling assumptions [45]-[47]. In [46] it is explicitly accounted for the existence of multiple directions of propagations based on Floquet's theory. This theory is, however, rigorously applicable only to periodic (e.g., phase-gradient) RIS. Also, the main analysis is specialized to the far field of the RIS. In [47] authors develop a ray-based representation of scattering from a finite-size RIS under the assumption that the RIS can be represented as locally periodic. The model proposed in [45] although less rigorous, is more general and accounts for the presence and impact of diffuse scattering that may be caused by, e.g., design trade-offs, construction inaccuracies and dust or raindrops deposit. In this section two approaches for general purpose, macroscopic modelling of scattering from a wide variety of RIS configurations for use in link-level and system-level wireless system simulators are described.

7.1.3.1 AAL approach

The first one is a simplified bilateral Huygens-based modelling approach that relies on the parametric power balance described above and on an "Antenna-Array-Like" (AAL) description of the RIS [45].

Although based on simple theory, this approach is limited to single-bounce scattering. Once the parameters in (7.8) are defined, the field contributions for each reradiating mode must be computed. Referring to a generic n^{th} or k^{th} reradiation mode and omitting the subscripts for simplicity, the RIS contribution to the reradiated field can be described by a spatial modulation coefficient, which can also be viewed as a local reflection coefficient, expressed as follows:

$$\Gamma_m(x, y) = \sqrt{m} A(x, y) e^{j\chi_m(x, y)} \quad (7. 12)$$

where $A(x, y)$ and $\chi_m(x, y)$ are the *amplitude and phase profiles* that the RIS imposes on the reradiated field. The amplitude term $A(x, y)$ has been introduced to account for power-transfer effects due to surface waves in non-local metasurfaces: $A(x, y)$ is normalized as it must satisfy $\iint_{S_{RIS}} A(x, y) dS = S_{RIS}$; $A(x, y) \equiv 1$ for PGM metasurfaces. To compute the reradiated field of the finite-size metasurface, we adopt a discrete Huygens-based approach, modelling the metasurface as a two-dimensional antenna array. RIS is discretized into surface elements ΔS with equal spatial sampling assumed, such that $\Delta S = \Delta x \Delta y = \Delta l^2$. Each element is modeled as an ideal aperture antenna that receives incident power P_i and reradiates a spherical wavelet of power $P_m = mA^2 P_i$ following a specified radiation pattern. These wavelets from all surface elements combine coherently in amplitude and phase to form the overall reradiated wavefront. To prevent grating lobes, it is essential that the element spacing satisfies:

$$\Delta l \leq \frac{\lambda}{2} \quad (7. 13)$$

The approach is based on classic antenna theory and on the concepts of effective aperture A_m and of antenna directivity gain $D_m = \frac{4\pi}{\lambda^2}$ for the reception and the reradiation of each antenna element, respectively. The radiation pattern and therefore D_m and A_m must satisfy the following physical constraint:

$$A_m \leq \Delta S = \Delta l^2 \quad (7. 14)$$

If (7.11) was violated, the power received and reradiated by a square meter of an infinite RIS surface could exceed the incident power, which is clearly impossible. Since an aperture antenna must have a directivity gain greater or equal to 3 [48], it must be:

$$3 \leq D_m = A_m \frac{4\pi}{\lambda^2} \rightarrow \frac{3\lambda^2}{4\pi} \leq A_m \leq \Delta l^2 \rightarrow \Delta l \geq \frac{\sqrt{3}\lambda}{2\sqrt{\pi}} = 0.49\lambda \quad (7. 15)$$

If we combine (7.10) and (7.12) we conclude that the only possible spacing step that is physically sound is $\Delta l \approx \lambda/2$. An antenna that naturally complies with this condition is the Huygens source, whose directivity gain is $D_m = 3$ and whose antenna pattern is:

$$f(\theta_m) = \left(\frac{1 + \cos\theta_m}{2} \right)^2 \quad (7. 16)$$

The electric field intensity $|\Delta E_m|^2$ of the generic antenna element must therefore be:

$$|\Delta E_m|^2 = \Delta E_{m_0}^2 \left(\frac{1 + \cos \theta_m}{2} \right)^2 \quad (7.17)$$

Where $\Delta E_{m_0}^2$ is an amplitude factor to be computed. If the primary source is a transmitter of power and antenna gain P_t and G_t , respectively, we have:

$$|E_i|^2 = \frac{60 P_t G_t}{r_i^2} \quad (7.18)$$

With reference to Figure 96 and by satisfying the power balance at the generic surface element, we calculate the reradiated field intensity of the generic surface element of radiation coefficient m :

$$|\Delta E_m|^2 = mA^2 \frac{60 P_t G_t}{(r_i r_m)^2} \frac{3\lambda^2}{16\pi} (1 + \cos \theta_i)^2 (1 + \cos \theta_m)^2 \quad (7.19)$$

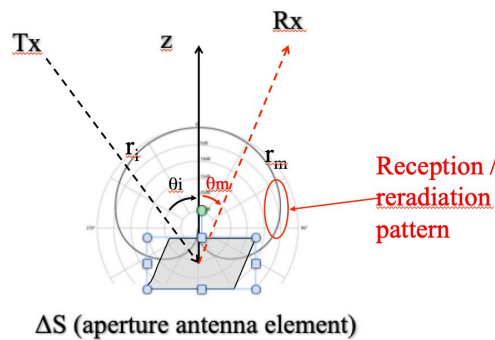


Figure 96. Generic antenna element, its cardioid-shaped radiation pattern and the Tx/Rx geometry

It is important to note that since the maximum effective aperture of the Huygens source (for $\theta_i = 0$) is $A_m = 3\lambda^2/4\pi$ and for $\Delta l = \lambda/2$ one gets:

$$\Delta S = \left(\frac{\lambda}{2} \right)^2 = \frac{\pi}{3} A_m \approx 1.047 A_m \quad (7.20)$$

The Huygens antenna element will not capture exactly the whole power incident on ΔS and therefore the field (7.16) will correspond to a reradiation coefficient slightly lower than $m A^2$. This small gap can be compensated by multiplying the field intensity (9) by $\pi/3$, or by considering a surface discretization with a slightly smaller spacing. Expression (7.16) only gives the field intensity, as it is derived from a simple power balance. The phase of the spatial modulation coefficient (7.9) must now be applied. Moreover, a proper polarization vector must also be applied to account for the polarimetric properties of the reradiated field. The coherent field contribution of the discrete element located at (x, y) to the field in P can be therefore written as:

$$\Delta E_m(P|x, y) = \frac{\sqrt{m 60 P_t G_t}}{r_i r_m} A(x, y) e^{j\chi_m(x, y)} \frac{3\lambda}{16\pi} (1 + \cos \theta_i)(1 + \cos \theta_m) e^{-jk(r_i + r_m)} \widehat{\mathbf{p}}_m \quad (7.21)$$

The total reradiated field at P can be expressed as a coherent summation of the discrete field contributions ΔE_m :

$$E_m(P) = \sum_{u=1}^{N_x} \sum_{v=1}^{N_y} \Delta E_m(P|x = u\Delta l, y = v\Delta l) \quad (7.22)$$

where the sum is performed on $N_x \times N_y$ antenna elements, where $N_x = L_x/\Delta l$ and $N_y = L_y/\Delta l$, being L_x and L_y the linear dimensions of the surface along x and y , respectively. Although the number of elements to be considered can be large, the computation of equation (7.19) is easily parallelizable on today's parallel computing platforms such as Graphic Processing Units (GPU) or multi-core CPUs, in order to achieve good computation speed. The AAL model is a simple, parametric approach that uses proper parametrization of the RIS to describe the reradiated field through a straightforward formula. In far-field illumination scenarios, the parameters m , χ_m and $\hat{\mathbf{p}}_m$ can be easily defined and treated as constant across the surface. A more detailed formulation of the AAL model is provided in [45].

Figure 97 illustrates an example of the scattered field computed using the AAL model for the main anomalous reradiation mode of a 7×7 m phase-gradient RIS centred at the origin. As shown in [45], field computations with the AAL method closely match those obtained using a more rigorous Physical Optics approach based on equivalent currents and the radiation integral.

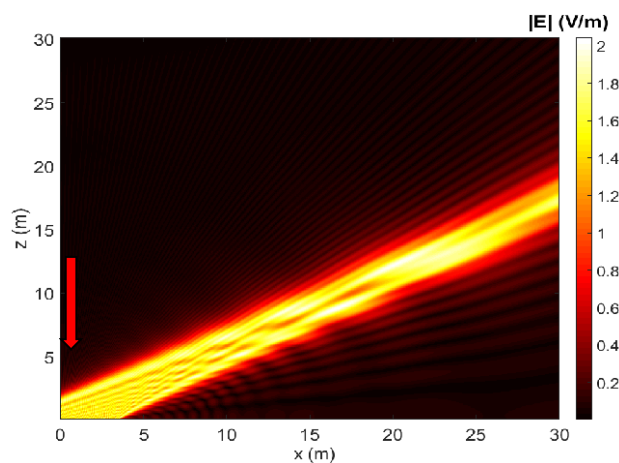


Figure 97. Reradiated field [V/m] in the xz plane for a horizontal xy 7×7 m LIS centred in the origin: $f = 3$ GHz, normal incidence, phase gradient set for TE-polarization

7.1.3.2 Fully ray-based approach

The second approach is a more rigorous and more complex, ray-based representation of scattering from the RIS that can be easily embedded into ray launching propagation simulation tools and therefore can simulate multiple-bounce cases. From a *forward ray-tracing* perspective, it is assumed that the surface of an impedance-modulated RIS is discretized into small surface elements (or "tiles"). Then, using the locally-plane wave assumption, we define the local incident and (anomalously) reflected ray at each tile, following a modification of the classical Geometrical Optics (GO) theory. Simultaneously, we account for the actual curvature of the incident and reflected wavefronts to compute the ray *spreading factor*, which determines the actual attenuation trend of the field with distance along the ray. The goal is to compute the total field reradiated by the RIS in both the far-field and radiative near-field as a set of rays. The procedure comprises the following steps:

- a. computation of the anomalous ray direction
- b. computation of the reradiated field at the RIS surface
- c. computation of the spreading factor

If the RIS has multiple reradiation modes (e.g. Floquet's modes of a locally periodic structure), the procedure above must be iterated for each reradiation mode. Moreover, the same procedure is applied also to diffracted rays from the surface edges, following the well-known approach of the Uniform

geometrical theory of diffraction (UTD) [49] that has been here properly modified to accommodate for the peculiar diffraction process taking place at the edge of a RIS.

A more complete and rigorous formulation of this ray-based modelling approach for RIS can be found in [50]. Although work on transmissive surfaces has already started with the extension of the power balance [44], the model is still limited to reflective surfaces. Moreover, vertex diffraction still must be developed on the base of what is already available in literature for ordinary surfaces, in future work.

Anomalous ray reflection

When a ray impinges on the RIS with propagation direction $\hat{\mathbf{s}}^i$, the field acquires an incidence phase gradient on the tile surface due to the inclination of the locally-plane wavefront of the ray with respect to the tile. Such a phase gradient is:

$$\nabla\chi^i = -k_0 \sin\theta_i \hat{\mathbf{s}}_t^i \quad (7.23)$$

where θ_i is the incidence angle with respect to the RIS normal, $\hat{\mathbf{s}}_t^i$ is a unit vector tangent to the RIS surface that defines the orientation of the incidence plane, and k_0 is the free-space wavenumber. Then, according to a macroscopic approach, the RIS applies the additional phase gradient $\nabla\chi^m$ of the considered reradiation mode so that the *total phase gradient* at the considered tile becomes:

$$\nabla\chi = \nabla\chi^i + \nabla\chi^m \quad (7.24)$$

Anomalous reflection direction takes place according to total phase gradient (7.21). In particular, the reflection plane is parallel to the total phase gradient direction (see Figure 98): however, as surface points with a greater phase will reradiate before those with a phase lag, the resulting locally-plane wavefront will have opposite orientation with respect to the total phase gradient $\nabla\chi$. Therefore, the reradiation direction can be easily computed by observing that:

$$\theta_r = \arcsin\left(\frac{|\nabla\chi|}{k_0}\right); \quad \hat{\mathbf{s}}_t^r = -\frac{\nabla\chi}{|\nabla\chi|} \quad (7.25)$$

with θ_r being the reradiation angle with respect to the normal of the surface, and $\hat{\mathbf{s}}_t^r$ the projection of the reradiation direction on the RIS plane. The reradiation direction $\hat{\mathbf{s}}^r$ is then given by:

$$\hat{\mathbf{s}}^r = \hat{\mathbf{s}}_t^r + \cos\theta_r \hat{\mathbf{n}} = -\frac{\nabla\chi}{|\nabla\chi|} + \cos\theta_r \hat{\mathbf{n}} \quad (7.26)$$

with $\hat{\mathbf{n}}$ being the normal unit vector to the RIS surface. As in [45], the reradiated field can be computed using the *Spatial Modulation Dyadic* (SMD) coefficient (7.9). In addition to the SMD, a proper spreading factor must be also applied to the incident field, to compute the reradiated field at a given point along the reflected ray. The spreading factor for the general case of an astigmatic wave is expressed by [51]:

$$A(s) = \sqrt{\frac{\rho_1 \rho_2}{(\rho_1 + s)(\rho_2 + s)}} \quad (7.27)$$

where s is a local coordinate along the ray, and ρ_1, ρ_2 are the principal curvature radii of the wavefront at the reference point $s=0$. The reciprocals of the principal curvature radii (i.e. the principal wave curvatures), are the eigenvalues of the so-called *curvature matrix* \mathbf{Q} [52],[53].

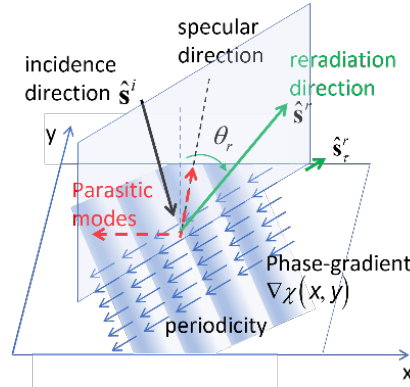


Figure 98. Incident and reradiated rays on a point of a periodic RIS, with representation of the total surface phase gradient.

The surface impedance modulation of the RIS modifies the local curvature of the incident wave. Then, by following an approach like the one adopted in [53], i.e. imposing the phase matching for the incident and reflected wave at the RIS surface, the curvature matrix of the reflected ray can be expressed as a function of the incident curvature matrix $\underline{\mathbf{Q}}^i$ and of the RIS modulation as [50]:

$$\underline{\mathbf{Q}}^r = \underline{\mathbf{1}} - \frac{\widehat{\mathbf{s}}^r \widehat{\mathbf{n}}}{\widehat{\mathbf{s}}^r \cdot \widehat{\mathbf{n}}} \cdot \left[\underline{\mathbf{Q}}^i - \frac{1}{k_0} \nabla \nabla \chi^m(\mathbf{r}'_0) \right] \cdot \left(\underline{\mathbf{1}} - \frac{\widehat{\mathbf{s}}^r \widehat{\mathbf{n}}}{\widehat{\mathbf{s}}^r \cdot \widehat{\mathbf{n}}} \right) \quad (7.28)$$

Where $\nabla \nabla \chi^m$ is the Hessian matrix of the phase modulation function computed at the reference point \mathbf{r}'_0 , and $\underline{\mathbf{1}}$ the identity matrix, while the notation $\mathbf{a}\mathbf{b} \equiv \mathbf{a}\mathbf{b}^T$ stands for the *dyadic vector product*, which is equivalent in linear algebra to the product of a column vector by a row vector, and $\mathbf{a} \cdot \mathbf{b} \equiv \mathbf{a}^T \mathbf{b}$ is the dot scalar product. Finally, the (anomalous) reflected field is expressed, in accordance with the general rules of GO, such as:

$$\mathbf{E}^r(\mathbf{r}) = \underline{\Gamma}(\mathbf{r}') \mathbf{E}^i(\mathbf{r}') A^r(s) e^{-jk_0 |\mathbf{r} - \mathbf{r}'|} = \underline{\Gamma}(\mathbf{r}') \mathbf{E}^i(\mathbf{r}') \sqrt{\frac{\rho_1^r \rho_2^r}{(\rho_1^r + s)(\rho_2^r + s)}} e^{-jk_0 s} \quad (7.29)$$

with \mathbf{r}' being the position vector of the considered tile on the RIS surface, \mathbf{r} the position vector of the observation point, $s = |\mathbf{r} - \mathbf{r}'|$ the local coordinate along the reflected ray, and $\rho_1^r \rho_2^r$ the reciprocals of the non-zero eigenvalues of the reflection curvature matrix $\underline{\mathbf{Q}}^r$, computed with (7.25).

Anomalous ray diffraction

Beside the GO contributions for the RIS reflected field, edge diffracted ray-fields are also included in the model. This type of contribution is important to smooth out the abrupt field discontinuity predicted by GO when crossing the shadow boundaries, i.e., at those observation aspects where the reradiated ray from the RIS arises at a point on the RIS edge, and to predict a nonzero field in the GO shadow region [40]. Since the total phase progression along the RIS edges results from the combination of both the incident wave illumination and the surface impedance modulation, edge diffracted rays are launched toward anomalous directions, similarly to what happens for reflected rays. Therefore, for the first time, the *Anomalous Keller's Cone* is introduced, like the ordinary Keller Cone of UTD, but with an aperture angle that must match the anomalous reflected ray direction. According to a generalized law of diffraction, the diffracted ray direction must obey to:

$$\cos \beta = \widehat{\mathbf{s}}^d \cdot \widehat{\mathbf{e}} = \widehat{\mathbf{s}}^r \cdot \widehat{\mathbf{e}} = \left(\widehat{\mathbf{s}}^i - \frac{\nabla \chi^m}{k_0} \right) \cdot \widehat{\mathbf{e}} = \cos \beta' - \frac{1}{k_0} \frac{\partial \chi^m}{\partial e} \quad (7.30)$$

where β is the aperture angle of the anomalous Keller's diffraction cone, β' is the incidence angle with respect to the edge and \hat{e} is the unit vector along the edge, as shown in Figure 99:

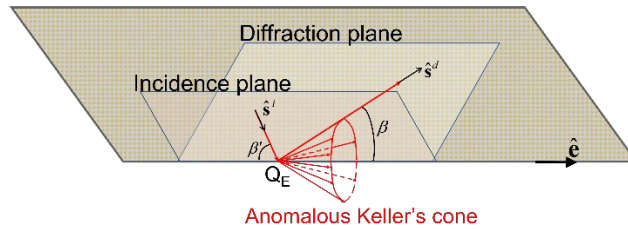


Figure 99. Incident and (anomalously) diffracted ray on a RIS edge

Therefore, one can proceed similarly to the standard UTD case, by recalling that the diffracted wave is astigmatic with one caustic on the edge, and that the diffracted field is computed as:

$$\mathbf{E}^d(s) = \underline{\mathbf{D}} \cdot \mathbf{E}^i(Q_E) \sqrt{\frac{\rho^d}{s(\rho^d+s)}} e^{-jk_0 s} \quad (7.31)$$

In (28), $\underline{\mathbf{D}}$ is the dyadic diffraction coefficient, and ρ^d is the edge-caustic distance, i.e. the distance between the caustic at the edge and the second caustic of the diffracted ray.

To extend the UTD theory to the case of a RIS, the diffraction coefficient introduced in [40] for a perfectly conducting wedge is here heuristically modified by multiplying it by the spatial modulation dyadic $\underline{\mathbf{\Gamma}}$ [50], similarly to the approach adopted in [54] for a non-perfectly conducting surface.

Validation and further work

The above-described ray-based model for reflecting RIS has been validated against the well-established Physical Optics (PO) approach [46] for the same case considered in [50]. The Root Mean Square Error (RMSE) between the two models is about 2.1% of the unit incident field. In Figure 100 a comparison between PO and ray-model results in terms of field strength along a line is reported: the agreement between the two curves is quite impressive. Moreover, the ray-based approach is intrinsically much more efficient: to produce the high-resolution image (1.2 Mpixel) the computation time difference is between 17 hours and 45 minutes of the PO model vs. about 200 seconds for the ray-based approach. Several other validation results are reported in 120[50].

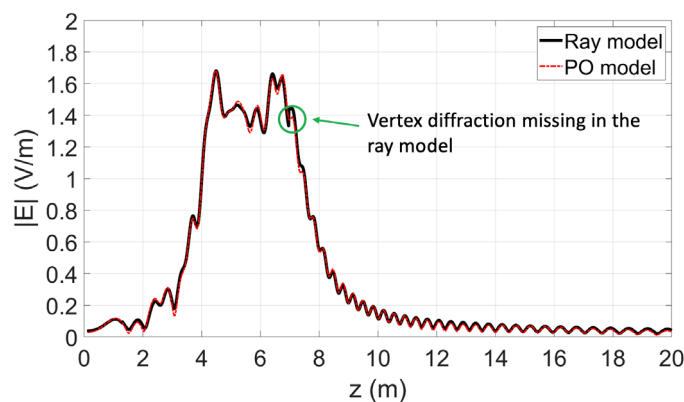


Figure 100. Comparison of the ray model with the PO model in terms of field strength along the dashed

As stated before, the model still needs to be extended to consider transmissive surfaces and vertex diffraction.

7.1.4 Parametrization of RIS models

The parametrization of RIS models involves extracting key parameters from electromagnetic simulations or measurements conducted on fabricated RIS prototypes. All the parameters in the power balance described above are crucial for accurately modelling RIS behaviour. These parameters, such as the reradiation coefficients m_R and m_T as well as the diffuse scattering coefficients S_R and S_T , can be determined through these methods, providing insights into how the incident power is reflected, transmitted, or scattered. However, a crucial aspect of this process is understanding how the incident power is distributed across the surface of the RIS, particularly in non-ideal conditions where effects such as material imperfections play a significant role. This distribution directly influences the accuracy of the power balance and the overall performance of the RIS in real-world wireless network environments. Without a clear understanding of how the incident power interacts with the surface, model predictions may deviate from real-world performance.

7.1.5 Integration of RIS model into deterministic or geometrical-stochastic planning tools

The macroscopic channel models described in previous subsections have been embedded in a 3D ray tracing simulator, then simulations in reference scenarios have been carried out with typical material and RIS parameters for a lossy, phase-gradient anomalous reflector, or for a RIS configured as a focusing lens, considering the use of pre-configured RIS to improve coverage. Realistic values for the RIS efficiency have been considered based on the existing literature and taken into account in the model, in addition to other parasitic effects such as diffuse scattering. Some examples of this evaluations are shown in [36],[41]. Moreover, by exploiting the collaboration between 6G-SHINE and CENTRIC projects, both the proposed RIS models (AAL and fully-ray based model) have been implemented by nVidia into the open-source simulator Sionna Ray Tracing: more details on the implemented functionalities can be found on the following webpage: [Tutorial on Reconfigurable Intelligent Surfaces \(RIS\) — Sionna 0.19.0 documentation](#). [63].

Finally, future activities in the project will deal with the possible implementation of the RIS macroscopic models into a general geometrical-stochastic channel model (GSCM), exploiting the collaboration between CNIT and Keysight. Moreover, synthetic channel impulse responses in reference scenarios generated using a ray tracing tool with the RIS models embedded, will be used to show the real-time performance of RIS-aided communications in the Keysight channel emulator. This will be also part of the PoC of WP5.

7.2 MEASUREMENTS WITH RIS

In order to evaluate the performance of RISs in realistic environment and to validate the proposed macroscopic models, accurate measurement systems are needed. In particular, it is necessary to investigate how a RIS re-radiates the incident field not only in the desired beamforming direction or focusing spot, but also in other directions. In other words, it is important to evaluate the impact of parasitic reradiation modes, and their effect on the system performance. This can be done effectively by using an automated measurement systems that allows to evaluate the 3D re-radiated field by a RIS in an efficient and accurate manner: the above-mentioned system is described in detail in the following subsection 7.2.1.

Also, it is important to introduce a methodology to assess the behaviour of the RIS, and the degradation of its performance, in the situation that one or more of its elements are not working properly. This investigation is called “RIS diagnosis”, and the main results are presented in subsection 7.2.2.

7.2.1 3D radiation characterization of RIS

The capability of the reconfigurable intelligent surface (RIS) to engineer wireless propagation channels has gained great interest in academia in recent years. Knowledge of RIS reradiation characteristics is important. This sub-chapter is based on our work presented in [17]. The authors in [17] present an automated over-the-air (OTA) testing platform designed for characterization of the RIS reradiation. The platform operates in an anechoic chamber, and it uses multiple probes. It is fully automated, and it employs a VNA for performing signal measurement and recording. An illustration of the fundamental geometrical parameters of a RIS aided wireless communication system is presented in Figure 101.

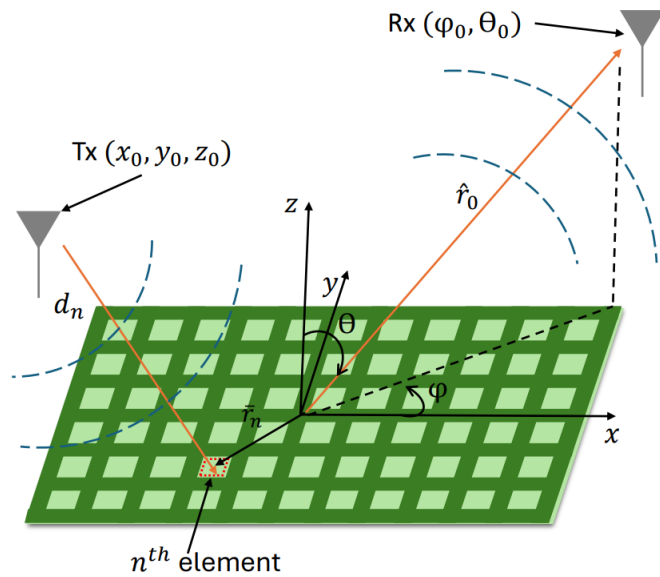


Figure 101. The fundamental geometrical parameters of a RIS aided wireless communication system, where the assumption is that the Rx is positioned in the far-field of the RIS, and the Tx is situated in the near-field of the RIS

For enhancing the communication in a wireless system with an RIS, the effective RIS-based beamforming is important. It optimizes the signal reception from the Tx and aims to direct the signals efficiently to the Rx, resulting in improved communication. The accurate control of RIS element phase shifts is of importance and relies on knowledge of the Tx and Rx locations.

In the presented scenario, the Tx is in the near-field of the RIS, while the receiver Rx is positioned in the far-field of the RIS. Following Equations (1) to (4) from [17], one can obtain the total beamforming phase shift of the n-th RIS elements as:

$$\phi_n = \beta_n + \gamma_n, \quad (7.29)$$

where β_n is the phase shift distribution used to compensate the phase distribution of the received signal α_n and γ_n is the phase shift distribution dependent on the desired direction of beamforming (beam-steering) (ϕ_0, θ_0) . α_n , β_n and γ_n can be estimated based on the following relationships:

$$\alpha_n = -\frac{2\pi}{\lambda} d_n \quad (7.30)$$

where λ is the wavelength of the signal and d_n is the distance between the Tx and the n-th element of the RIS.

$$\beta_n = -\alpha_n \quad (7.31)$$

$$\gamma_n = -\frac{2\pi}{\lambda} \sin\vartheta_0 (x_n \cos\phi_0 + y_n \sin\phi_0) \quad (7.32)$$

where x_n and y_n are the coordinates of the n -th RIS element, θ_0 and ϕ_0 are the elevation and the azimuth angle of the desired beamforming direction.

The proposed automated OTA testing platform for RIS is presented in Figure 102.

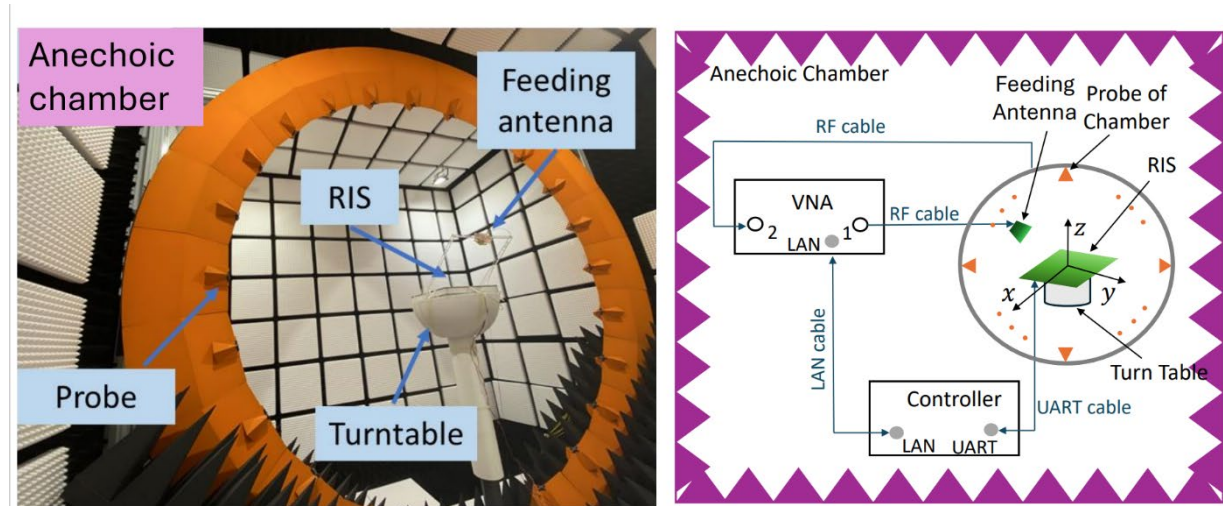


Figure 102. Photo (a) and diagram (b) of the proposed OTA testing system

The RIS under test consists of 10×10 elements and it operates within the 3.4 ~ 3.6 GHz frequency range. More information about the RIS under investigation can be found in table 1 in [17]. Each RIS unit is connected to a 2-bit phase shifter, providing 4 phase states of 0° , 90° , 180° , and 270° . The phase shift accuracy is within $90^\circ \pm 15^\circ$. The RIS is positioned on the turntable, and it is rotated during the measurement to obtain the 3D radiation patterns. The feeding antenna is held by a plastic structure. It illuminates the RIS, and it is located 50 cm away from the RIS centre. Moreover, the feeding antenna is located at an elevation angle of 50° and at an azimuth angle of 0° relative to the RIS centre. The chamber probe antennas are in the form of a ring, and they function as Rx antennas during the measurements. The S_{21} between the feeding antenna and chamber probes were recorded by the VNA for each orientation of the RIS. The VNA operates at 3.5 GHz and utilizes a 100 Hz IF bandwidth and transmitting power of -10 dBm.

The RIS beamforming reradiation pattern measurements show an illustrative example to validate the measurement procedure and the capability of the testing platform. As it is shown in (7.29), the total beamforming phase shift $\{\phi_n\}$ of n -th RIS element consists of two elements: the phase shift $\{\beta_n\}$, which is the phase shift for receiving signals with an opposite sign, and the phase shift $\{\gamma_n\}$ for reflecting signals. A codebook is created based on the phase shifts $\{\phi_n\}$ calculated according to Eq. (7.29) - (7.32) and the available phase shift states. It is then transmitted to the RIS, where it is interpreted by adjusting the phase shift of each element according to the code-book values. Afterwards, the controller activates the probe antennas positioned at different elevation angles with the use of a switch system. The VNA records the transmission coefficients between the feeding antenna and the activated probe antenna. The measurement of the elevation cut of the RIS reradiation is conducted quickly, because the switch

system is driven electrically. After a single elevation cut measurement, the turntable rotates to the next predefined angle to measure the next elevation cut reradiation pattern of the RIS. The switching of the probe antennas and the rotation of the RIS are repeated until all elevation cuts are scanned, which results in a complete 3D pattern scan of the RIS reradiation. The measured reradiation patterns for both beamforming examples are shown in Figure 103 and Figure 104.

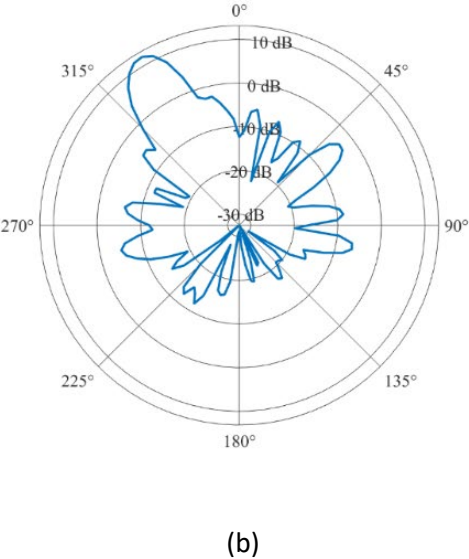
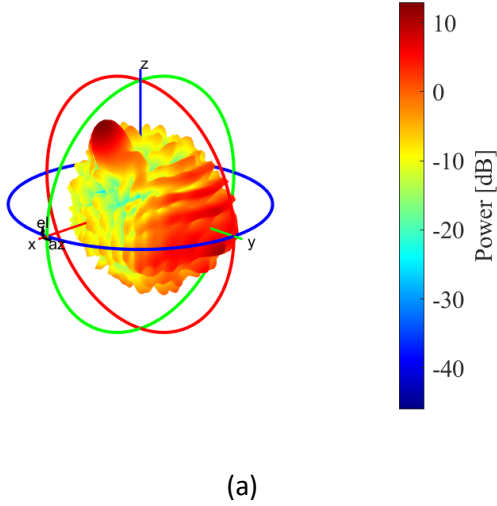
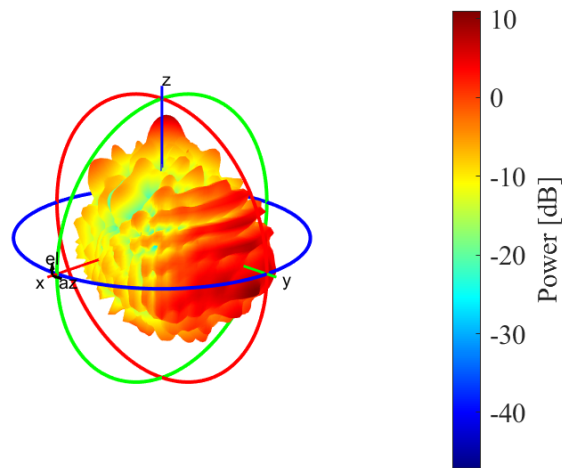
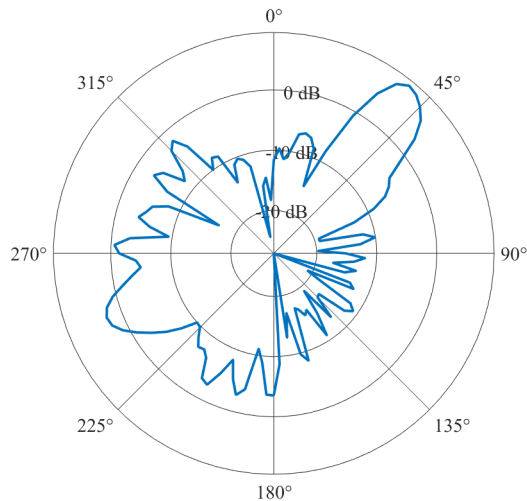


Figure 103. Measured RIS reradiation in the beamforming direction (30°, 0°): (a) 3D pattern and (b) 2D cut pattern with azimuth angle of 0°



(a)



(b)

Figure 104. Measured RIS reradiation in the beamforming direction ($45^\circ, 225^\circ$): (a) 3D pattern and (b) 2D cut pattern with azimuth angle of 225°

The beamforming targets ($30^\circ, 0^\circ$) and ($45^\circ, 225^\circ$) were achieved with acceptable errors. In the first case, the main lobe is at ($30^\circ, 6^\circ$), while in the second it is at ($39^\circ, 225^\circ$). The main lobe peak is 12 dB and 8.7 dB, respectively. The main beam width is 15° and 18° , respectively. Measurements of the RIS reradiation were performed for two different cuts with azimuth angles of 0° and 45° . Figure 105 shows the obtained results for the reradiation patterns.

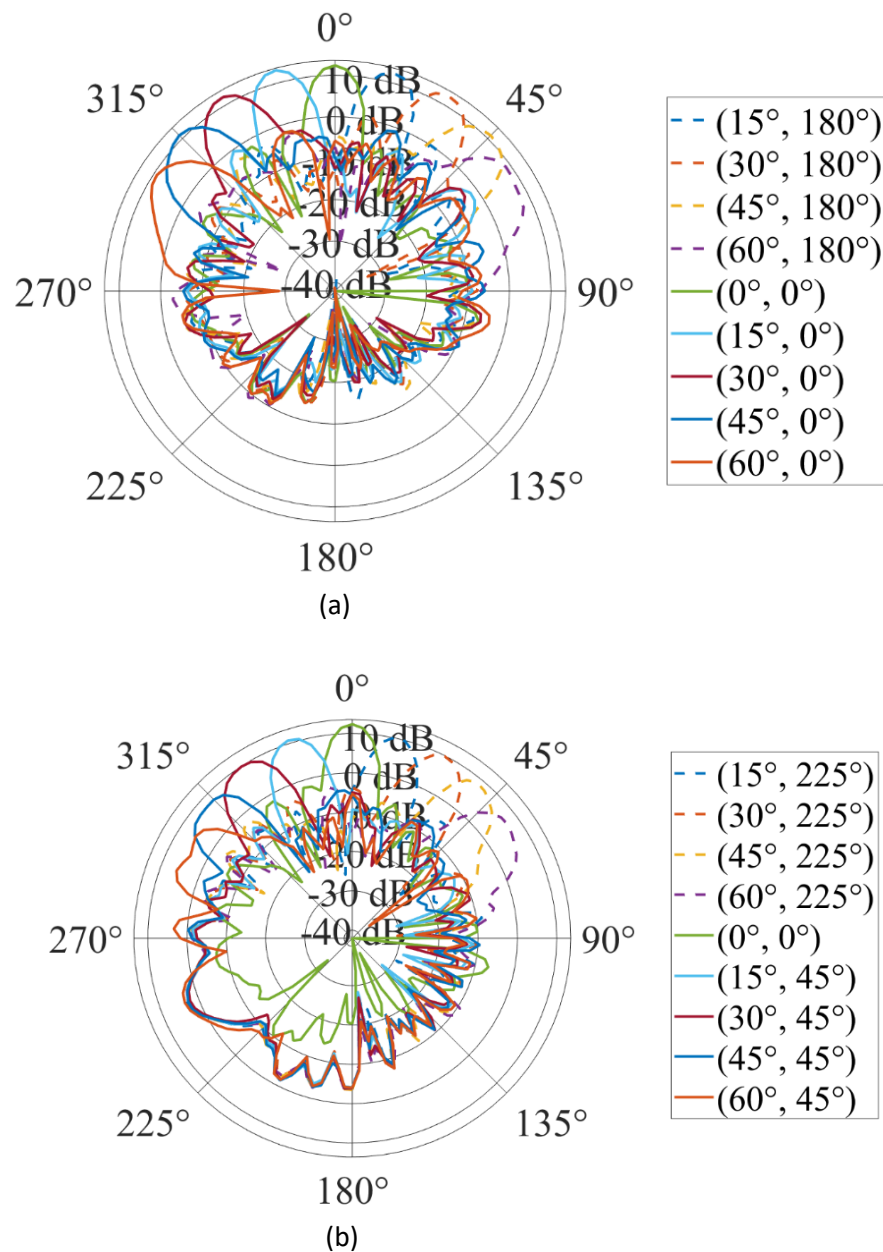


Figure 105. Measured RIS reradiation pattern in two cuts with azimuth angle of: (a) 0° and (b) 45°. The directions of multiple intended beamforming in each cut are as they are shown in the legend

These measurement results validate that the measured beam directions match closely with the desired ones. However, as the elevation angle increases, more noticeable deterioration in the beamforming performance is observed, i.e., the main beam direction error increases, the main beam width widens, and the peak of the main beam decreases. Several factors may contribute to it. The main factor is that the higher the beamforming elevation angle gets, the smaller the effective aperture of the RIS is. As the beamforming elevation angle increases, the physical area available for signal capture decreases, impacting the RIS’s energy concentration ability. Additionally, the limited adjustable phase shift capability and inherent control errors of the RIS element may also impact the accurate beam steering. In conclusion, the following important points of the work must be outlined:

- An automated OTA testing platform for conducting reradiation measurements of RIS was presented.

- The close agreement between measured and theoretical RIS beamforming reradiation patterns validated the capability of the proposed test platform.
- However, performance limitations were observed for high elevation angles. Therefore, further research and optimization is needed.

7.2.2 RIS Diagnosis

RIS phase shifters are prone to malfunction due to the increased likelihood of manufacturing defects or errors associated with their cost-effective design and the large number of units involved. OTA diagnosis is crucial for verifying their radiation characteristics and ensuring reliable performance.

OTA diagnosis of RISs based on complex measurements is proposed in [18]. The proposed solution is low-cost, robust, generic, fast and highly effective. The method is validated experimentally by using the same 10×10 RIS prototype operating at 3.5 GHz (presented in [17] and in the previous sub-chapter). The measurement setup for the proposed RIS diagnosis is illustrated in Figure 106.

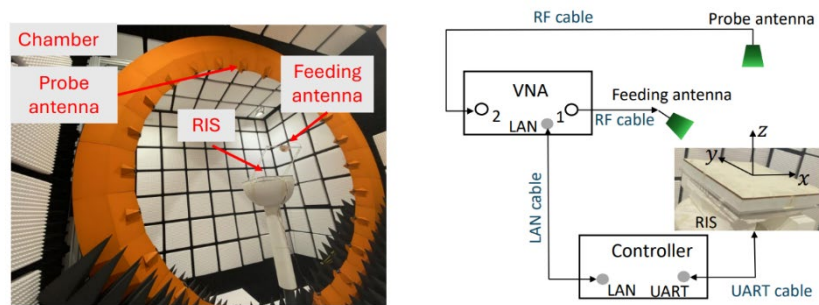


Figure 106. RIS diagnosis measurement setup: (a) photo and (b) diagram

The measurement setup is the same as in the one presented in the previous sub-chapter. The feeding antenna illuminates the RIS, and the mentioned probe antenna records the composite field reflected by the RIS elements. The IF bandwidth and the transmit power of the VNA are set to 100 Hz and -10 dBm, respectively. The distance between the feeding antenna and the centre of RIS is 50 cm. Moreover, the feeding antenna is positioned in a direction with an azimuth angle of 0° and an elevation angle of 50° with respect to the RIS, respectively. Only the probe antenna in the RIS bore-sight direction is used to capture the reflected signals from the RIS. The distance between the probe antenna and the centre of the RIS is 1.75 m. The phase tuning of the RIS and the operation of the VNA is performed automatically. Equations (1) to (5) in [9] are used to define the received signal variation:

$$\Delta_n \approx \begin{cases} 2E_n & \text{the phase shifter works} \\ 0 & \text{the phase shifter fails} \end{cases} \quad (7.33)$$

where E_n denotes the amplitude of the complex signal received by the probe antenna port that is reflected by the n -th RIS element. VNA records the complex transmission coefficient S_{21} between the feed antenna and the probe antenna.

The measurement is conducted following the procedure below:

- Step 1: Set the phases of all RIS elements to 0° and measure the complex signal y_n^0 recorded at the Rx antenna port
- Step 2: Set 180° to the n -th RIS element and 0° to the rest of the RIS elements, and measure the complex signal y_n^π recorded at the Rx antenna port
- Step 3: Calculate the received signal variation Δ_n for the n -th RIS according to (5)
- Step 4: repeat step 1 to 3 for all RIS units to obtain Δ_n with $n = 1, 2, \dots, N$
- Step 5: Compare Δ_n among RIS elements and detect the faulty element(s)

In measurements, Δ_n will be approximately zero in case of failed RIS element. On the other hand, if the phase tuning of n-th RIS element works as expected, Δ_n will be significantly higher than that for the previous case when the n-th RIS element is faulty.

The proposed diagnosis method was examined and validated by assuming five scenarios. In practical applications, the number and the locations of the faulty elements can be arbitrary. Therefore, to test the robustness and the effectiveness of the suggested method, the following validation cases were chosen:

1. Scenarios without any faulty RIS elements
2. Scenarios with one faulty element - malfunction of one edge RIS element with index 8
3. Scenario with one faulty element - malfunction of one non edge element with index 15
4. Scenario with two faulty elements - malfunction of RIS elements with index 65 and 66, which are positioned around the RIS centre
5. Scenario with four faulty elements - malfunction of the RIS elements with index 8, 15, 65 and 66

It is worth noting that a faulty element is “programmed” by keeping the phase of the RIS element at 0° to mimic the malfunctioning phase shifters. Firstly, all RIS element phase shifters are set to 0° , the measurement of the S_{21} is conducted. Afterwards, each of the RIS element phase shift is set to 180° sequentially while keeping phase shifters of the other RIS elements to 0° . The S_{21} between the feeding and probe antennas was measured for each RIS excitation setting. Therefore, there are in total 101 S_{21} measurements for each scenario under investigation. The obtained results are shown in Figure 107.

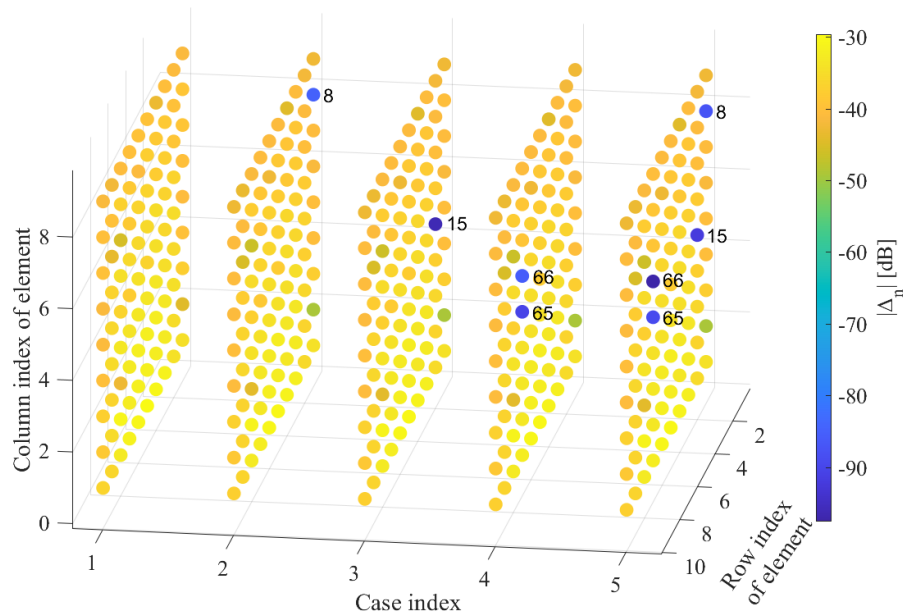


Figure 107. The proposed RIS diagnosis method applied to five scenarios

In Scenario 1, Δ_n varies within $[-50, -30]$ dB. Higher values for Δ_n can be observed for the RIS elements positioned closer to the feeding Tx antenna. The reason is the different illumination of the RIS elements by the feeding Tx antenna. In Scenario 2–5, all the faulty elements are detected correctly. The received signal variation Δ_n associated with the faulty elements are below -80 dB, which in practice secures a gap of more than 30 dB compared to Δ_n of the fault-free RIS elements.

7.2.3 Summary

In conclusion, the proposed method can be defined as valuable and effective owing to the following advantages:

- Cost-effective setup: the proposed algorithm is based on measurements in the mid-field of an RIS (i.e., the feeding and probe antennas are in the mid-field of the RIS).
- Robustness: the received signal variation Δ_n among the fault-free RIS elements is at least 30 dB higher than that of the faulty RIS elements to avoid fake alarm.
- Short measurement time: the entire measurement procedure can be conducted in an automatic manner without the need of any mechanical operations, because the RIS, the feeding and the probe antennas are fixed, and the control of RIS is made automatically with the use of a control computer.
- Generic RIS diagnosis solution: the proposed algorithm works for 1-bit RIS (i.e. with phase setting of 0° and 180° only).

8 CONCLUSIONS AND RECOMMENDATIONS

This deliverable summarizes the key achievements of WP2-Task 2.2 of the project, focusing on propagation measurements and channel modelling in the scenarios of interest. The measurements were primarily conducted in industrial and vehicular environments using a VNA-based channel sounding system, covering multiple frequency bands from sub-6 GHz to sub-THz frequencies. Additional measurements were carried out in order to evaluate propagation in a short-range outdoor campus scenario and to characterize human-body shadowing in the D-band. Furthermore, an automated measurement system for 3D characterization of RIS reradiation was developed, along with a procedure for RIS diagnostics to assess the impact of multiple faulty RIS elements on overall performance. Special emphasis was placed on the emerging frequency bands identified as critical for the 6G ecosystem [22], particularly FR3 and sub-THz frequencies.

For industrial measurements, the analysed scenarios included: (1) spatial map measurements in both LOS and NLOS locations using omnidirectional antennas, (2) short-range measurements near a robotic arm and a production line, and (3) VAA and large-scale VAA measurements for comprehensive characterization. From a channel modelling perspective, industrial spatial map measurements were extensively analysed, with key channel parameters such as path loss, delay spread, and Rician K-factor extracted and compared against reference 3GPP models. Notably, the delay spreads were found to align with the median range of the reference model. However, measured Rician K-factors were generally low, reaching up to 10 dB only in extreme cases. This indicates that the LOS component does not dominate even under clear LOS conditions, as several strong multipath components contribute significantly to the signal.

Regarding the vehicular environment, the analysis of measurements under different conditions (in-cabin, inside engine bay, LOS, O-LOS, and outdoor-to-indoor) has highlighted a rich scattering propagation of the radio signal and low attenuation caused by internal furniture for a wide range of frequencies: this result confirms the feasibility of in-vehicle subnetworks in the low frequencies (FR1), mmWave (FR2), and 8-12 GHz bands, as radio channels show many similarities in these 3 cases. On the other hand, a different behaviour is observed for sub-THz frequencies, with a higher degree of channel sparsity, due to the strong attenuation of the path and the use of highly directive antennas. Observations related to outdoor-to-indoor propagation have also been carried out, specifically for the frequencies 8-12 GHz (belonging to the FR3 mid-band) and for sub-THz frequencies (D band): the results in terms of penetration loss through different vehicle components have shown the possibility of inter-vehicle communication in the FR3 band, with the possibility for the radio signal to overcome the obstacle represented by metallic obstacles thanks to the diffraction effect. Instead, penetration through the vehicle is not possible at sub-THz frequencies, with the sole exception of windows, due to the high penetration and propagation attenuation typical of these frequency bands. The above-mentioned study therefore provides useful indications for the design of vehicular subnetworks, including the possibility of communication - or isolation, with beneficial effect on interference protection - between subnetworks implemented in different vehicles.

The document has then analysed the characteristics of the radio channel in short-range scenarios, in the presence of shadowing by human bodies at sub-THz frequencies, and proposed macroscopic models for RIS, which can be used for planning studies with the aim of improving the radio coverage and optimizing RIS-aided wireless communications. Finally, an accurate measurement system was realized that will allow in the future to evaluate the realistic performances of RIS prototypes, and to validate and parameterize the novel RIS macroscopic models that have been introduced in WP2. The latter studies

apply to all the use case categories proposed in the project, and in particular to consumer and industrial scenarios.

The outcomes of the studies will be used in the last year of the project to parametrize deterministic channel models (such as ray tracing) for the different frequency bands, and then to provide large datasets of synthetically generated channel parameters (e.g. channel impulse responses) which are needed for physical layer studies and for system simulations in WP3.

Overall, the findings of the studies carried out in WP2-Task2.2 offer valuable insights for enhancing radio resource management (RRM), as well as the physical (PHY) and MAC layers for 6G networks. In RRM, dynamic spectrum allocation and adaptive power control can leverage the measured characteristics of FR3 and sub-THz bands, addressing multipath-dominated environments and ensuring interference mitigation. PHY layer designs can benefit from robust modulation and coding schemes, multipath-aware MIMO configurations, and improved beamforming strategies tailored to industrial and vehicular scenarios. Additionally, synchronization mechanisms should adapt to observed delay spreads for reliable communication. For the MAC layer, environment-specific scheduling, RIS-assisted access mechanisms, and mobility-aware protocols are essential to manage resources efficiently and support high mobility and time-critical applications. These improvements collectively optimize 6G network performance across diverse and complex use cases.

REFERENCES

- [1] W. Fan, H. Sun, Y. Lyu, X. Zhang, J. Borrill, P. Kyosti, B. Derat and F. Zhang, "Challenges and Potential Solutions for 6G Radio Channel Sounding: Industrial Perspectives", submitted to Transactions on Antennas and Propagation
- [2] M. Li, Y. Li, Q. Zeng, K. Olesen, F. Zhang and W. Fan, "Multiple-Frequency-Bands Channel Characterization for In-vehicle Wireless Networks", submitted to Transactions on Antennas and Propagation
- [3] W. Li, X. Hu, J. Gao, L. Zhao, and T. Jiang, "Measurements and analysis of propagation channels in vehicle-to-infrastructure scenarios," IEEE Transactions on Vehicular Technology, vol. 69, no. 4, pp. 3550–3561, 2020
- [4] L. Bai, Z. Huang, Y. Li, and X. Cheng, "A 3d cluster-based channel model for 5g and beyond vehicle-to-vehicle massive mimo channels," IEEE Transactions on Vehicular Technology, vol. 70, no. 9, pp. 8401–8414, 2021
- [5] M. Yang, B. Ai, R. He, Z. Ma, H. Mi, D. Fei, Z. Zhong, Y. Li, and J. Li, "Dynamic v2v channel measurement and modeling at street intersection scenarios," IEEE Transactions on Antennas and Propagation, 2023
- [6] M. Yusuf, E. Tanghe, P. Laly, F. Challita, B. Lannoo, R. Halili, R. Berkvens, M. Weyn, L. Martens, D. P. Gaillot et al., "Experimental study on the impact of antenna characteristics on non-stationary V2I channel parameters in tunnels," IEEE Transactions on Vehicular Technology, vol. 69, no. 11, pp. 12 396–12 407, 2020
- [7] M. G. Doone, S. L. Cotton, D. W. Matolak, C. Oestges, S. F. Heaney, and W. G. Scanlon, "Pedestrian-to-vehicle communications in an urban environment: Channel measurements and modeling," IEEE Transactions on Antennas and Propagation, vol. 67, no. 3, pp. 1790–1803, 2018
- [8] M. Yang, B. Ai, R. He, Z. Ma, Z. Zhong, J. Wang, L. Pei, Y. Li, J. Li, and N. Wang, "Non-stationary vehicular channel characterization in complicated scenarios," IEEE Transactions on Vehicular Technology, vol. 70, no. 9, pp. 8387–8400, 2021
- [9] I. Rashdan, F. de Ponte Muller, W. Wang, M. Schmidhammer, and S. Sand, "Vehicle-to-pedestrian channel characterization: Wideband measurement campaign and first results," in 12th European Conference on Antennas and Propagation (EuCAP 2018). IET, 2018, pp. 1–5
- [10] H. Jiang, B. Xiong, H. Zhang, and E. Basar, "Hybrid far-and near-field modeling for reconfigurable intelligent surface assisted v2v channels: A sub-array partition based approach," IEEE Transactions on Wireless Communications, vol. 22, no. 11, pp. 8290–8303, 2023
- [11] R. Adeogun, G. Berardinelli, P. E. Mogensen, I. Rodriguez, and M. Razzaghpour, "Towards 6g in-x subnetworks with sub-millisecond communication cycles and extreme reliability," IEEE Access, vol. 8, pp. 110 172–110 188, 2020
- [12] M. Bengtson, Y. Lyu, and W. Fan, "Long-range VNA-based channel sounder: Design and measurement validation at mmwave and sub-THz frequency bands," China Communications, vol. 19, no. 11, pp. 47–59, 2022.
- [13] Y. Lyu, P. Kyosti, and W. Fan, "Sub-terahertz channel sounder: Review and future challenges," China Communications, vol. 20, no. 6, pp. 26–48, 2023.
- [14] A-INFO, "Data sheet for biconical antenna sz-2003000/p." 2021, accessed 4 March 2021. [Online]. Available: <https://www.ainfoinc.com/antenna-products/bi-conical-antennas/sz-2003000-p-bi-conical-antenna-2-30-ghz-0db-gain-sma-female>
- [15] Flann, "Data sheet for 22240-20 and 27240." 2022, accessed 4 June 2022. [Online]. Available: <https://flann.com/products/antennas/standard-gain-horns-series-240/>

- [16] Y. Lyu, Z. Yuan, H. Gao, Q. Zhu, X. Zhang and W. Fan, "Measurement-Based Channel Characterization in a Large Hall Scenario at 300 GHz", China Communications, 2023
- [17] Y. Li, F. Zhang, K. Olesen, Z. Ying; G. Pedersen and W. Fan, "An Automated Over-the-Air Radiated Testing Platform for Reconfigurable Intelligent Surface", EuCAP 2024
- [18] Y. Li, F. Zhang, K. Olesen, Z. Ying and W. Fan, "Experimental Over-the-Air Diagnosis of 1-Bit RIS Based on Complex Signal Measurements", IEEE Antennas and Wireless Propagation Letters, 2024.
- [19] Mikko A. Uusitalo et al., "6G vision value use cases and technologies from European 6G Flagship Project Hexa-X", IEEE Access, vol. 9, pp. 160004-160020, 2021.
- [20] [G. Berardinelli et al., "Boosting Short-Range Wireless Communications in Entities: the 6G-SHINE Vision," In Proc. IEEE Future Networks World Forum (FNWF), Baltimore, MD, USA, 2023.
- [21] "IMT Vision-Framework and overall objectives of the future development of IMT for 2020 and beyond", Recommendation ITU 2083.0, 2015.
- [22] [European Vision for the 6G Network Ecosystem, [online] Available: <https://115gppp.eu/european-vision-for-the-6g-network-ecosystem!>
- [23] Anritsu Shockline, [online]: <https://www.anritsu.com/en-us/test-measurement/products/me7868a>
- [24] L. J. Greenstein, D. G. Michelson, and V Erceg, "Moment-method estimation of the Ricean K-factor" IEEE Communications Letters 3.6 (1999): 175-176.
- [25] "5G; Study on channel model for frequencies from 0.5 to 100 GHz," European Telecommunications Standards Institute, Technical Report 38.901, v18.0.0 2024. Available: <https://www.etsi.org/>.
- [26] 3GPP RAN1 contribution R1-2403996, "Discussion on Channel model validation of TR38.901 for 7-24GHz," [Online]: https://www.3gpp.org/ftp/tsg_ran/WG1_RL1/TSGR1_117/Docs
- [27] V. Degli-Esposti, F. Fuschini, E.M. Vitucci, G. Falciasecca, "Measurement and modelling of scattering from buildings". IEEE transactions on antennas and propagation, vol 55, no. 1, 2007, pp.143-153.
- [28] X. Chen, L. Tian, P. Tang, and J. Zhang, "Modelling of human body shadowing based on 28 GHz indoor measurement results," in Proc. IEEE 84th Veh. Technol. Conf. (VTC-Fall), Montreal, QC, Canada, Sep. 2016, pp. 1–5.
- [29] D. Prado-Alvarez, S. Inca, D. Martin-Sacristan, and J. F. Monserrat, "Millimeter-wave human blockage model enhancements for directional antennas and multiple blockers," IEEE Commun. Lett., vol. 25, no. 9, pp. 2776–2780, Sep. 2021.
- [30] S. Collonge, G. Zaharia, and G. Zein, "Influence of the human activity on wide-band characteristics of the 60 GHz indoor radio channel," IEEE Trans. Wireless Commun., vol. 3, no. 6, pp. 2396–2406, Nov. 2004.
- [31] M. Jacob, C. Mbianke, and T. Kürner, "A dynamic 60 GHz radio channel model for system level simulations with MAC protocols for IEEE 802.11ad," in Proc. IEEE Int. Symp. Consumer Electron. (ISCE), Braunschweig, Germany, June 2010, pp. 1–5.
- [32] M. Peter, M. Wisotzki, M. Raceala-Motoc, W. Keusgen, R. Felbecker, M. Jacob, S. Priebe, and T. Kürner, "Analyzing human body shadowing at 60 GHz: Systematic wideband MIMO measurements and modeling approaches," in Proc. Eur. Conf. Antennas Propag. (EuCAP), Prague, Czech Republic, Mar. 2012, pp. 468–472.
- [33] P. Karadimas, B. Allen, and P. Smith, "Human body shadowing characterization for 60-GHz indoor short-range wireless links," IEEE Antennas Wireless Propag. Lett., vol. 12, pp. 1650–1653, Dec. 2013.

- [34] G. R. MacCartney, S. Deng, S. Sun, and T. S. Rappaport, "Millimeter-wave human blockage at 73 GHz with a simple double knife-edge diffraction model and extension for directional antennas," in Proc. IEEE 84th Veh. Technol. Conf. (VTC-Fall), Montreal, QC, Canada, Sep. 2016, pp. 1–6.
- [35] G. R. MacCartney, T. S. Rappaport, and S. Rangan, "Rapid fading due to human blockage in pedestrian crowds at 5G millimeter-wave frequencies," in Proc. IEEE Global Commun. Conf. (GLOBECOM), Singapore, Dec. 2017, pp. 1–7.
- [36] U. T. Virk and K. Haneda, "Modeling human blockage at 5G millimeter-wave frequencies," IEEE Trans. Antennas Propag., vol. 68, no. 3, pp. 2256–2266, Mar. 2020.
- [37] P. Zhang, P. Kyösti, M. Bengtson, V. Hovinen, K. Nevala, J. Kokkonen, A. Pärssinen, "Measurement-Based Characterization of D-Band Human Body Shadowing," 17th European Conference on Antennas and Propagation (EuCAP 2023), March 2023.
- [38] Q. Wu, S. Zhang, B. Zheng, C. You and R. Zhang, "Intelligent reflecting surface-aided wireless communications: A tutorial," IEEE Trans. Commun., vol. 69, no. 5, p. 313–3351, May 2021.
- [39] M. Di Renzo, A. Zappone, M. Debbah, M. S. Alouini, C. Yuen, J. de Rosny, "Smart Radio Environments Empowered by Reconfigurable Intelligent Surfaces: How It Works, State of Research, and The Road Ahead," IEEE Journal on Selected Areas in Communications, vol. 38, no. 11, pp. pp. 2450-2525, Nov. 2020.
- [40] C. Simovski. and S. Tretyakov, An Introduction to Metamaterials and Nanophotonics, Cambridge University Press, 2020.
- [41] M. Merluzzi, A. Clemente, "Anomalous and specular reflections of reconfigurable intelligent surfaces: Configuration strategies and system performance," IEEE Wireless Communications Letters, Vols. vol. 13, no. 10, p. pp. 2707–2711, 2024.
- [42] A. I. Vistnes, "Physics of Oscillations and Waves," Springer Nature, Switzerland, 2016.
- [43] A. Diaz-Rubio, V. S. Asadchy, A. Elsakka, S. A. Tretyakov, "From the generalized reflection law to the realization of perfect anomalous reflectors," Science Advances, vol. 3, no. 8, p. e1602714, 2017.
- [44] S. Kodra, E. M. Vitucci, M. Barbiroli, M. Albani, V. Degli-Esposti, "A Macroscopic Bilateral Modeling Approach for Reflective and Transmissive Metasurfaces," in 18th European Conference on Antennas and Propagation (EuCAP), Glasgow, United Kingdom, 2024.
- [45] V. Degli-Esposti, E. M. Vitucci, M. Di Renzo, S. A. Tretyakov, "Reradiation and Scattering from a Reconfigurable Intelligent Surface: A General Macroscopic Model," IEEE Transactions on Antennas and Propagation, vol. 70, no. 10, pp. pp. 8691-8706, October 2022.
- [46] Ana Diaz-Rubio and S. A. Tretyakov, "Macroscopic Modeling of Anomalous Reflecting Metasurfaces: Angular Response and Far-Field Scattering," IEEE Transactions on Antennas and Propagation, vol. 69, no. 10, pp. pp. 6560-6571, October 2021.
- [47] Y. L. C. de Jong, "Uniform Ray Description of Physical Optics Scattering by Finite Locally Periodic Metasurfaces," IEEE Transactions on Antennas and Propagation, vol. 70, no. 4, pp. pp. 2949-2959, April 2022.
- [48] P.-S. Kildal, "Foundations of Antenna Engineering: A Unified Approach for Line-of-Sight and Multipath," Available at: <https://www.kildal.se/downloads/>, March 2021.
- [49] R. G. Kouyoumjian and P. H. Pathak, "A uniform geometrical theory of diffraction for an edge in a perfectly conducting surface," Proc. IEEE, vol. 62, p. pp. 1448–1461, Nov. 1974.
- [50] E. M. Vitucci, M. Albani, S. Kodra, M. Barbiroli, V. Degli-Esposti, "An Efficient Ray-Based Modeling Approach for Scattering from Reconfigurable Intelligent Surfaces," IEEE Transactions on Antennas and Propagation, vol. vol. 72, no. no. 3, pp. pp. 2673-2685, March 2024.

- [51] L. Felsen and N. Marcuvitz, *Radiation and Scattering of Waves*, IEEE Press Series on Electromagnetic Wave Theory, Wiley, 1994.
- [52] G. L. James, *Geometrical Theory of Diffraction for Electromagnetic Waves*, ser. IEE electromagnetic waves series. P. Peregrinus, 1986.
- [53] G. Deschamps, “Ray techniques in electromagnetics,” *Proc. IEEE*, vol. vol. 60, no. no. 9, p. pp. 1022–1035, 1972.
- [54] R. Luebbers, “Finite conductivity uniform GTD versus knife edge diffraction in prediction of propagation path loss,” *IEEE Transactions on Antennas and Propagation*, vol. vol. 32, no. no. 1, p. pp. 70–76, 1984.
- [55] C. A. Balanis, “*Antenna Theory: Analysis and Design*”, Wiley, New York, 2015.
- [56] W. Fan, I. Carton, J. O. Nielsen, K. Olesen, and G. F. Pedersen, “Measured wideband characteristics of indoor channels at centimetric and millimetric bands”, *EURASIP Journal on Wireless Communications and Networking*, vol. 2016, no. 1, pp. 1–13, 2016.
- [57] ETSI ISG THz Activity Report 2023, available online: <https://www.etsi.org/committee-activity/activity-report-thz>
- [58] 6G-SHINE Deliverable D2.1: “Initial definition of scenarios, use cases and service requirements for in-X subnetworks”, available online: <https://6gshine.eu/wp-content/uploads/2024/11/D2.1-Initial-definition-of-scenarios-use-cases-and-service-requirements-for-in-X-subnetworks.pdf>
- [59] 6G-SHINE Deliverable D.2.2: “Refined definition of scenarios, use cases and service requirements for in- X subnetworks”, available online: <https://6gshine.eu/wp-content/uploads/2024/11/D2.2-Refined-definition-of-scenarios-use-cases-and-service-requirements-for-in-X-subnetworks- v1.0.pdf>
- [60] TIMES Project: <http://www.times6g.eu/>
- [61] TERRAMETA Project: <https://terrameta-project.eu/>
- [62] CENTRIC Project: <https://centric-sns.eu/>
- [63] Tutorial on Reconfigurable Intelligent Surfaces (RIS) — Sionna 0.19.0 documentation. Available online: https://nvlabs.github.io/sionna/examples/Sionna_Ray_Tracing_RIS.html
- [64] U. Demir, C. U. Bas, and S. C. Ergen, “Engine compartment UWB, channel model for intravehicular wireless sensor networks,” *IEEE Transactions on Vehicular Technology*, vol. 63, no. 6, pp. 2497–2505, 2013.